Monthly Notices of the ROYAL ASTRONOMICAL SOCIETY

MNRAS **514,** 3410–3451 (2022) https://doi.org/10.1093/mnras/stac1171
Advance Access publication 2022 April 29

Disc cloaking: Establishing a lower limit to the number density of local compact massive spheroids/bulges and the potential fate of some high-z red nuggets

Dexter S.-H. Hon [1]★ Alister W. Graham,[1]★ Benjamin L. Davis [1,2]★ and Alessandro Marconi[3,4]

[1]*Centre for Astrophysics and Supercomputing, Swinburne University of Technology, Hawthorn, Victoria 3122, Australia*
[2]*Center for Astro, Particle, and Planetary Physics (CAP^3), New York University Abu Dhabi , Abu Dhabi, United Arab Emirates*
[3]*Dipartimento di Fisica e Astronomia, Universitá degli Studi di Firenze, I-50019 Firenze, Italy*
[4]*INAF Osservatorio Astrofisico di Arcetri, I-50125 Firenze, Italy*

Accepted 2022 April 25. Received 2022 April 24; in original form 2021 November 30

ABSTRACT

The near-absence of compact massive quiescent galaxies in the local Universe implies a size evolution since $z \sim 2.5$. It is often theorized that such 'red nuggets' have evolved into today's elliptical (E) galaxies via an E-to-E transformation. We examine an alternative scenario in which a red nugget develops a rotational disc through mergers and accretion, say, at $1 \lesssim z \lesssim 2$, thereby cloaking the nugget as the extant bulge/spheroid component of a larger, now old, galaxy. We have performed detailed, physically motivated, multicomponent decompositions of a volume-limited sample of 103 massive ($M_*/\mathrm{M}_\odot \gtrsim 1 \times 10^{11}$) galaxies within 110 Mpc. Many less massive nearby galaxies are known to be 'fast-rotators' with discs. Among our 28 galaxies with existing elliptical classifications, we found that 18 have large-scale discs, and two have intermediate-scale discs, and are reclassified here as lenticulars (S0) and elliculars (ES). The local spheroid stellar mass function, size–mass diagram and bulge-to-total (B/T) flux ratio are presented. We report lower limits for the volume number density of compact massive spheroids, $n_{\mathrm{c,\,Sph}} \sim (0.17\text{–}1.2) \times 10^{-4}\,\mathrm{Mpc}^{-3}$, based on different definitions of 'red nuggets' in the literature. Similar number densities of local compact massive bulges were reported by de la Rosa et al. using automated two-component decompositions and their existence is now abundantly clear with our multicomponent decompositions. We find disc-cloaking to be a salient alternative for galaxy evolution. In particular, instead of an E-to-E process, disc growth is the dominant evolutionary pathway for at least low-mass ($1 \times 10^{10} < M_*/\mathrm{M}_\odot \lessapprox 4 \times 10^{10}$) red nuggets, while our current lower limits are within an alluring factor of a few of the peak abundance of high-mass red nuggets at $1 \lesssim z \lesssim 2$.

Key words: galaxies: abundances – galaxies: bulges – galaxies: discs – galaxies: elliptical and lenticular, cD – galaxies: evolution – galaxies: structure.

1 INTRODUCTION

Compact ($R_\mathrm{e} \lesssim 2$ kpc) massive ($M_{*,\,\mathrm{gal}} \gtrsim 10^{10}$–$10^{11}\,\mathrm{M}_\odot$), quiescent galaxies (nicknamed 'red nuggets' by Damjanov et al. 2009) are common at high-redshifts (Buitrago et al. 2008; Pérez-González et al. 2008), but relatively rare in the local Universe according to many studies (e.g. Trujillo et al. 2009; Taylor et al. 2010; Saulder, van den Bosch & Mieske 2015). First detected in the local Universe by Zwicky & Kowal (1968) and Zwicky & Zwicky (1971), and later Poggianti et al. (2016), examples include NGC 1271 (Graham, Ciambur & Savorgnan 2016b), NGC 1277 (Trujillo et al. 2014; Graham et al. 2016a), NGC 5252 (Sahu, Graham & Davis 2019), MRK 1216, PGC 032873 (Werner et al. 2018), and others (Damjanov et al. 2013; Savorgnan & Graham 2016b; Tortora et al. 2018). It is frequently speculated that mergers converted the majority of the high-z compact massive galaxies into large (pure) elliptical galaxies by today (e.g. Bezanson et al. 2009; Hopkins et al. 2009; Naab, Johansson & Ostriker 2009; Trujillo, Ferreras & de La Rosa 2011). However, Graham (2013),[1] and later Driver et al. (2013), Dullo & Graham (2013), and Dutton et al. (2013), noted that this may not always be the case and that the spheroidal components of today's disc galaxies (including ES, S0, and S) are also compact and massive.

While 'relic' galaxies, believed to be untouched red nuggets from the local Universe, have been found, they are certainly not common. In addition, relics show complex dynamical structures (Trujillo et al. 2014; Ferré-Mateu et al. 2017) that warrant being treated as more than a single component system. Could the growth of 2D discs, rather than 3D envelopes, be a prelevant mechanism transforming these galaxies? Such a two-phase disc-building scenario, rather than an envelope-building process, was suggested by Graham et al. (2011), and Nelson et al. (2012) subsequently reported on the rapid build up of discs at $z \sim 1$, which could yield S0 galaxies with old stellar populations by today. At stake is the evolutionary pathway for

★ E-mail: dex-hon-sci@outlook.com (DSHH); agraham@astro.swin.edu.au (AWG); ben.davis@nyu.edu (BLD)

[1]First published online in 2011 (https://arxiv.org/abs/1108.0997).

some/many of the Universe's old and massive galaxies, and perhaps also for some of the less massive, high-z 'red nuggets', which we term 'red pebbles', which may now be the bulges of some spiral galaxies.

The distinct size difference between the passive galaxy populations at high and low redshifts sparked deliberations as to the dominant evolution mechanism of massive early-type galaxies (ETGs). While regular size ETG are not rare at low and high-z, one cannot say the same for the compact massive red nuggets. The red nuggets are rather abundant at high redshifts. For instance, Saracco, Longhetti & Gargiulo (2010) reported a comoving number density of compact galaxies at $0.9 < z < 1.92$ of $2.3 \times 10^{-5}\,\mathrm{Mpc}^{-3}$ for $M_*/\mathrm{M}_\odot > 3 \times 10^{10}$. Barro et al. (2013) plotted the evolution of the number density across different redshifts, finding that the number density, n, of red nuggets peaked at a look-back time of 8 Gyr ($z = 1$), with $n_{\mathrm{peak}} \approx 1.5 \times 10^{-4}\,\mathrm{Mpc}^{-3}$. However, regardless of the assorted size and mass criteria used to define red nuggets, it has repeatedly been claimed that these objects are virtually non-existent at $z \sim 0$ (Trujillo et al. 2009; Taylor et al. 2010). The sharp decrease in the compact massive galaxy population indicates a drastic change in galaxy structure over this period of time. However, disagreement among observations (e.g. Trujillo et al. 2007; Valentinuzzi et al. 2010; Poggianti et al. 2013a) led to debates over whether there is indeed a drop in the number of compact massive quiescent systems across time.

The structure of an ETG is often overlooked and oversimplified. Many are misclassified as purely elliptical (E) galaxies while in reality, most ETGs contain a disc (Capaccioli, Held & Nieto 1987; Carter 1987; Nieto et al. 1988; Capaccioli et al. 1990a; D'Onofrio et al. 1995; Graham et al. 1998; Emsellem et al. 2011; Scott et al. 2015); either a large-scale disc making it a lenticular (S0) galaxy, or an intermediate-scale disc making it an ellicular[2] (ES) galaxy (Liller 1966; Savorgnan & Graham 2016b; Graham 2019). Given that different structures, for example, triaxial spheroids or relatively flat discs, form via different physical mechanisms, advances may be made by not simply treating galaxies as if they are single-component systems but rather examining their bulge/disc nature and the role of S0 and ES galaxies in the grand scheme of galaxy evolution.[3]

From a random incomplete sample, Graham, Dullo & Savorgnan (2015) reported a lower limit to the volume number density for local compact massive spheroids in fair agreement with some of the number densities reported for compact massive galaxies at high-z (see also de la Rosa et al. 2016; Costantin et al. 2020). Here, we investigate the issue more thoroughly, using a mass and a volume-limited sample of nearby galaxies combined with a careful, homogeneous, physically motivated[4] multicomponent decomposition of their surface brightness profile. We do this to detect and quantify the primary spheroidal component, a.k.a. bulge.

While we do not advocate any particular origin for the high-z red nuggets, we do note that some bulges may form in other ways. For example, star-forming clumps may form in turbulent discs at high-redshift before migrating inwards to form the bulge (e.g. Bournaud, Elmegreen & Elmegreen 2007; Elmegreen, Bournaud & Elmegreen 2008). This process does not preclude subsequent disc accretion and growth but it does start with a disc rather than the monolithic collapse of a spheroid. In addition, discs (with and without a stabilizing dark matter halo) can experience instabilities leading to bars, which can in turn experience instabilities of their own, leading to the formation of buckled bars often with distinct (peanut shell)-shaped structures known as pseudobulges (e.g. Bardeen 1975; Hohl 1975; Combes & Sanders 1981; Combes et al. 1990). While both low-mass classical bulges and pseudobulges can rotate and have a Sérsic index for their light profile around 1 (Graham 2015), the bar+pseudobulge has a tendency to result in elongated isophotes having a maximum B_6 Fourier harmonic term at around half the length of the bar (Ciambur 2016, and references therein).[5] Classical bulges, bars and pseudobulges, and discs are known to coexist (e.g. Norman, Sellwood & Hasan 1996; Erwin et al. 2003; Athanassoula 2005). In our multicomponent decompositions, we focus on recovering what would be considered the 'classical bulge'. We will present the decompositions of the galaxy light in a forth-coming paper which will compare the sizes and masses obtained from fitting a single Sérsic function, a Sérsic plus an exponential function, and our multicomponent analysis used here to obtain the spheroid size and mass.

In Section 2, we describe the data selection of local galaxies that potentially contain a compact massive spheroid. Section 3 goes through the process of galaxy model fitting and some of the nuances of multicomponent decomposition. In Section 4, the spheroid mass function, the spheroid size–mass relation, and the number density of local compact massive spheroids are presented. A comparison with local spheroid and high-z samples are shown in Section 5. Based on the newly found local spheroids, we discuss the implications for galaxy evolution as a whole in Section 6. We summarize our findings in Section 6.5. Finally, in a set of appendices, we provide an accounting of distance corrections (Appendix A), assumptions governing our adopted mass-to-light colour relations (Appendix B), host galaxy sample (Appendix C), and structural parameters for the local spheroids (Appendix D).

Throughout this paper, we assume the following cosmographic parameters: $H_0 = 68\ \mathrm{km\ s^{-1}\ Mpc^{-1}}$, $\Omega_{\mathrm{m}} = 0.3$, and $\Omega_\Lambda = 0.7$. The absolute magnitude of the sun ($\mathfrak{M}_\odot$) in i −band is set to 4.53 (in AB mag). Unless otherwise stated, all bulge parameters (R_{e}, μ_{e}, and n) correspond to the geometric-mean axis ($R_{\mathrm{eq}} = \sqrt{R_{\mathrm{maj}} R_{\mathrm{min}}}$, aka the equivalent axis) which is equivalent to a circularized form of the isophotes.

2 DATA

In Section 2.1, we explain the parent data selection process. Section 2.2 briefly describe the images sources. Section 2.3 explores the various stellar mass-to-light ratio implemented in this study. Section 2.4 describes our process of finding the appropriate distance for each galaxy. Section 2.5 is a general summary of our volume-limited sample.

2.1 Parent sample

To calculate the number of (compact, massive) spheroids per cubic Mpc, hereafter the number density, as well as study the statistical properties of these local spheroids, a well-defined volume-limited

[2]The concatenated name (elliptical + lenticular) 'ellicular' was introduced for the ES galaxy type in Graham et al. (2017).

[3]Those unfamiliar with the historical discovery of, and continuity between, the different morphological substructures in large, high surface brightness galaxies may like to refer to the galaxy classification grid presented in Graham (2019). It builds upon past works by better recognizing the range of disc sizes in ETGs, which can also contain bars.

[4]Rather than randomly/automatically fitting two or three Sérsic components, we fit physical structures such as bars, *ansae* (e.g. Martinez-Valpuesta, Knapen & Buta 2007), discs, etc., as detected through imaging and kinematic data.

[5]In our decomposition, such pseudobulge structures are effectively folded into the bar component.

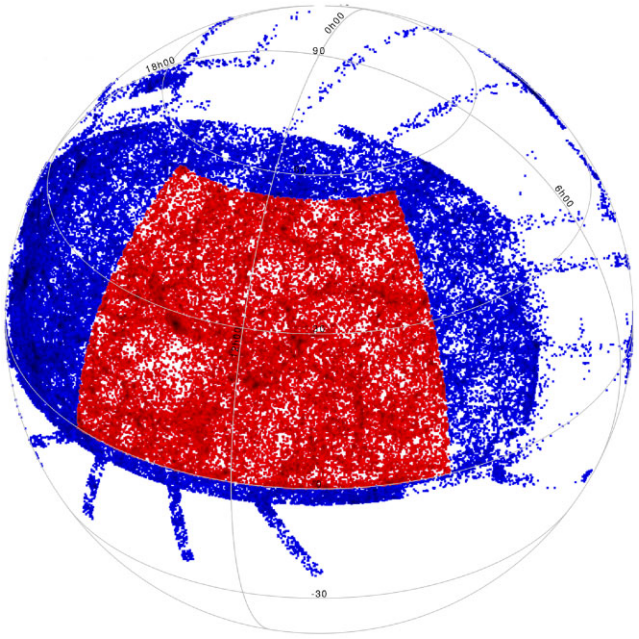

Figure 1. The angular boundaries of the volume-limited sample. The blue points belong to the parent sample from the NASA-Sloan ATLAS catalogue, while the red points are the galaxies satisfying the criteria in equation (1).

sample of galaxies is required. The galaxy images should also be of sufficiently high spatial resolution for us to properly separate the substructures such as discs and bars from the spheroidal components. This limits our sample's maximum co-moving distance to approximately 100 Mpc, because, beyond this point, the multicomponent decomposition becomes challenging with ∼1 arcsec seeing.

We elected to use Sloan Digital Sky Survey (York et al. 2000) photometric data because of its wide sky coverage of ∼14 555 deg^2 (Aihara et al. 2011), and its completeness of galaxies at the bright end ($m_{i'} < 23$ mag) of the galaxy magnitude distribution. Our sample selection is based on the NASA-Sloan ATLAS catalogue,[6] a data set that consists of information from the SDSS DR8 (Aihara et al. 2011), NASA Extragalactic Database (NED; Helou et al. 1991),[7] Six-degree Field Galaxy Redshift Survey (Jones et al. 2004), Two-degree Field Galaxy Redshift Survey (Colless 1999), ZCAT (Huchra et al. 1983), and ALFALFA (Giovanelli et al. 2005). The catalogue provides a list of unique objects as they remove all the redundant data and stars that were previously misclassified as galaxies. It contains 145 155 galaxies within a redshift $z \sim 0.055$.

From the parent sample, we limit the angular boundaries to

$$139^\circ < \text{R.A.} < 214^\circ, \text{ and} \tag{1a}$$

$$0 < \text{Dec} < 55^\circ. \tag{1b}$$

We define these arbitrary boundaries in the attempt to cover the majority of the northern sky in the SDSS field. It contains 55 370 galaxies and captures 8.5 per cent of the sky, or a solid angle of 1.07 sr. Fig. 1 shows the distribution of the angular selection. The area contains notable supergalactic structures such as the Virgo and Coma clusters.

[6]http://www.nsatlas.org/
[7]http://ned.ipac.caltech.edu

2.2 The imaging data

Our imaging data come from SDSS *i*-band images. We decided to use *i*-band photometry for its smaller galactic extinction. The initial flux of the objects was previously measured with a single Sérsic component fit by the SDSS pipeline. The NASA-Sloan ATLAS catalogue provided the flux in the *ugriz* bands in units of *nanomaggies*. The SDSS magnitude of a galaxy in the AB magnitude system (Oke 1974) is:

$$m = [22.5\,\text{mag}] - 2.5\log_{10}(f), \tag{2}$$

where f is the flux of the object in *nanomaggies* and [22.5 mag] is the photometric zero-point magnitude for all bands in the SDSS.

The seeing for each galaxy was estimated by using the Image Reduction and Analysis Facility (`IRAF`; Tody 1986, 1993) function `imexam`. We typically measured 5 or 6 stars randomly distributed in each frame. The `imexam` task was used to fit a Gaussian function to each star. The median value of the full-width at half-maximum (FWHM) was used to represent the seeing of the frame. The measurements are listed in Column 8 of Tables C1–C3.

2.3 Stellar masses

Despite slight differences in definition between studies, compact massive galaxies generally have a stellar-mass larger than $M_*/\text{M}_\odot \sim (1\text{–}7) \times 10^{10}$. We will focus on local host galaxies with a total stellar mass of $M_*/\text{M}_\odot \gtrsim 1 \times 10^{11}$, in order to find compact massive spheroidal components. The determination of the stellar mass depends heavily on different factors, including the initial mass function (IMF); stellar population synthesis (SPS) models; the treatment of dust attenuation; and the fine-tuning of the age, metallicity, and reddening parameters. While it is a common practice to obtain the stellar mass by fitting a stellar model to the spectral energy distribution (SED) of the galaxy light, it is not quite appropriate for our purpose. Having the galaxy SED does not provide us with the mass-to-light ratio (M_*/L) of the spheroid, which would require a structural decomposition in many bands to provide the SED of the spheroid.

While bulge+disc fits in many bands are increasingly produced on scale (e.g. Kennedy et al. 2016), the proximity of our sample, in which bars and rings are resolved, mandates the implementation of multicomponent decompositions. To date, these are performed manually rather than automatically, which allows for greater care and recourse to additional information, such as kinematic maps in the literature. Given time constraints, we elected to focus on the decomposition of *i*-band images (described in detail in Section 3.3). It has also been shown that the *i*-band mass-to-light ratio M_*/L and $(g - i)$ relation has a low scatter intrinsically (Taylor et al. 2011). We use the galaxy colour, rather than the full SED, as a proxy for the spheroid colour when estimating the spheroid M_*/L ratio.

We utilize several mass-to-light versus $(g - i)$–colour relations (MLCRs), $\Upsilon_i(g, i)$, available from the literature and applicable to the *i*-band magnitudes: Zibetti, Charlot & Rix (2009, hereafter Z09); Taylor et al. (2011, hereafter T11); Into & Portinari (2013, hereafter IP13); and Roediger & Courteau (2015, hereafter RC15). All of these works assume an exponentially declining star formation history (SFH $\propto e^{t/\tau}$) in their models. The following equations can be used to calculate the host galaxy total stellar mass, and later the bulge/spheroid stellar mass:

$$\text{Z09}: \log_{10}\Upsilon_i(g, i) = 1.032(g - i) - 0.963 \tag{3a}$$

$$\text{T11}: \log_{10}\Upsilon_i(g, i) = 0.700(g - i) - 0.680 \tag{3b}$$

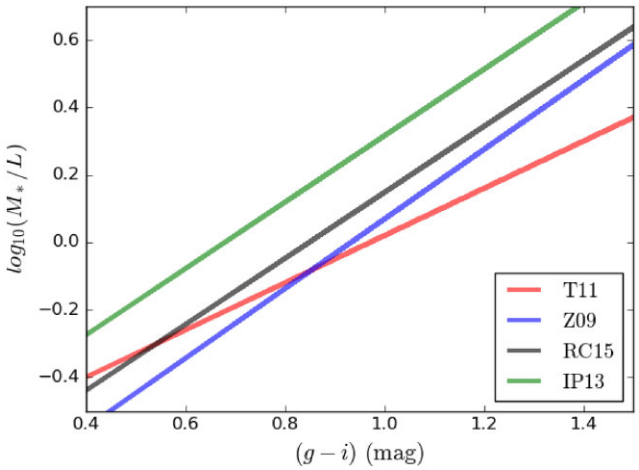

Figure 2. The (M_*/L_i)-to-$(g-i)$ relations. The MLCR equations (3) are shown as red, blue, black, and green lines for T11, Z09, RC15, and IP13, respectively. The massive galaxies ($M_*/\mathrm{M}_\odot > 1 \times 10^{11}$) occupy the colour range $(g-i) \sim 1.20 \pm 0.04$ mag. Within this range, the M_*/L ratio decreases monotonically in the following order: IP13 > RC15 > Z09 > T11.

$$\mathrm{IP13} : \log_{10} \Upsilon_i(g,i) = 0.985(g-i) - 0.669 \quad (3c)$$

$$\mathrm{RC15} : \log_{10} \Upsilon_i(g,i) = 0.979(g-i) - 0.831 \quad (3d)$$

Given the conditions on their respective assumptions, each MLCR self-reported to have the following intrinsic dispersions, Z09: 0.10–0.15 dex, T11: 0.1 dex, IP13: 0.13 dex, and RC15: 0.14 dex.

For our sample, the galaxy $(g-i)$ colours exhibit a familiar bimodal distribution (Tully & Verheijen 1997; Blanton et al. 2003; Kauffmann et al. 2003; Strateva et al. 2003; Baldry et al. 2004; Balogh et al. 2004; Brinchmann et al. 2004). The most massive galaxies occupy the 'red' distribution, centred at $(g-i) \sim 1.2$ mag. We demonstrate the $\log_{10}(M_*/L)$-to-$(g-i)$ relations for the four equations in Fig. 2. Within our sample's colour range ($\sim 1.2 \pm 0.04$ mag), the MLCRs yield decreasing M_*/L ratio in the following order: IP13 > RC15 > Z09 > T11.

Given the goal of this work is comparative in nature, it is important to know the stellar mass relative to the high-z galaxies. While the underlying assumptions in calculating the stellar masses of high-z galaxies have varied from paper to paper, we attempt to make the comparison using the MLCR best matches their assumptions.[8] Throughout this work, we present the result mainly using RC15 stellar mass for the sake of consistency. It represents an intermediate estimation between the lowest (T11) and the highest estimation (IP13[9]). Moreover, RC15 have the same priors as some prominent red nuggets studies (Barro et al. 2013; van der Wel et al. 2014; van Dokkum et al. 2015,, etc.), namely the Chabrier (2003) IMF and the Bruzual & Charlot (2003) SPS. That being said, the effect of using a different M_*/L ratio prescription should be considered thoroughly. Having several stellar mass estimations allow us to examine the potential bias inherent in the choice of stellar mass estimation measurement. We shall explore how the number density of the embedded compact massive spheroids may change for each MLCRs, later in Section 5.4.

[8]The theoretical background for each MLCR is discussed in detail in Appendix B.

[9]Considering there are many S0 and S galaxies in our sample, we apply the disc-model equation from IP13 (see their table 5). Although, the two equations in IP13 (in their tables 3 and 5) for $(g-i)$ colour would return a similar result. We provide several estimates of the stellar mass, with the MLCRs from IP13 yielding the highest masses here. It is noted that this is not an extreme mass estimate, with MLCRs from Bell et al. (2003) and Schombert, McGaugh & Lelli (2019) yielding yet higher masses.

2.4 Distances

We try to account for the peculiar velocity influence on distance measurements. There are several empirical methods to approximate the distance of nearby galaxies: the Tully–Fisher (TF) relation (Tully & Fisher 1977), fundamental plane (Djorgovski & Davis 1987), and velocity field reconstruction (Peebles 1989, 2001; Phelps et al. 2006; Shaya & Tully 2013). To construct our volume-limited sample, the procedure involved several steps.

(i) Redshifts. We commenced this project by first calculating the distances using the corrected redshift (ZDIST) available in the NASA-Sloan ATLAS catalogue. The redshift values are based on the Mark III Catalogue of Galaxy Peculiar Velocities (Willick et al. 1997, hereafter W1997), obtained using the TF or D_n–σ relation. This catalogue provides a Malmquist bias-corrected distance based on the velocity field provided by the IRAS 1.2 Jy redshift survey (Fisher et al. 1995) density field. The initial distances and stellar mass estimation are shown in the upper panel of Fig. 3 as grey crosses.

(ii) A broad mass–distance sample selection boundary. We select our initial galaxy sample for further examination using the broad mass–distance selection criteria (blue line) in the upper left-hand corner of Fig. 3, satisfying the arbitrary condition

$$\log_{10}(M_*/\mathrm{M}_\odot) > 10 + (0.014 \times \mathrm{Dist.}), \quad (4)$$

and Dist. < 115 Mpc. This is intended to produce a manageable sample size of galaxies for us to further check if redshift-independent distances are available on NED. There are 708 data points (green crosses) remaining after imposing the mass–distance sample selection boundaries.

(iii) Updated redshift-independent distances. Each of these green points was checked in NED to see if there were redshift-independent measurements. We primarily focused on obtaining distances related to stellar phenomena, such as surface brightness fluctuation (SBF), Cepheids, Supernovae Ia (SNIa), the tip of the red giant branch (TRGB), etc. When such measurements were not available for a galaxy, we resorted to using the velocity correction from NED, based on the linear infall velocity model in Mould et al. (2000, hereafter M2000). This model corrects for the influence imposed by major gravitational bodies, namely the Virgo Cluster, the Great Attractor, and the Shapley supercluster.

The revised distances are shown as the coloured dots and purple crosses (labelled 'New Distance', see Column (4) in Tables C1–C3) in the lower panel of Fig. 3.[10] One can see changes from the upper panel. For example, one can see how the Virgo Cluster at ~17 Mpc materializes from the data, and quite a number of galaxies escape the blue-line selection boundary. One can similarly expect that some galaxies initially outside of the blue-line selection boundary (and ignored by us) would be shifted inside. We mitigated against this by limiting the final selection to galaxies in three regions, which

[10]Note that, because we rely on redshift independent distances measured using stellar information, our distance is luminosity distance. Although, in this redshift range ($0 < z < 0.025$), luminosity distance and comoving distance are similar.

contained the galaxies previously outside these bins based on the older distances. Within the broad mass–distance selection boundary sample of 708 galaxies, we defined three volumes, aka bins, to acquire both a manageable[11] and useful number of galaxies.

$$\text{Bin 1}: M_*/\mathrm{M}_\odot(\mathrm{IP13}) \gtrsim 5.0 \times 10^{11}, \quad 75\,\mathrm{Mpc} < \mathrm{Dist.} < 110\,\mathrm{Mpc} \tag{5a}$$

$$\text{Bin 2}: M_*/\mathrm{M}_\odot(\mathrm{IP13}) \gtrsim 2.0 \times 10^{11}, \quad 45\,\mathrm{Mpc} < \mathrm{Dist.} < 75\,\mathrm{Mpc} \tag{5b}$$

$$\text{Bin 3}: M_*/\mathrm{M}_\odot(\mathrm{IP13}) \gtrsim 1.0 \times 10^{11}, \quad \mathrm{Dist.} < 45\,\mathrm{Mpc}. \tag{5c}$$

We chose these arbitrary bins to include the massive galaxies that potentially host a massive bulge ($M_*/\mathrm{M}_\odot > 10^{10}$). The data points of each bin are highlighted in different colours in the lower panel of Fig. 3.

(iv) Further refinements. In this step, we further checked the appropriate distance of each galaxy in the three bins. In addition to the redshift-independent measurements, as well as the W1997 and M2000 velocities, we collected another independent set of distances using the newly available *Cosmicflow-3* distance calculators (Kourkchi et al. 2020). The *Cosmicflow* project uses a collection of diverse distance measurements (Tully et al. 2008, 2013) to derive the velocity and density field fluctuations in the local Universe. Their two online calculators provide a distinct approach for galaxies with Dist. < 38 Mpc and distances greater than this and up to 200 Mpc. In the former case, the velocity field is based on the non-linear numerical action orbit reconstruction in Shaya et al. (2017) and the velocity model of Tully et al. (2014). For the latter case, the distance is inferred from the 3D linear velocity field model in Graziani et al. (2019), with an emphasis on mitigating inherent biases such as Malmquist bias and the lognormal distribution of peculiar velocities. The main advantage of *Cosmicflow* is the large library (17 647 individual galaxies) of distances from which the velocity field is constructed.

Armed with 3 to 4 distinct distance estimations for each galaxy in our set of three bins, we found that no matter which distance is chosen, all of our sample lies within the three bins selection volume (within 110 Mpc). The sample provides a good representation of galaxies within these boundaries.

The distance we used for the calculation is chosen on a case-by-case basis. The z-independent distance is prioritized if they are available. We have 20 and 1 z-independent distances in Bin 3 and Bin 1, respectively. Unless the measurement has a significant error or disagrees significantly with the other measurements, z-independent distance is used (in total 18). When z-independent distances are not available, we resort to using the *Cosmicflow-3* distances (in total 81). There are a few of *Cosmicflow-3* distances that fall within the 'triple-value' region, as the Virgo Cluster bends the distance–velocity relation into a cubic function and returns three distinct distance solutions. In such cases (in total, only four galaxies), we choose the W1997 distances instead.

The final distance we used in the calculation is shown in Column (2) in Tables D1–D3, and the details of specific cases are discussed in the Appendix A. After eliminating all the false samples (stars or galaxies with obviously wrong velocities), this leaves us with 115 galaxies spread over three bins.

[11]By the term 'manageable', we are referring to the workload required to perform careful multicomponent decomposition.

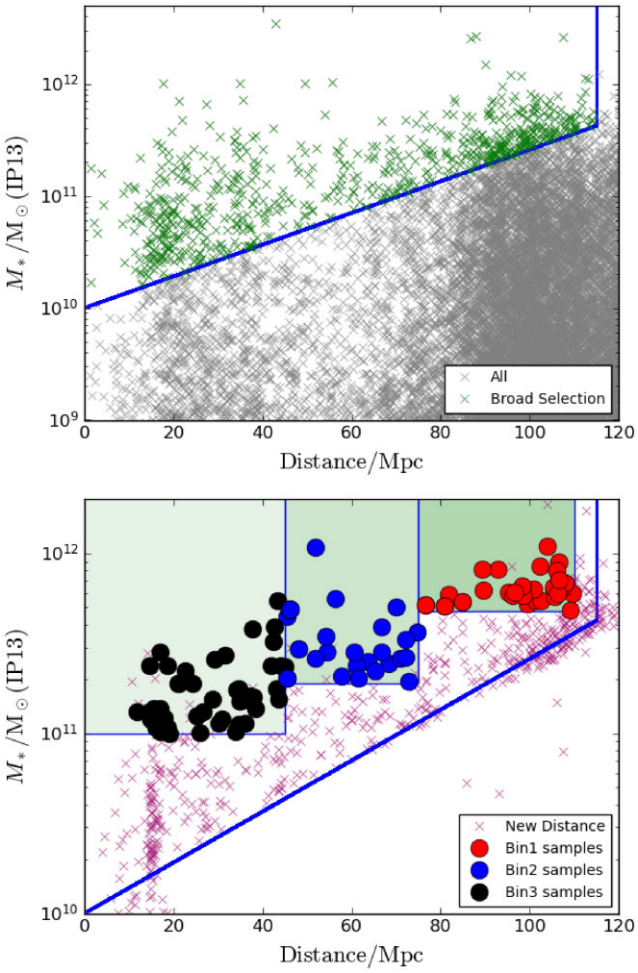

Figure 3. The data selection for potential host galaxies containing compact massive spheroids. Top: The grey crosses (×) are the galaxies satisfying the angular sample selection boundaries in equation (1). The green crosses (×) are the galaxies that satisfy equation (4). All distances are from W1997. Bottom: Bins 1, 2, and 3 are shaded in green for the right, middle, and left boxes, respectively. All distances have been updated (see Appendix A). The red, blue, and black points correspond to the samples listed in Tables C1–C3, respectively. The violet crosses (×) either do not satisfy the equation (5) conditions or do not consistently reside in the same bin if alternative distance estimates are adopted (see Fig. A1). After careful examination, we excluded the false sample that are stars or galaxies with wrong velocities. The crosses not overlapping with the points in the lower panels are rejected from the analysis.

2.5 Volume-limited galaxy sample

We defined the bins in a manner that would produce a manageable sample size for careful multicomponent decomposition work. The volume of each bin and the total survey volume are shown in Table 1. It is labour intensive to create a detailed decomposition. As we will discuss in Section 3.3, the process involves manual attention and cross-referencing evidences from the literature. While it would be best to conduct large-scale studies on all the local massive host galaxies, the current limitation in automatic decomposition programs prevent us from doing so. We mitigate the challenge by limiting a local volume with respect to the relevant mass range.

Table 1. The volume of each bin.

	Distance (Mpc)	Volume (Mpc^3)
Bin 1	75 – 110	3.25×10^5
Bin 2	45 – 75	1.18×10^5
Bin 3	0 – 45	3.26×10^4
Total	0 – 110	4.76×10^5

Table 2. The lower mass limit of each bin using different MLCRs.

	T11 ($M_*/M_\odot$)	Z09 ($M_*/M_\odot$)	RC15 ($M_*/M_\odot$)	IP13 ($M_*/M_\odot$)
Bin 1	1.8×10^{11}	2.9×10^{11}	3.4×10^{11}	5.0×10^{11}
Bin 2	7.2×10^{10}	1.1×10^{11}	1.3×10^{11}	2.0×10^{11}
Bin 3	3.0×10^{10}	5.7×10^{10}	6.7×10^{10}	1.0×10^{11}

In the parent sample selection (equation 5), we have proceeded by intentionally using the highest mass estimations, which come from IP13, in order not to miss potential host galaxies of compact massive spheroids. This ensures the inclusion of even the least likely (the least massive) candidates within our stellar mass selection criteria. For easy comparison across different MLCRs, we present a table of conversion, the lower mass limit for each bin across the four MLCRs in Table 2. As one applied another MLCRs instead of IP13, the galaxies stellar mass within the three bins decreased by roughly a fixed amount ($\delta M_*/M_\odot$).[12] The lower mass limits for other MLCRs are obtained by reducing the IP13 lower mass limits by $\delta M_*/M_\odot$. Ultimately, the choice of MLCR would not affect the analysis. As we move forward to discuss in RC15 stellar mass terms, the lower mass boundaries of the host galaxies are now $3.4 \times 10^{11}\,M_\odot$, $1.3 \times 10^{11}\,M_\odot$, and $6.7 \times 10^{10}\,M_\odot$ for Bin 1, 2, and 3, respectively.

Given each bin's differences in the lower galaxy mass that was included, throughout this paper, the result of each bin is presented separately. Tables C1–C3 show the galaxies' basic information from the three bins.

3 METHODOLOGY

This section showcase our data processing methods, including the reduction process (Section 3.1), modelling of the galaxy image (Section 3.2), and the multicomponent decompositions (Section 3.3). Based on the result of the decomposition, we explore several important aspect about the embedded spheroids such as: the spheroid colour (Section 3.5), mass (Section 3.6), and size (Section 3.7). Additionally, we reclassify the morphology for each galaxy based on our multicomponent decompositions (Section 3.4).

3.1 Data reduction

We obtained cutout images of the galaxies from the SDSS DR12 Science Archive Server (SAS).[13] Each frame spans 2048 pixels × 1489 pixels (819.″2 × 595.″6). The flux originates from multiple sources, including the Poissonian background noise plus the signal coming from foreground stars and our target galaxy. Naturally, the distribution of the pixel intensity values in frames with a sufficient field-of-view to capture the sky background will be a combination of a symmetrical Poissonian bell curve (random noise) centred on a low photon count, plus pixels with target-galaxy light stretching to brighter intensities. We define our sky value as the median of the Poissonian distribution and subsequently subtract it from the frame (Almoznino, Loinger & Brosch 1993; Davis, Graham & Cameron 2019; Sahu et al. 2019).

The use of wide-frame cutouts resolves the reported SDSS sky subtraction problem in the SDSS DR8 (Blanton et al. 2005; West 2005; Bernardi et al. 2007; Lauer et al. 2007; Hyde & Bernardi 2009; West et al. 2010; Blanton et al. 2011). The SDSS standard photometric pipeline (Lupton et al. 2001) estimates the background from a 100 arcsec × 100 arcsec frame and subtracts it from the image. In the case of large extended local galaxies, such an approach will result in oversubtraction because the frame is not wide enough to reach beyond the galaxy. Since our frame is significantly bigger than the target galaxy, the sky subtraction issue is under control.

After the sky subtraction, the images proceed to a masking procedure. It is important to mask out the excess light from foreground stars and nearby galaxies because they can prevent the fitting algorithm (Section 3.2) from creating an accurate model for the target galaxy. We divided the masking process into two stages.

(i) First, we exclude the majority of the bright sources using the `SExtractor` (Bertin & Arnouts 1996) automatic process. The program identified the contamination by threshold sigma detection. While it is good at tracking isolated sources, `SExtractor` is not as effective in deblending overlapping objects, in particular, foreground stars in front of a galaxy along the line of sight. We handle this issue through the second stage: manual masking.

(ii) Additional foreground objects are identified by human eyes and concealed using the polygon tool from `DS9` (Joye & Mandel 2003). We masked the bright sources, as well as the dust lanes that influence the stellar light.

We construct the mask using the `IRAF` function `mskregion`. Combining both the automatic and manual masking, all the irrelevant objects are effectively removed from the frame.

3.2 Isophotal fitting

The galaxy images are modelled with the isophotal fitting program `ISOFIT` (Ciambur 2015). The method was first described by Carter (1978, 1987) and implemented by Jedrzejewski (1987). It has since been a staple technique in modelling early-type galaxies, most notably through the `IRAF` package `ellipse`. The algorithm fits a series of nested isophotes centred around the peak brightness region. It performs a least-square fit on each isophote with intensity, $I(\theta)$, expressed by the Fourier series:

$$I(\theta) = \langle I_{ell} \rangle + \sum_n [A_n \sin(n\theta) + B_n \cos(n\theta)], \quad (6)$$

where $\langle I_{ell} \rangle$ is the average intensity, A_n and B_n are the harmonic coefficients of nth order, and θ is the azimuthal angle. `ISOFIT` made two significant changes to the Jedrzejewski (1987) algorithm. It replaces the azimuthal angle (θ) with the eccentric anomaly (ψ), with the following relation:

$$\psi = -\arctan\left(\frac{\tan\theta}{1-\epsilon}\right), \quad (7)$$

[12] While $\delta M_*/M_\odot$ is different for each galaxy, the deviation is insignificant. The deviation between the maximum and minimum $\delta M_*/M_\odot$ is equal to 0.087 dex for Bin 1, 0.01 dex for Bin 2, and 0.002 dex for Bin 3.

[13] https://dr12.sdss.org/bulkFields, https://dr12.sdss.org/sas/dr12/boss/photoObj/frames/301/

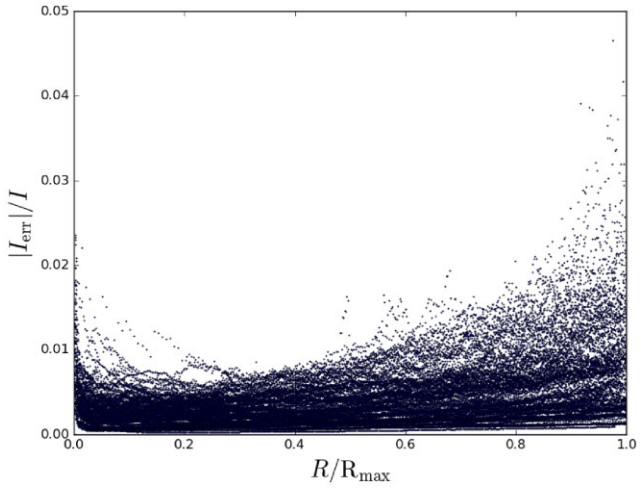

Figure 4. (Model error)-to-intensity ratio along the normalized radius of 103 galaxies. The ($|I_{\rm err}/I|$) ratio is defined by $I_{\rm err} = \sigma/\sqrt{N}$, where σ is the standard deviation and N is the number of pixels comprising the isophotal ring at a given radius. The normalized radius ($R/R_{\rm max}$) is defined by the maximum radius $R_{\rm max}$ to which we modelled each galaxy. We display the average ratio with black points.

where ϵ is the varying ellipticity $\epsilon \equiv 1 - (b/a)$ of each nested isophote, and a and b are the lengths of the semimajor and semiminor axes, respectively.

The incorporation of the ellipticity information in the eccentric anomaly gives us a better description of the shape of each isophote, in particular those that have high ϵ. It substantially improves the modelling of edge-on disc galaxies and those with elongated bars. Given the dramatic improvement, `ISOFIT` additionally allows more higher harmonic coefficients, with amplitudes A_n and B_n typically asymptoting to zero by $n \lesssim 12$. The high-order Fourier coefficients capture the radial perturbations of each isophote. Each integer n represents a specific type of deformation from a perfect ellipse. For example, A_4 and B_4 describe the amplitude of a four-cornered deformation of an ellipse, in turn showing the 'boxyness' and 'discyness' of the isophote. As illustrated in Ciambur (2015, fig. 4), the high-order ($n \geq 6$) coefficient reveals additional information about a galaxy that is rarely studied, i.e. the B_6 profile captures (peanut shell)-shaped structures nestled around bars (Ciambur & Graham 2016; Ciambur, Graham & Bland-Hawthorn 2017; Saha, Graham & Rodríguez-Herranz 2018).

The 2D intensity map described by the `ISOFIT` task is comprised of a series of 1D radial distributions, capturing the surface brightness, ellipticity, position angle, and Fourier harmonic terms. The ratio of the model error $I_{\rm err} = \sigma/\sqrt{N}$ to intensity (I) at each isophote is shown in Fig. 4, where σ is the standard deviation of the pixel values (data) about the 2D reconstruction of the image created with the IRAF task `Cmodel` (Ciambur 2015) and N is the number of pixels in each isophote. $R_{\rm max}$ is the cutoff radius to which we modelled each galaxy.[14] While the model error-to-intensity ratio increases with radius, they do not deviate much from $I_{\rm err}/I = 0$, with most points having $|I_{\rm err}|/I < 0.02$. The error from the isophotal fitting is small and the surface brightness information is well captured by the fitting process.

It is common in the community to use 2D fitting algorithms such as `GIM2D` (Simard 1998), `GALFIT` (Peng et al. 2002, 2010), `BUDDA` (de Souza, Gadotti & dos Anjos 2004) and `IMFIT` (Erwin 2015), to fit 2D analytic functions directly on to the image. While there are pros and cons concerning whether 1D profile or 2D image analysis is more adequate (e.g. Ciambur 2016), we favour the use of the above-mentioned 1D radial brightness profiles. As shown in van der Marel, Binney & Davies (1990) and Läsker, Ferrarese & van de Ven (2014), some triaxial spheroids exhibit twisting in their position angle (PA) and ellipticity ϵ profile. The aforementioned 2D codes cannot account for the shape changes because they assume a fixed PA and ϵ for each galaxy component. Furthermore, Savorgnan & Graham (2016a) conducted an empirical comparison between 1D and 2D methods on the same galaxies and remarked on some key advantages of the 1D approach. With the 1D radial profiles, weak features such as embedded discs and small bars were more visible. The changes in the PA, ϵ, and harmonic coefficient profiles can signify the presence of these components. They also found that the 2D routine has a substantially harder time converging to a meaningful solution. We, therefore, adopted the more manually intensive, but also more reliable, 1D approach over the automated 2D approach.

A few of the galaxies from our three bins had to be excluded from the analysis due to various reasons:

(i) edge-on galaxies with substantial dust covering the centre of the galaxy (see Section 3.2);
(ii) galaxy pairs where the gravitational interaction significantly distorts the structure of both galaxies; or
(iii) unique cases for which the fitting program failed to produce a convincing 2D model.

Ultimately, we have reliable data for 27, 24, and 52 galaxies in Bins 1, 2, and 3, highlighted as red, blue, and black in Fig. 3, respectively. 12 galaxies are rejected in our analysis.

We have listed the perceived Hubble types by their (de Vaucouleurs et al. 1991, hereafter RC3) classifications in Column (8) of Tables C1–C3. For each bin, they are Bin 1 (E: 13, S0: 6, and S: 8), Bin 2 (E: 9, S0: 7, and S: 8), and Bin 3 (E: 6, S0: 18, and S: 28).

3.3 Multicomponent decompositions

In this section, we present the justification and describe the decomposition process. The projected radial intensity profile $I(R)$ of a spheroid or bulge can be described by the Sérsic (1968) function, expressed in Graham & Driver (2005) as:

$$I(R) = I_{\rm e} \exp\left\{-b_n\left[\left(\frac{R}{R_{\rm e}}\right)^{\frac{1}{n}} - 1\right]\right\}, \tag{8}$$

where $R_{\rm e}$ is the effective 'half-light' radius, n is the Sérsic index, $I_{\rm e}$ is the surface brightness at $R_{\rm e}$, and b_n can be obtained by solving $\Gamma(2n) = 2\gamma(2n, b_n)$, involving the complete and incomplete Gamma functions. The surface brightness profile is calculated by substituting $I(R)$ into the following equation:

$$\mu(R) = zp - 2.5\log_{10}\left[\frac{I(R)}{ps^2}\right], \tag{9}$$

where zp is the zero-point magnitude and ps is the pixel angular size.

Many conventional studies perform Bulge+Disc decompositions involving a Sérsic $R^{(1/n)}$-bulge plus an exponential-disc (e.g. Andredakis, Peletier & Balcells 1995; Seigar & James 1998; Iodice, D'Onofrio & Capaccioli 1999; Khosroshahi, Wadadekar & Kembhavi 2000; D'Onofrio 2001; Graham 2001; Möllenhoff & Heidt 2001; Simard et al. 2002; Allen et al. 2006; Simard et al. 2011, etc.). While a gravitationally bound system can be broken into rotational (disc) and triaxial, pressure-supported components (bulge), in the case of a galaxy, there is an extra layer of complication.

[14]For further information on the galaxy size, see Appendix C.

Table 3. `Profiler` functions and their corresponding galactic structures.

Analytic functions	Galactic structures
Sérsic[a]	Spheroid/Bulge or Lens
Core-Sérsic[b]	Core-depleted spheroid
Exponential[c]	Type I Disc
Broken exponential[d]	Type II/III disc
Edge-on disc model[e]	Inclined disc
Ferrers[f]	Bars
Gaussian	Excess light, spiral arms, rings, and *ansae*

Note. [a] Sérsic (1968); [b] Graham et al. (2003a); [c] Patterson (1940), de Vaucouleurs (1959); [d] de Grijs, Kregel & Wesson (2001), Pohlen et al. (2002); [e] van der Kruit & Searle (1981); [f] Ferrers (1877), Sellwood & Wilkinson (1993).

Additional substructures, such as *ansae* and rings, are common. They have distinct features and stellar orbits from a bulge or a disc. Furthermore, spheroids and discs can have a more complex structure than the Sérsic and exponential function permit. For instance, massive galaxies often have a depleted core (King 1978; Trujillo et al. 2004), where the light in the centre is fainter than what a Sérsic function predicts.

Bulges/spheroids are also known to rotate. Some rotate along their short axes (Binney 1978; Miller 1978). There are evidences where spheroid rotate around both major (Davies & Birkinshaw 1986, 1988; Franx, Illingworth & Heckman 1989b; Jedrzejewski & Schechter 1989) and minor (Schechter & Gunn 1979; Efstathiou, Ellis & Carter 1980; Davies et al. 1983; Bender 1988b, 1990; Bender, Saglia & Gerhard 1994) axes.

Discs also often exhibit bending in their outer region (van der Kruit 1987; Pohlen et al. 2004; Erwin, Beckman & Pohlen 2005), classified by the different behaviour as either Type I (no bend), II (a downward-bend), and III (a temporary upward-bend). Moreover, substructures such as nuclear discs, intermediate-scale discs, and nuclear stellar clusters also exist. They can contribute an indelible amount of stellar light to the galaxy.

For years, these extra features have motivated the use of multicomponent decompositions for well-resolved galaxies (e.g. Martin 1995; Prieto et al. 1997; Aguerri, Beckman & Prieto 1998; Graham, Jerjen & Guzmán 2003b; Laurikainen, Salo & Buta 2005; Laurikainen et al. 2010; Vika et al. 2012; Läsker et al. 2014; Savorgnan & Graham 2016a; Davis et al. 2019; Sahu et al. 2019). Indeed, Stone et al. (2021) concluded 'that two-component fits (e.g. Sérsic plus exponential) are insufficient to describe late-type galaxies with high fidelity'.

In addition, one need to be cautious while modelling with Sérsic function. A part of its usefulness comes from the function's flexibility. It is able to fit a range of light profile shapes. The flexible nature, however, also presents a problem. If one ignores a prominent substructure, such as a bar or an outer ring, the fitting code will attempt to compensate by bending the Sérsic function, intended to describe the bulge, upward at the tail end, leading to a higher Sérsic index n and radius R_e than is correct for the bulge. Therefore, in a counterintuitive sense, the most accurate way to model a spheroid is to not solely focus on the Sérsic component but also account for potentially biasing substructures. With that in mind, we proceed to model galaxies' structures.

We use the program `Profiler` (Ciambur 2016) to perform the decomposition. The analytic functions in `Profiler` that were used to depict the different galactic structures are listed in Table 3. We start our fitting using `ISOFIT`'s major axis surface brightness profile, where the galaxy components often appear more prominent than in comparison with the geometric-mean axis.[15] The key to the decomposition is to identify deviations in the various 1D profiles for each galaxy, such as their surface brightness, position angle, and ellipticity profiles. Each component that we include in the fitting process has a corresponding physical substructure that is visible and identified in either the 2D image or (more readily) the 1D profiles. We additionally spent some time scouring the literature for additional evidence to justify the inclusion of components. This typically included confirmation of bars already detected by others or rotating discs seen in kinematic data.

To illustrate the process, here we present a case study using the late-type galaxy NGC 4045. In Fig. 5, we present the `ISOFIT` modelling result. In the bottom row, from left to right, they are the image of NGC 4045, the model produced by the `ISOFIT` model, and the residual by subtracting the image by the model. The top row illustrates a 1D representation of the image, model and residual, by averaging the pixel value along the vertical direction. One can see the `ISOFIT` model has done a marvellous job capturing the surface brightness profile of the galaxy.

Fig. 6 shows the decomposition for NGC 4045 along its geometric-mean axis, a.k.a. equivalent axis, R_{eq}. The galaxy has a small bulge (dashed-dotted red curve), a large extended broken disc (blue curve), and a bar (orange curve; see Erwin 2005; Erwin & Debattista 2013; Díaz-García et al. 2016; Font et al. 2017, 2019). Along the ϵ and PA profiles, there are two 'bumps' at $R_{eq} \sim 3$ arcsec and 7 arcsec, corresponding to the inner spiral arm-like structures. Comerón et al. (2014) classified NGC 4045 as a $(R'_1L)SAB(rs, nl)ab$ galaxy containing two outer rings and a 'nuclear lens'.[16] Upon closer inspection (see Fig. 7), there are two dust lanes obscuring the light at ∼7–8 arcsec (see also Erwin & Sparke 2002), resulting in a dip in ϵ, making the isophote appear more circular. We modelled the nuclear lens with a Sérsic function (dashed red line) with a very low Sérsic index ($n \sim 0.01$). The strong position angle (PA) twist at $R_{eq} \sim 27$ arcsec coincides with the small bump in ϵ. This feature associated with the bar and elevation in μ is an '*ansae*', where the bar transitions into the disc rotation. Finally, the outermost plateau of $\epsilon \sim 0.4$ beyond $R_{eq} \sim 40$ arcsec is the projection of the inclined, rotationally supported disc (see Erwin et al. 2005; Erwin, Pohlen & Beckman 2008). We use an broken exponential model for this disc, plus a Gaussian function to account for the brightening in μ at $R_{eq} \sim 43$ arcsec, which thereby captures the weak spiral arm within this disc. Failing to account for the elongated bar structure in NGC 4045 would result in the fitted Sérsic function substantially overestimating the mass and size of the spheroidal component of this galaxy. As shown in Column (9) of Table C1, our sample has a range of morphologies.

Our decomposition experience also reveals that the outer components can significantly affect the estimation of a bulge. That is, if a prominent structure in the outer region of a galaxy, such as a strong spiral arm or disc truncation, is not considered, then the parameters of the disc will be distorted. Like a domino effect, an incorrect disc model impacts upon the Sérsic model at the centre, changing its parameters to compensate for the ill-modelled disc.

We analysed 103 galaxies with the same individual level of attention to detail, following that done by Davis et al. (2019) and Sahu

[15]The geometric mean of each isophotes' major- and minor-axis, equivalent to a circularized version of the galaxy.

[16]The 'nuclear lens' appears to be the head of the spiral arms that run perpendicular to the so-called 'bar' in this galaxy.

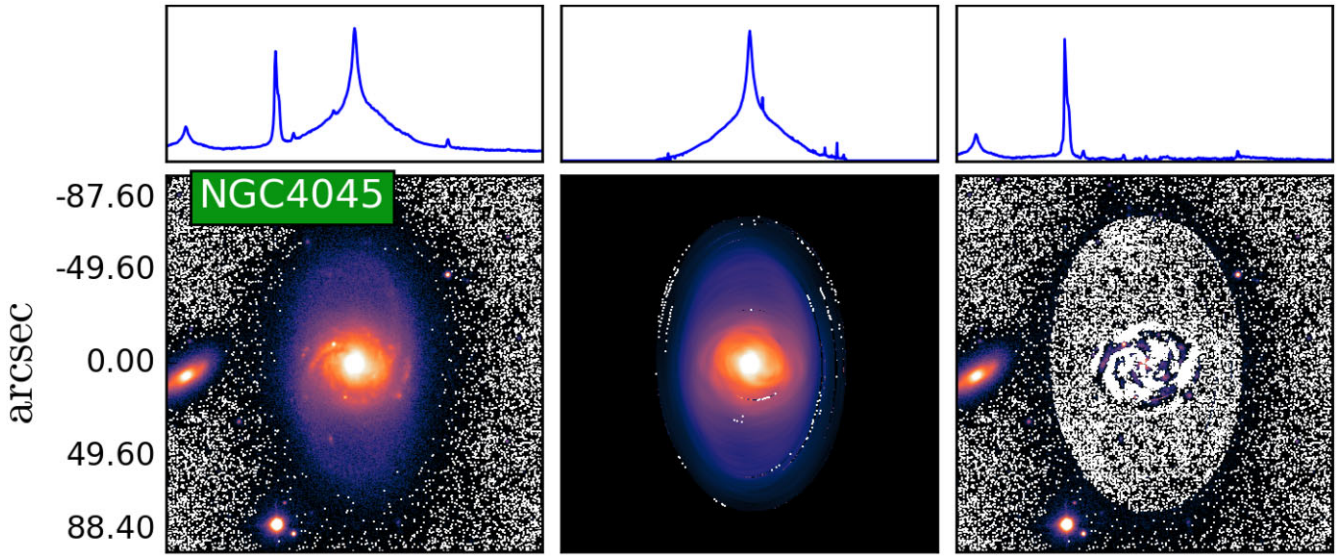

Figure 5. NGC 4045, an example of an early-type spiral galaxy. Bottom row: The galaxy images, the pixel value are shown in the same contrast setting across the three panels. Upper row: The average pixel value along the y-axis of the image. Left-hand column: The original image. Middle column: The 2D isophote model created by CMODEL. Right-hand column: the residual image. The images are orientated with their right-hand side pointing north and up side pointing east.

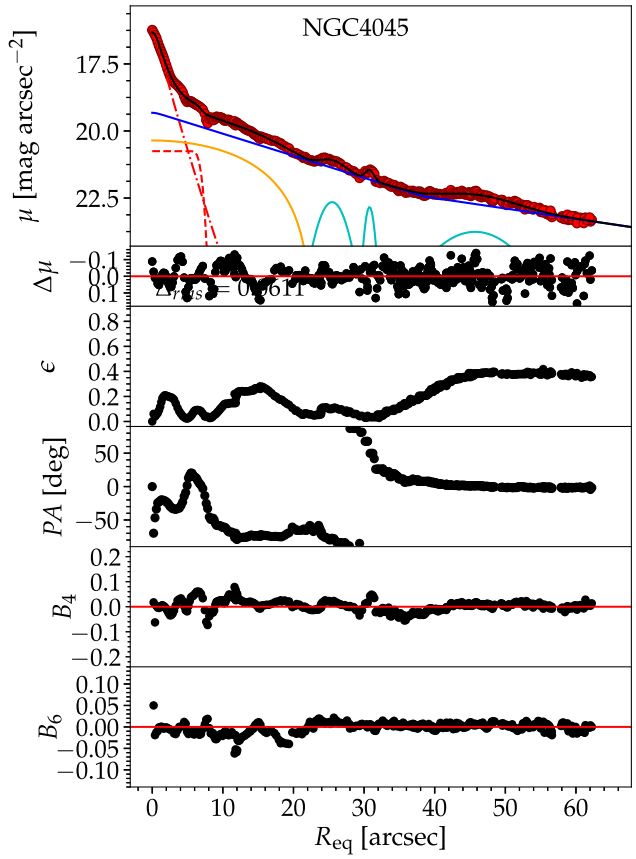

Figure 6. NGC 4045 'equivalent axis' surface brightness profile, with $R_{\rm eq}$ equivalent to the geometric mean of the major (a) and minor (b) axis: $R_{\rm eq} = \sqrt{ab}$. From top to bottom panel: i-band surface brightness (μ); (model − data) residual ($\Delta\mu$); ellipticity (ϵ); Position Angle (PA); and 4th-order Fourier harmonic coefficient (B_4). The galaxy components are the Bulge (dashed-dotted red line), nuclear lens (dashed red line), Bar (orange), Disc (blue), plus a broad ansae and a faint outer spiral arm (cyan).

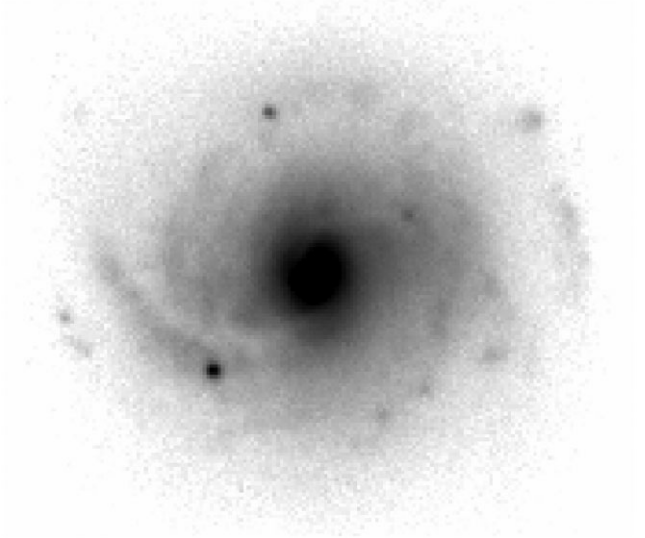

Figure 7. A zoomed-in image for the inner part (∼20 arcsec) of NGC 4045 with the same orientation as Fig. 5. One can see a four armed 'pinwheel' shaped pattern. The two bright fringes of dust lanes spiraling towards the centre obscure some of the light and decreases the ellipticity at ∼7 arcsec, making the isophote appears more circular than it should be.

et al. (2019) in their decomposition of late- and early-type galaxies with directly measured supermassive black hole masses. Tables D1–D3 provide the best-fitting, equivalent-axis, Sérsic parameters for the 103 spheroids. This axis provides circularized component sizes which enable `Profiler` to integrate each component's model surface brightness profile to obtain the associated luminosity. The resulting spheroid apparent magnitudes are given in Column (7) of the tables. From there, we calculated the stellar mass based on the four MLCRs from equation array 3. These are listed in Columns (9)–(12).

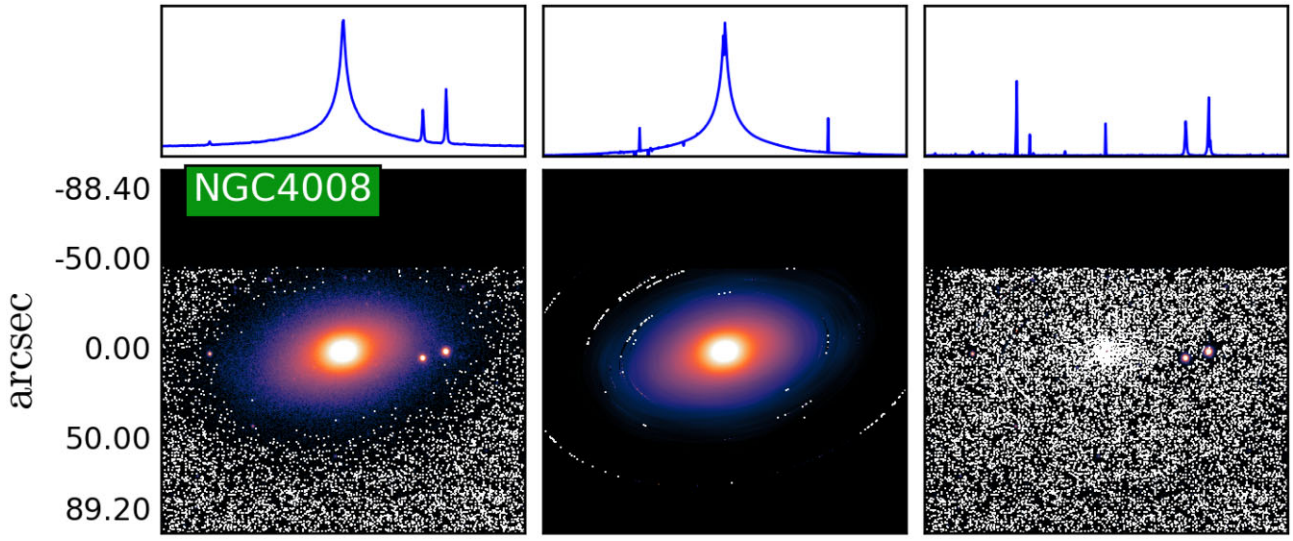

Figure 8. NGC 4008, an example of an elliptical (E5) galaxy according to RC3. See also Fig. 5. We reclassified it as a lenticular (SA0) galaxy based on the decomposition in Fig. 9.

3.4 Morphological reclassifications

We are able to reclassify the morphology of the host galaxies based on our decomposition of their light. The previous morphologies were determined by visual inspection of photographic images (Dressler 1980; Sandage, Binggeli & Tammann 1985; Binggeli, Tammann & Sandage 1987; de Vaucouleurs et al. 1991), which can drown out features and limit the accuracy of the past classifications. For instance, a faint disc in an early-type galaxy can be hard or impossible to see in images at certain fixed contrasts. In the case of a face-on disc, from a photograph, it is very difficult to distinguish a barless lenticular galaxy from an elliptical galaxy. For this reason, in our search for compact massive spheroids, we have not restricted the initial galaxy sample to galaxies classified as either lenticular or spiral.

Many, and no doubt most, galaxies classified as elliptical are either lenticular or ellicular galaxies with discs and bulges. Analysing the surface brightness profiles is much more reliable for identifying host galaxy substructures due to the bumps and bends in the profiles. Our decompositions, therefore, provide a more complete picture of the host galaxies than past visual inspections. The new information will be particularly valuable to understand the morphological evolution of galaxies.

Among the 28 initially elliptical galaxies (E, according to the RC3), 64 per cent (18/28) of them are relabelled as lenticular galaxies (S0). Two of the original S0s are now classified as ellicular galaxies (ES): NGC 3805 and NGC 5382.

We present one such 'elliptical galaxy', NGC 4008, to illustrate why we reclassified it as an S0 galaxy instead of an E galaxy. NGC 4008 was classified as an 'E5' in RC3. Fig. 8 shows the galaxy, our model, and our residual image of NGC 4008. The galaxy has a central stellar velocity dispersion of $\sigma_0 \sim 208$–$240\,\mathrm{km\,s^{-1}}$ (Faber et al. 1989; Simien & Prugniel 2002). In its ellipticity profile (ϵ, middle panel in Fig. 9), one can see that the ellipticity reaches $\epsilon \sim 0.4$, and the surface brightness profile (μ, top panel in Fig. 9) has a smooth exponential decline from $R_{\rm eq} \sim 20$ arcsec. Although the PA and B_4 seem to be featureless, the galaxy has clear signs of an extended disc. Simien & Prugniel (2002) found the stellar velocity to be $v = 123\ \mathrm{km\,s^{-1}}$ at $R = 10$ arcsec (in major axis) and appear to keep rising beyond this point. We first tried to use a Sérsic bulge plus an exponential disc to model the galaxy, but we found that it can

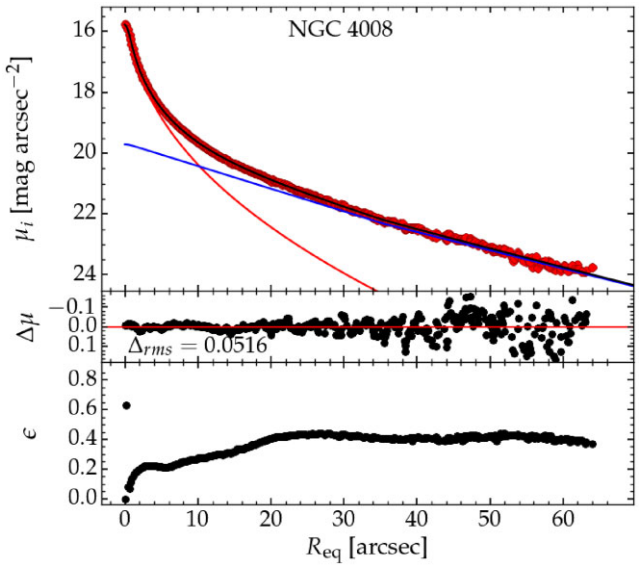

Figure 9. NGC 4008's surface brightness profile in 'equivalent axis' (circularized radius). See also the general description in Fig. 6 for reference. The profile is fitted with a bulge (red line in the top panel) and a disc (blue line in the top panel).

be better described with a bulge (top panel in Fig. 9, red line) and a Type III exponential disc with a slight slope difference separated at $R_{\rm eq} = 35$ arcsec (top panel in Fig. 9, blue line). The final fit is an excellent agreement with the isophotal model and has a root mean square residual $\Delta_{\rm rms} = 0.0516\,\mathrm{mag\,arcsec^{-2}}$ (see the middle panel in Fig. 8). This decomposition also aligns with Simien & Prugniel (2002), who show that at $R_{\rm eq} > 10$ arcsec, NGC 4008 transitions from bulge-dominant to disc-dominant. The presence of an extended disc means NGC 4008 is not an 'E5' but an 'SA0' galaxy. There are 17 other galaxies similar to NGC 4008 where we reclassified them as S0.

Two other galaxies are worthy of note. NGC 4459 was the only galaxy originally labelled as an S0 prior to our changing it to an E2 designation. It contains a nuclear disc in the centre, as reported

by Peterson (1978) and Krajnović et al. (2011). Gutiérrez et al. (2011) has suggested that it contains a Type III antitruncated disc. Savorgnan & Graham (2016a) broke down the galaxy into a Sérsic bulge, a Gaussian nucleus (for the nuclear disc), and an exponential disc. However, the neighbouring disc galaxy is likely the main contribution to the light in the 'extended disc' at large radii. As we limit the fitting range to within 77 arcsec along the major axis, a nuclear exponential disc and a Sérsic bulge are found to suffice. Additionally, we sustain the E classification for NGC 2872, but it is noteworthy that it contains a dusty nuclear disc (as shown in Tran et al. 2001).

In summary, only eight elliptical galaxies (NGC 2832, NGC 3615, NGC 3812, NGC 4073, NGC 4261, NGC 4555, NGC 4889, and NGC 5444) in our sample are devoid of (detectable) discs, while three of them have nuclear discs (NGC 2872, NGC 4459, and NGC 4494) and two have intermediate-scale discs (NGC 3805 and NGC 5382). The abundance of pure elliptical galaxies is much lower than the morphologies previously indicated. In total, it leaves five E galaxies in Bin 1, three in Bin 2, and three in Bin 3. True elliptical (E+ES) galaxies occupy only ∼13 per cent (13/103) of our sample,[17] and they are only ∼0.46 per cent (13/28) old E class objects. This equates to an E+ES galaxy number density in Bins 1, 2, and 3 of $1.84 \times 10^{-5}\,\mathrm{Mpc}^{-3}$, $3.39 \times 10^{-5}\,\mathrm{Mpc}^{-3}$, and $9.20 \times 10^{-5}\,\mathrm{Mpc}^{-3}$, respectively.

This result is comparable to the ATLAS^{3D} kinematic analysis of 260 nearby early-type galaxies (Cappellari et al. 2011a, b; Emsellem et al. 2011; Krajnović et al. 2011, 2013a). Studying a volume-limited sample within <40 Mpc, Emsellem et al. (2011) reveal only ∼14 per cent (36/260) of their early-type galaxies are 'slow-rotators', defined by a luminosity weighted specific angular momentum $\lambda_R \leq 0.1$ (see Emsellem et al. 2007). They found that one-third (∼34 per cent) of the previously classified elliptical galaxies are slow rotators, and ∼47 per cent (17/36) of them contain a kinematically distinct core (KDC). We share a mutual sentiment that reclassification is needed for many early-type galaxies. Indeed, Cappellari et al. (2011b) advocated the kinematic classification scheme from Bender (1988a) and Capaccioli & Caon (1992) to correct for the misunderstanding caused by the old visual-based classification. Although, as illustrated in Bellstedt et al. (2017), this kinematic scheme fails to accommodate the ES galaxies which are either fast or slow rotators depending on the radial extent of one's observations, it does help identify which early-type galaxies have discs and therefore require a decomposition to measure the size and mass of the spheroidal component.

3.5 Spheroid colours

Local early-type galaxies typically, although not universally, exhibit a negative colour gradient such that they are redder in their centre than their outskirts (e.g. Franx, Illingworth & Heckman 1989a; Peletier et al. 1990; Gargiulo et al. 2012; Peletier et al. 2012; Marian et al. 2018). In the absence of substantial dust and gas, a negative gradient suggests younger (more blue) stellar population in the outer regions, which can be a sign of inside-out disc growth. However, from galaxy colour profiles, it can be problematic to readily establish the colours of the individual overlapping structural components. For instance, a young nuclear disc can make a galaxy core colour blue and result in a more positive galaxy gradient than compared to the surrounding red quiescent spheroid (e.g. Graham et al. 2017).

While we would like individual $g - i$ colours for the bulges, or better yet, the spectral energy distributions of the bulges for use in software like MAGPHYS (da Cunha et al. 2012) to obtain the stellar mass, we make use of the galaxy colours, recognizing that there is not a big difference between bulge and disc colours of early-type galaxies and early-type disc galaxies (e.g. Peletier & Balcells 1996). Our galaxies have a mean $g - i$ colour of ∼1.2, in accord with the value reported in Fukugita et al. (1996) for what they thought were elliptical galaxies, but undoubtedly included many S0 galaxies.

In general, the bulges of galaxies are redder than their discs (Bothun & Gregg 1990; Peletier et al. 1999). For bright red galaxies, Kennedy et al. (2016, see their figs 10–13) find $u - r$ bulge colours ∼0.5 mag redder than the disc colours, although they remind the reader that they performed a bulge-disc decomposition of every galaxy regardless of whether there was a physical need for two components. As such, their colour difference will also capture metallicity gradients in disc-less elliptical galaxies. However, for some of our galaxies with bulges, their galaxy $g - i$ colour might be bluer (a smaller value) than the bulge colour.

Our use of the galaxy colour in the MLCRs to derive the stellar mass of the bulge might, therefore, underestimate the stellar mass of the bulges. Although, Vika et al. (2014, see their fig. 10 and table 2) report that E-S0-Sa galaxies tend to have bulges and discs with a similar $(g - i)$ colour (see also Peletier & Balcells 1996). Using morphologically classified galaxies, they find it is the Sb and later spiral galaxies that have notably bluer discs than their bulges, with average $(g - i)$ disc colours that are 0.3 mag bluer than their bulges. Throughout this work, we use the galaxy colour as a proxy for the bulge/spheroid colour. The effect of underestimating how red any bulge is will be to underestimate the M_*/L ratio assigned to that bulge and thus underestimate the stellar mass of that bulge. That is, the number density of local, massive, compact spheroids will not be erroneously overestimated due to this issue.

In an effort to check on this matter, in Fig. 10, we compare the galaxy $(g - i)_{\mathrm{gal}}$ colour with the SDSS point-spread function (PSF) $(g - i)_{\mathrm{PSF}}$ colour. Fig. 10 reveals how some galaxies with a global $(g - i)_{\mathrm{gal}} \sim 1.2 \pm 0.1$ mag have relatively blue cores. The PSF magnitude is obtained by fitting a point-spread function to the light source, stars, and galaxies alike (see in Stoughton et al. 2002). A PSF is a good description for point sources like stars, but not so for extended sources like galaxies. The PSF fit on the galaxies should mainly sample the spheroidal part of the galaxies. PSF size variation is biased to the red. We highlighted those with unique central components in Fig. 10. The sample with a nuclear disc is marked with blue crosses. Other prominent central components, such as nuclear rings, secondary bar, and AGN are marked with cyan crosses.

All of this simply provides a rough guide for what the error in the spheroid colour may be. Of the 103 galaxies in our sample, 69 have PSF magnitude available in the NED data base. The median difference between $(g - i)_{\mathrm{gal}}$ and $(g - i)_{\mathrm{PSF}}$ is 0.09 mag and the standard deviation ±0.26 mag. Most galaxies reside at $1.0 < (g - i)_{\mathrm{gal}} < 1.5$ along the dashed centre line. Some of the major outliers can be explained by the influence of prominent central components, as evidenced by the four galaxies at $(g - i)_{\mathrm{PSF}} < 0.9$ mag and the one with $(g - i)_{\mathrm{PSF}} > 1.8$ mag. One outlier deviates from the centre line significantly at $(g - i)_{\mathrm{gal}} \sim 1.8$ mag and $(g - i)_{\mathrm{PSF}} \sim 0.8$ mag. This galaxy is UGC 8736 (marked with a red cross in Fig. 10). Its image has severe foreground contamination. The galaxy is situated next to a bright star. We suspect its PSF colour might not be accurate due to

[17] Among the true ellipticals, there are six cD galaxies: NGC 2832, NGC 4073, NGC 4874, NGC 4889, NGC 4914, and NGC 5444. NGC 4914 is relabelled as a SAB0 galaxy, for its weak bar (Buta et al. 2010) and an extended disc with $\epsilon \sim 0.4$. Informed by the three components model by Dullo (2019), NGC 4874 is now labelled as SA0 (see later in Section 4.1).

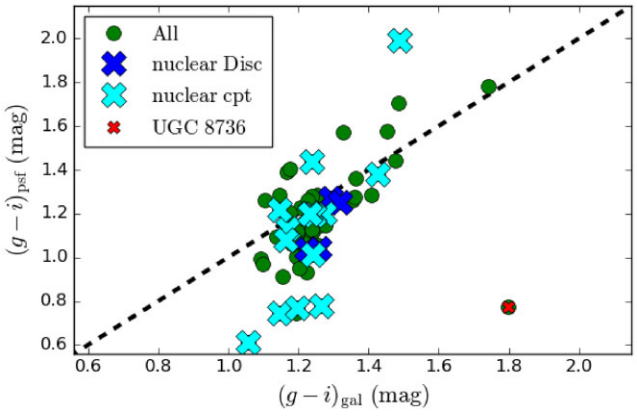

Figure 10. The comparison between galaxy colour difference $(g-i)_{\rm gal}$ and SDSS PSF colour difference $(g-i)_{\rm psf}$. The dashed black line is the centre line where $y = x$. The galaxies that contain a nuclear disc are marked with blue crosses. Those containing other prominent nuclear components, such as a nuclear ring, secondary bar, or AGN, are marked collectively with cyan crosses, labelled as 'nuclear cpt'. The particular outlier UGC 8737 is marked with a red cross.

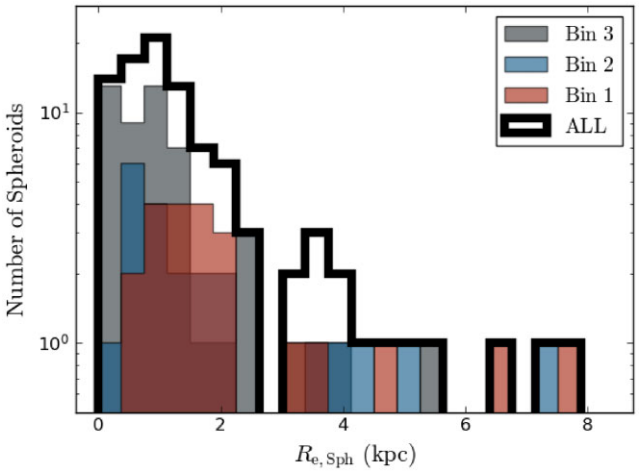

Figure 11. The size ($R_{\rm e,\,Sph}$, in equivalent axis) distribution of our bulges/spheroids. The spheroids from Bins 1, 2, and 3 are depicted by the red, blue, and black histograms, respectively. The thick black line depicts the size distribution of the entire sample set. The figure only shows the 96 spheroids with $R_{\rm e,Sph} < 10$ kpc of the complete sample, see the spheroids' size–mass distribution later in Section 4.3 for further reference.

such an influence. The galaxy $(g-i)_{\rm gal}$ colour provides a reasonable estimation of the spheroid $(g-i)$ for our purpose.

Given that galaxies do not have $g-i$ colours redder than $\sim$1.5 (e.g. T11), we recognize the five galaxies[18] in our sample with a $g-i$ colour of $\sim$1.8 as erroneous, perhaps due to dust or a poor single Sérsic fit to obtain the $g-$ and $i-$ 0band magnitudes. We reset these galaxies $g-i$ colour to 1.5 so as to not overestimate the stellar mass-to-light ratio used and thus not overestimate the galaxies' stellar mass. We move on to calculate the stellar masses of the spheroids accordingly.

3.6 Spheroid masses

Multiple high-z red nugget studies (Barro et al. 2013; van der Wel et al. 2014; van Dokkum et al. 2015) use the SED fitting code FAST (Kriek et al. 2009) to determine the stellar masses of their high-z galaxies. These works assume the Chabrier (2003) IMF and Bruzual & Charlot (2003, hereafter BC03) SPS, with a variety of dust extinction treatments. Among the available MLCRs, only the T11 and RC15 relations are constructed with these priors. For the sake of simplicity, the result will be presented in RC15 stellar mass. However, to ensure the result is not biased by the choice of stellar mass measurements, the effect of using the different MLCRs will be later discussed in Section 6.1.2.

Our final uncertainty on the stellar masses have been calculated using the following error propagation equation:

$$\delta \log_{10} M_* = \sqrt{\left(\frac{\delta \mathfrak{m}}{2.5}\right)^2 + \left(2\frac{\delta D}{D\ln(10)}\right)^2 + \left(\frac{\delta \Upsilon_*}{\Upsilon_* \ln(10)}\right)^2}, \quad (10)$$

where δD is our assumed uncertainty in the distance, $\delta\mathfrak{m}$ is our uncertainty in the bulge apparent magnitude, and $\delta\Upsilon_*$ is our uncertainty in the M_*/L ratio. The uncertainty in the magnitude, $\delta\mathfrak{m}$, is determined by the component modelling process. The unknown degeneracy amongst components is the primary source of error. As explored in Savorgnan & Graham (2016a), adding or subtracting a galaxy component can change the spheroid parameters. Based on our extensive practical experience with the fitting routine, and informed by the results of previous studies (Savorgnan & Graham 2016a; Davis et al. 2019; Sahu et al. 2019), we have assigned a probable magnitude error of $\delta\mathfrak{m} = 0.3$ mag for all of our spheroids. This level of uncertainty encapsulates the average error commonly encountered throughout the combined efforts of this work and its predecessors. The uncertainty in the mass-to-light ratio is taken to be the intrinsic scatter of each MLCR, as recorded in Section 2.3. The error in distance is taken directly from their respective measurement sources (see Appendix A).

3.7 Bulge sizes

We present the bulge/spheroid size (in equivalent axis, $R_{\rm e,\,Sph}$) distribution in Fig. 11. The spheroids from Bin 1, 2, and 3 are depicted with red, blue, and black filled histograms, respectively. The median size $\langle R_{\rm e,\,Sph}\rangle$ for Bin 1, 2, and 3 are 1.7, 1.2, and 0.8 kpc, respectively. The majority of our spheroids (96/103, 93 per cent) are smaller than $R_{\rm e,Sph} < 7$ kpc.

Over time, as the stars in galaxies evolve and eject their stellar winds, the amount of dust builds up, at least in late-type galaxies where dust sputtering does not operate efficiently. While the presence of dust is known to reduce the apparent bulge and disc magnitudes, and increasingly so with a more edge-on disc inclination (i), the impact on the effective half-light radius of the bulge is not well known. An investigation of how $R_{\rm e}$ changes with i, at different wavelengths, would be welcome. Ideally, this information would be known for different galaxy morphological types.

The dust is known to be more centrally concentrated in galaxies than in their outskirts. Qualitatively, this acts to reduce the inner flux relative to the outer flux, which has the effect of increasing the half-light radius of the galaxy, and the disc component of the galaxy (e.g. Graham & Worley 2008, see their fig. 2). It is not known how much the apparent half-light radius of the bulge increases, however,

[18]The five outliers are: UGC 8736, NGC 4527 NGC 3718, NGC 2968, and NGC 2894. All of which are spiral galaxies from Bin 3. We marked their spheroids in Fig. 15 with black star signs (⋆). Three of them contains a low mass spheroids ($M_*/{\rm M}_\odot < 1\times10^{10}$). Only two lie within a 'compact massive' region. The outliers does not alter the number of compact massive spheroids, nor the shape of the spheroids distribution in any significant way.

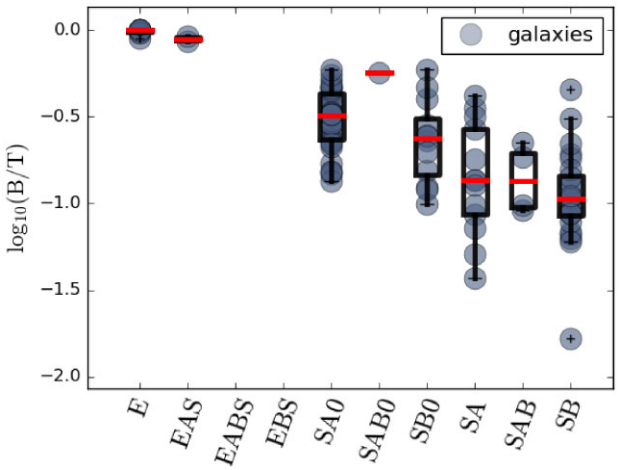

Figure 12. SDSS *i*-band Bulge-to-Total (B/T) flux ratios. The spiral (SA–SB) galaxies presented here are dominated by the so-called 'early-type' spirals (Sa–Sb). The boxes denote the lower (Q1) to upper (Q3) quartiles of the data, and the whiskers extend from the minimum to the maximum data points (excluding any outliers). The red lines represent the median $\langle B/T\rangle$ ratios for each morphology. The ' + ' marker denotes an outlier (NGC 5350) that lies beyond the Q1 − 1.5(Q3 − Q1) limit (Tukey 1977).

the effect is such that we may be underestimating the true number of local, compact spheroids.

Combined with potentially underestimating the masses of the bulges, we move forward in the knowledge that we are presenting a conservative estimate of the number density of compact massive spheroids. That is, these potential biases do not act to overestimate the number density.

4 RESULTS

We present our result in the following subsections: Section 4.1 showcase the bulge-to-total flux ratio (B/T) newly obtained from multicomponent decomposition; Section 4.2 shows the bulge/spheroid mass function; and Section 4.3 present the size–mass relation of the local spheroids and the number of compact massive spheroids under different definitions.

4.1 Bulge-to-total (B/T) flux ratios

We present the *i*-band bulge-to-galaxy flux ratios in Fig. 12, plotted against by their morphologies. Our flux ratios are the observed (no internal dust correction) ratios taken from the equivalent-axis decompositions. For simplicity, we have applied the same M_*/L ratio to all galaxy components; this poses a slight limitation and is an area where future improvements can be made. However, we note that the (dust-free) colours of bulges and discs are, in general, not too dissimilar from each other in massive disc galaxies (Peletier & Balcells 1996). As such, the M_*/L ratio will typically, although not necessarily, be similar. The grey points indicate the bulge-to-total (B/T) flux ratios for individual galaxies while the red line is the median ratio in each subgroup. We obtained a disc-dominated median $\langle B/T\rangle \pm 1\sigma \approx 0.33 \pm 0.15$ for the S0 galaxies (49 in sample). Our spiral galaxies exhibited a notably lower median ratio of $\approx$0.13 ± 0.12, (41 in sample). In both cases, the barred galaxies consistently have a lower B/T ratio than the unbarred galaxies.

In Table 4, we present the median $\langle B/T\rangle \pm 1\sigma$ value for each morphological type from each bin. The two unbarred ES galaxies have an average $\langle B/T\rangle \pm 1\sigma \approx 0.86 \pm 0.02$. While this simply reflects the range of masses and galaxy types, it is important for understanding the transition from galaxy to spheroid mass at the high-mass end of the galaxy stellar-mass function.

Our inclusion of minor components, such as nuclear discs, spiral arms, lenses, and secondary bars can change the B/T ratio. This is not so much because of the flux held in these components but because of how their presence can skew the galaxy decomposition if they are not properly accounted. Although one may expect this to decrease the B/T ratio, it is more complicated than that. For example, the more sophisticated models, which can involve truncated-exponential discs rather than a single exponential disc model, can result in a fainter central disc surface brightness and thus a greater assignment of flux to the bulge if the single-disc model was biased by the outer disc profile. We have 32 truncated discs in our sample: 14 Type II (downward-bending) and 18 Type III (upward-bending) discs. Echoing the same point made by Kim et al. (2014b), which claimed that ignoring Type II disc breaks will result in an $\approx$10 per cent decrease in the B/T ratio, we agree that broken, and inclined, exponential disc models play an important role in correctly modelling a galaxy. Contrarily, the application of these more sophisticated disc models to Type III discs can be expected to decrease the B/T ratio, compared to the result using a single exponential model, if the single-disc model is biased by the outer disc slope.

In Fig. 13, we show the distribution of B/T ratio and the stellar mass of the spheroids ($M_{*,\rm Sph}/\rm M_\odot$, upper panel) and the galaxies ($M_{*,\rm gal}/\rm M_\odot$, lower panel), separated by their morphology. The outliers: NGC 3158 (S0), and NGC 4874 (S0)[19] are labelled individually in the lower panel. Similar to Fig. 12, E+ES galaxies occupy the high B/T region, between $0.8 \lesssim B/T < 1.0$, while S0 and S galaxy have a $B/T \lesssim 0.6$. Note that E galaxies do not have $B/T = 1$ exactly due to the presence of nuclear discs and other components. Regardless of their B/T ratio and morphological type, most[20] of our galaxies span the galaxy stellar mass range of $6 \times 10^{10} \lesssim M_{*,\rm gal}/\rm M_\odot(RC15) < 1.5 \times 10^{12}$. It appears that many S0 galaxies, as well as a smaller amount of S galaxies, can be as massive as $M_{*,\rm gal}/\rm M_\odot$ (RC15) $>2 \times 10^{11}$. Spheroids follow a positive correlation between B/T ratio and spheroid mass by morphology where S galaxies tend to have less massive bulges than S0 galaxies (see the upper panel of Fig. 13).

The lack of a strong correlation between B/T ratio and galaxy stellar mass is reminiscent to the result from Méndez-Abreu et al. (2017), where they performed detailed 2D multicomponent decomposition

[19]The two S0 galaxy outliers are particularly massive ($M_{*,\rm gal}/\rm M_\odot > 7 \times 10^{11}$). The MASSIVE survey (Veale et al. 2017) confirms our stellar mass calculation, where in their table 1, NGC 3158 and NGC 4874 reports a galaxy stellar mass of $M_{*,\rm gal}/\rm M_\odot \sim 1.05 \times 10^{12}$ and $M_{*,\rm gal}/\rm M_\odot \sim 9.54 \times 10^{11}$, respectively. Similar to our classification, Veale et al. (2017) labelled NGC 3158 as a 'fast rotator'. For NGC 4874, according to the multicomponent decomposition in Dullo (2019), it contains three components, an inner core-Sérsic bulge, an intermediate component, and an outer exponential halo. The intermediate component is dominant between ∼10 and ∼100″. In their $F606W - F814W$ colour map (their fig. 2), the colour becomes gradually bluer towards larger radii. We found that an exponential component can describe the intermediate component well. The outer envelope comes into play beyond our cut-off radius of 90″ in the major axis and was therefore not required in our decomposition

[20]Some (13/103) galaxies are below our lower mass selection limit in ($M_*/\rm M_\odot$ (RC15) $= 6.7 \times 10^{10}$). This is somewhat expected because SDSS *i* −band total galaxy magnitude is measured using a single Sérsic function, while ours is measured by a multicomponents model (Bulge+Disc + others). For galaxies with prominent discs (S0 & S), a single Sérsic model can overestimate the size and luminosity of the galaxy (see later in Fig. C1). The implication of which, however, shall be better explored in future works.

Table 4. The Bulge-to-Total (B/T) flux ratio of our galaxy sample. This table presents the median flux ratio $\langle B/T \rangle$ and the 1σ range for each morphological type in each of our three volume bins. The number in parentheses is the sample size for each subdivision, i.e. median $\langle B/T \rangle \pm 1\sigma$ (sample size).

	E	EAS	SA0	SAB0	SB0	SA	SAB	SB
Bin 1	$1.0^{+0.0}_{-0.01}$ (5)	0.86 (1)	$0.33^{+0.15}_{-0.17}$ (13)	−− (0)	$0.25^{+0.10}_{-0.10}$ (2)	0.19 (1)	$0.19^{+0.03}_{-0.06}$ (3)	$0.10^{+0.01}_{-0.01}$ (2)
Bin 2	$1.0^{+0.0}_{-0.04}$ (3)	0.92 (1)	$0.30^{+0.14}_{-0.06}$ (9)	0.56 (1)	$0.53^{+0.04}_{-0.04}$ (2)	$0.2^{+0.08}_{-0.08}$ (2)	0.10 (1)	$0.09^{+0.05}_{-0.01}$ (5)
Bin 3	$1.0^{+0.0}_{-0.02}$ (3)	−− (0)	$0.33^{+0.12}_{-0.10}$ (14)	−− (0)	$0.21^{+0.03}_{-0.09}$ (8)	$0.13^{+0.18}_{-0.10}$ (10)	−− (0)	$0.11^{+0.10}_{-0.04}$ (17)
Total	$1.0^{+0.0}_{-0.07}$ (11)	$0.89^{+0.02}_{-0.02}$ (2)	$0.32^{+0.14}_{-0.10}$ (36)	0.57 (1)	$0.24^{+0.18}_{-0.11}$ (12)	$0.14^{+0.18}_{-0.07}$ (13)	$0.14^{+0.06}_{-0.05}$ (4)	$0.11^{+0.08}_{-0.04}$ (24)

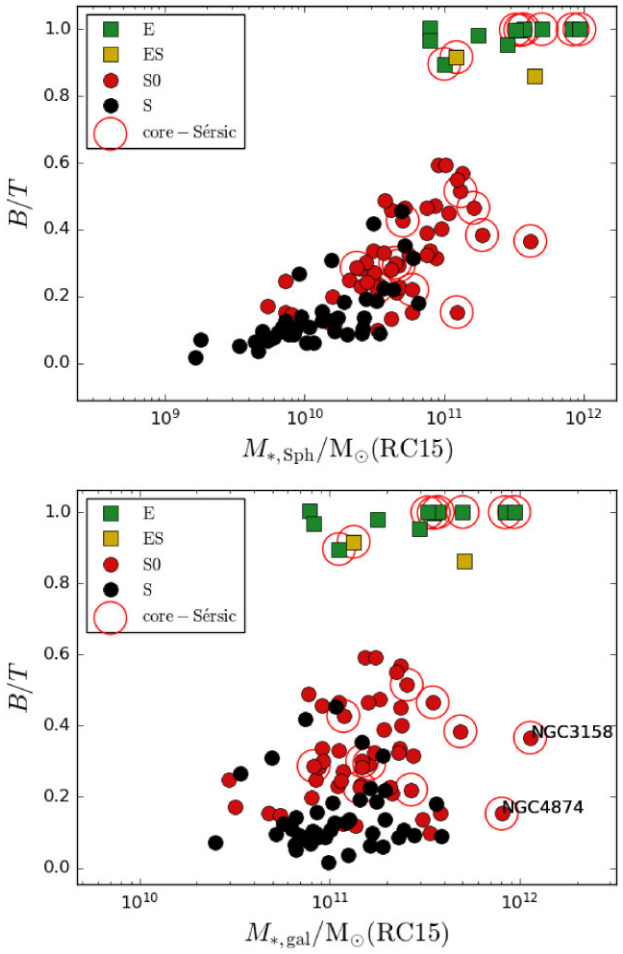

Figure 13. The bulge-to-total (B/T) flux ratio-versus-spheroid stellar mass ($M_{*,\mathrm{Sph}}/\mathrm{M}_\odot$, upper panel) and galaxy stellar mass ($M_{*,\mathrm{gal}}/\mathrm{M}_\odot$, lower panel). We labelled the data points from E, ES, S0, and S galaxies as green squares, yellow squares, red points, and black points, respectively. Bulges modelled by core-Sérsic function are marked by red circles while the rest are modelled by Sérsic function. The outliers: NGC 3158 (S0) and NGC 4874 (S0) are marked by their name in the plots.

(including nuclear, bar, and broken disc components) to 404 galaxies from the Calar Alto Legacy Integral Field Area (CALIFA; Sánchez et al. 2016) data. They presented the mean $\langle B/T \rangle \pm 1\sigma$ value for S0, Sa, and Sb to be $\sim 0.32 \pm 0.17, 0.28 \pm 0.17, 0.12 \pm 0.11$, respectively. The mass of their S0, Sa, and Sb galaxies occupy a similar range of $\langle \log_{10}(M_*/\mathrm{M}_\odot) \rangle \pm 1\sigma \sim 10.79 \pm 0.6$, 10.80 ± 0.4, and 10.48 ± 0.4, respectively. It has been shown that, if the bar component is not considered, the bulge's Sérsic index n and the B/T ratio will be overestimated (Gadotti 2009; Salo et al. 2015). The rather low median B/T ratio ($B/T \sim 0.1$–0.3) in both massive S0 and S galaxies reflect a reality that stellar discs and their induced structures take up the majority of the mass budget (see also, Laurikainen et al. 2005).

4.2 Spheroid stellar mass function

We present the high-mass end of the local bulge/spheroid stellar mass function in Fig. 14. It includes bulges in the mass range $2 \times 10^9 \lesssim M_*/\mathrm{M}_\odot$ (RC15) $\lesssim 1.5 \times 10^{12}$. To our knowledge, these results are the first of their kind derived from highly detailed, multicomponent decompositions on a volume- and mass-limited sample. For each Bin (1 to 3), the mass function is constructed by counting the number of spheroids per 0.3 dex range in mass, then dividing that number by 0.3 and by the volume of the associated Bin (1 to 3).

Based on the B/T flux ratios from Section 4.1, we use the individual galaxy B/T ratios in each bin to estimate the median $\langle B/T \rangle \pm 1\sigma$ range for each bin. They are:

(i) Bin 1 ($\langle B/T \rangle \sim 0.33 \pm 0.32$): E (5), EAS (1), SA0 (13), SB0 (2), SA (1), SAB (3), and SB (2);
(ii) Bin 2 ($\langle B/T \rangle \sim 0.29 \pm 0.30$): E (3), EAS (1), SA0 (9), SAB0 (1), SB0 (2), SA (2), SAB (1), and SB (5); and
(iii) Bin 3 ($\langle B/T \rangle \sim 0.21 \pm 0.22$): E (3), SA0 (14), SB0 (8), SA (10), and SB (17).

While we have a well-defined stellar mass 'selection limit' for the galaxies, it is unclear to what completeness the spheroid mass function is covered below this limit. Spheroids/bulges more massive than the 'selection limit' cutoff are of course accounted for, but since we did not sample galaxies below the limit, the spheroid mass function is only 'partially complete' at lower masses. For instance, a massive galaxy of $M_{*,\mathrm{gal}} \sim 2 \times 10^{11}\,\mathrm{M}_\odot$ with $B/T = 0.1$ will have a bulge of $M_{*,\mathrm{Sph}} \sim 2 \times 10^{10}\,\mathrm{M}_\odot$, below our selection limit. Our sample provides a good representation for embedded spheroids coming from galaxies more massive than $6.7 \times 10^{10}\,\mathrm{M}_\odot$ (RC15), but increasingly less so for less massive spheroids. For example, a less massive galaxy ($M_{*,\mathrm{gal}} \sim 4 \times 10^{10}\,\mathrm{M}_\odot$, outside of the limit) with a bulge-to-total ratio $B/T \sim 0.5$ will also have a spheroid of the same stellar mass as above ($M_{*,\mathrm{Sph}} \sim 2 \times 10^{10}\,\mathrm{M}_\odot$), but it will not be in our sample. We refer to the region below the 'selection limit' as the 'partially complete region'. The number of spheroids found in this mass range represents a lower limit to the true number.

We estimate a rough lower bound to this 'partially complete region' by multiplying the galaxy mass limit (see Table 2) by the average $\langle B/T \rangle$ ratio for the galaxies with masses greater than this limit. This provides the following rough lower bound to the spheroid stellar masses (when using the M/L prescription from RC15) for each bin: $1.12 \times 10^{11}\,\mathrm{M}_\odot$ (Bin 1), $3.77 \times 10^{10}\,\mathrm{M}_\odot$ (Bin 2), and $1.54 \times 10^{10}\,\mathrm{M}_\odot$ (Bin 3). Between the galaxy mass limit and these lower values, our spheroid mass function is only partially complete. Above the galaxy mass limit, our numbers are complete. The galaxy mass 'selection limit' has been depicted by the colour-coded solid bars,

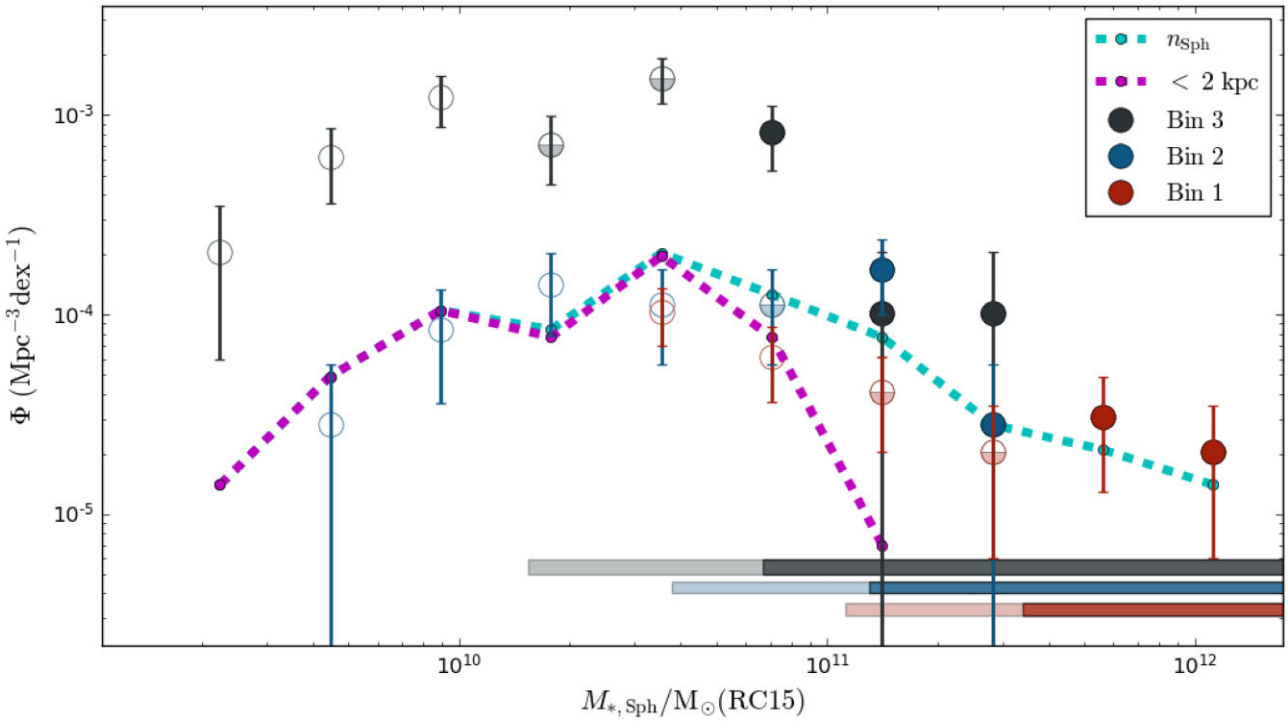

Figure 14. The local bulge/spheroid 'stellar mass' function, with the stellar mass defined using the RC15 MLCR. The red, blue, and black points represent the spheroid sample from the three 'galaxy mass bins' 1, 2, and 3, respectively (see Fig. 3). The spheroid stellar masses are divided into 0.3 dex mass bins. The error bars represent the Poisson error. The cyan dashed line, labelled '$n_{\rm Sph}$', is the lower limit of the number density for each mass interval, obtained by summing up the total number of spheroids in each interval and dividing it by the total volume of our selection space. The purple dashed line, labelled '< 2 kpc', is the same as the cyan line but including only the spheroids with $R_{\rm e} < 2$ kpc (in equivalent axis). The three colour-coded bars in the bottom right represent the mass range of confidence, in which the solid bars depict the mass 'selection limit' from the host galaxies, and the transparent bars depict a 'partially complete' region. The points in the 'selection limit' are plotted in solid circles, the ones in the 'partially complete' region are in half-filled circles, and the ones below these regions are in open circles. The spheroid mass function is complete down to each host galaxies' 'selection limit' where all the hidden spheroids within this range are accounted. In the 'partially complete' region, our sample includes all spheroids coming from high-mass galaxies ($M_*/{\rm M}_\odot \gtrsim 0.7$–$3.0 \times 10^{11}$) with low B/T ratios, but not the spheroids coming from low-mass galaxies ($M_*/{\rm M}_\odot \sim 0.18$–$1.5 \times 10^{11}$) with high B/T ratios. Since Bin 1 has a volume of 3.25×10^5 Mpc^3, 1 object per 0.3 dex range of spheroid mass will give a number density of $\Phi \approx 1 \times 10^{-5}$ Mpc^{-3}dex^{-1}. See Table 1 for the volume of each bin.

and the 'partially complete region' by the semitransparent colour-coded bars, in the lower right of Fig. 14. The data points above the 'selection limit' are shown with solid circles, while those in the 'partially complete region' are shown using transparent half-filled circles, while those less massive than that are depicted using open circles.

Given that Bin-1 has a volume of 3.25×10^5 Mpc^3, a count of 1, 2, 3, or 4 objects per 0.3 dex range in spheroid mass will result in a number density of $\approx$1, 2, 3, or 4×10^{-5} Mpc^{-3} dex^{-1}. The number densities coming from the smaller volumes of Bin-2 and Bin-3 will be roughly 3 and 10 times greater for the same number of objects per 0.3 dex in spheroid mass. As can be seen in Fig. 14, there is a rising number density from $\sim 2 \times 10^{-5}$ Mpc^{-3} dex^{-1} at 10^{12} M$_\odot$, to $\sim 10^{-4}$ Mpc^{-3} dex^{-1} at 10^{11} M$_\odot$, and reaching $\sim 10^{-3}$ Mpc^{-3} dex^{-1} by 0.7×10^{11} M$_\odot$. Bin-3, which is more complete at lower masses, reveals a lower limit to the number density of $\sim 10^{-3}$ Mpc^{-3} dex^{-1} at 10^{10} M$_\odot$.

We present the overall mass function across the three bins using a dashed cyan line in Fig. 14, obtained by summing up the number of spheroids in each mass interval from all three bins and dividing them by the total survey volume (4.76×10^5 Mpc^3) and then by 0.3 dex. The purple dashed line depicts the overall mass function of small spheroids with $R_{\rm e} < 2$ kpc (equivalent axis). The overall mass function serves as a lower limit of spheroids in each mass interval. At stellar masses above $M_{*,\rm Sph}/{\rm M}_\odot$ (RC15) $\sim 1.5 \times 10^{11}$, there are no spheroids smaller than 2 kpc in our sample. However, there is no strict definition in the literature for 'compact massive' galaxies. To better explore the situation requires us to next look at the size–mass diagram.

4.3 Size–mass relation of the local spheroids

In the top left-hand panel of Fig. 15, we show the distribution of local spheroids in terms of their (equivalent axis) effective half-light radius $R_{\rm e,\,eq}$ and their stellar masses derived from the RC15 MLCR, assuming a BC03 SPS. The spheroids are colour-coded according to the volume-bins (1, 2, and 3) shown in red, blue, and black, respectively. We plot our spheroids against the opaque grey cloud of the general population of bright SDSS galaxies, consisting of both early- and late-type galaxies. It is clear that, for a given mass, the local spheroids are considerably more compact than most galaxies. As expected, the spheroids extracted from Bin 3, with their lower galaxy mass-boundary, occupy the lower to the medium mass range, and the giant spheroidal elliptical galaxies reside in the (high mass)–(large radius) region of the diagram.

In the other panels, we report the number density (n (Mpc^{-3})) based on different selection criteria. The arbitrary selection boundary often contains a diagonal line separating the sample into 'compact' and 'non-compact' systems, with a lower mass limit.

The compactness criteria are as follows:

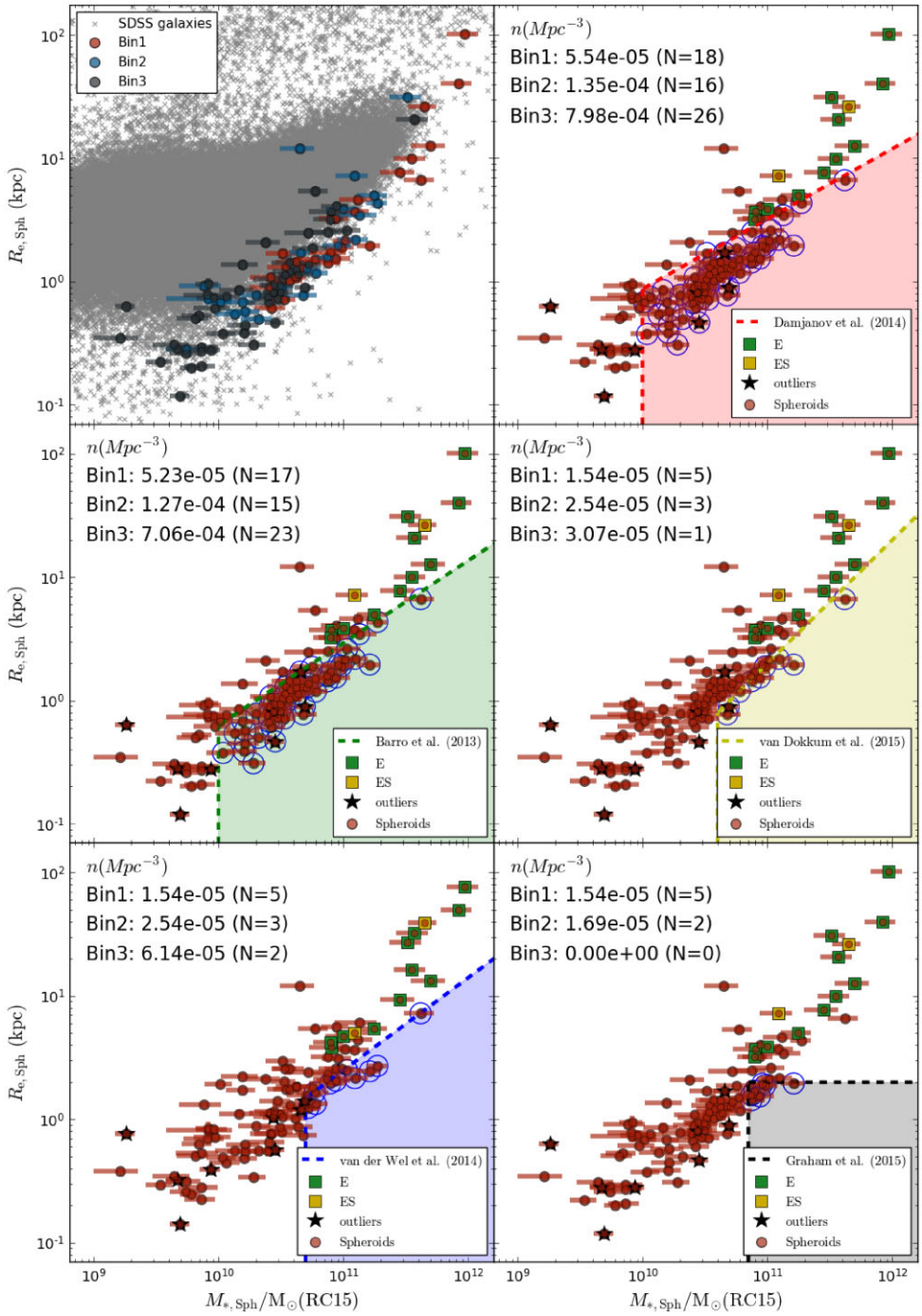

Figure 15. Size–mass distribution for our local spheroids (marked as •). The stellar masses of the local spheroids are calculated via the RC15 MLCR. The effective half-light radii for the local spheroids come from their geometric mean axes, with the exception that the major-axis half-light radii have been used in the bottom left-hand panel to provide a better comparison with van der Wel et al. (2014). In the top left-hand panel, we have the size–mass distribution separated by our three-volume bins, shown against the SDSS galaxy sizes and stellar masses (×). The SDSS galaxy radius and flux data are taken from the NASA-Sloan ATLAS catalogue (see description in Section 2). We calculate their stellar mass using the same MLCR as our spheroids, in this case, with the RC15 equation. The other plots illustrate some of the different 'compactness' criteria used in the literature. The number of galaxies (N) that satisfied the conditions in each bin and the corresponding number densities (n) are shown in the panels. These are, of course, lower limits to the true number density of local compact massive spheroids due to the lower galaxy-mass limits used to construct each bin. The compactness criteria are from: Damjanov et al. (2014) (top right-hand panel), Barro et al. (2013) (middle left-hand panel), van Dokkum et al. (2015) (middle right-hand panel) van der Wel et al. (2014) (bottom left-hand panel), and Graham et al. (2015) (bottom right-hand panel). Additionally, the 13 E+ES class galaxies are highlighted in squares (■), where E galaxies are in green and ES galaxies are in yellow. The outliers with galaxy colour ($g - i$) > 1.5 are marked with black star signs (⋆, see Section 3.5). In our sample, there are 55 (53 per cent), 10 (9.7 per cent), 60 (58.3 per cent), 9 (8.7 per cent), and 7 (6.7 per cent) compact massive spheroids according to Barro et al. (2013)'s, van der Wel et al. (2014)'s, Damjanov et al. (2015a)'s, van Dokkum et al. (2015)'s, and Graham et al. (2015)'s compactness criteria, respectively.

(i) In the middle left-hand panel of Fig. 15, we applied the Barro et al. (2013) selection boundary (green) with mass and circularized size limits:

$$M_*/\mathrm{M}_\odot > 10^{10}$$
$$\log_{10}(R_\mathrm{e}/\mathrm{kpc}) < \left[\log_{10}(M_*/\mathrm{M}_\odot) - 10.3\right]/1.5. \quad (11)$$

The compact massive quiescent galaxies in the CANDELs survey (Grogin et al. 2011; Koekemoer et al. 2011) within this boundary roughly follow the Newman et al. (2012) size–mass relation. The slope of the selection boundary is motivated by the apparent trend of the quiescent galaxies (with specific star-formation rate $\log_{10}(sSFR_{\mathrm{UV+IR}}) > -0.5\,[\mathrm{Gyr}^{-1}]$) at $z > 1.5$.

(ii) In the bottom left-hand panel, the van der Wel et al. (2014) boundary (blue) was applied:

$$M_*/\mathrm{M}_\odot > 5 \times 10^{10}$$
$$R_{\mathrm{e,major}}/\mathrm{kpc} < \left(M_*/10^{11}\,\mathrm{M}_\odot\right)^{0.75} \times 2.5. \quad (12)$$

Note, that unlike most studies, van der Wel et al. (2014) selected their compact sample by the major axis effective radius $R_{\mathrm{e,\,major}}$ instead of in the equivalent axis $R_{\mathrm{e,\,eq}}$, where the two quantities follow the relation $R_{\mathrm{e,eq}} \equiv R_{\mathrm{e,major}}\sqrt{b/a}$, in which b/a is the semiminor to semimajor axes ratio of a galaxy's apparent elliptical shape. Therefore, the size–mass plot in the lower left-hand panel of Fig. 4.3 is plotted in major axis instead.

(iii) In the top right-hand panel, the sample is divided by the Damjanov et al. (2014) compactness criteria (red):

$$M_*/\mathrm{M}_\odot > 10^{10}$$
$$\log_{10}(R_\mathrm{e}/\mathrm{kpc}) < 0.568\log_{10}(M_*/\mathrm{M}_\odot) - 5.74. \quad (13)$$

Unlike the high-z studies, Damjanov et al. (2014) applied this selection criteria on a sample of intermediate redshift galaxies from the COSMOS field at $0.2 < z < 0.8$. While having discussed the different choice in the mass limit, we set it to the lowest limit for easier comparison with Barro et al. (2013).

(iv) In the middle right-hand panel, we select for the van Dokkum et al. (2015) boundary (yellow):

$$M_*/\mathrm{M}_\odot > 4 \times 10^{10}$$
$$\log_{10}(R_\mathrm{e}/\mathrm{kpc}) < \log_{10}(M_*/\mathrm{M}_\odot) - 10.7. \quad (14)$$

This selection criteria are constructed based on the argument that the Barro et al. (2013) boundary is not restrictive enough because it will also include 60 per cent of the star-forming galaxies, which have a factor of two bigger effective radii than the quiescent galaxies. It could enhance the 'progenitor bias', where the quenching of star-forming compact galaxies may inflate the number density of the passively evolving quiescent galaxies. It does not, however, concern our sample because the stellar population of local bulges has exist for a long time (MacArthur, González & Courteau 2009). It is unlikely the quenching process between $0 < z < 1.0$ to produce such system.

(v) In the bottom right-hand panel, we select the compact spheroids via the Graham et al. (2015) selection conditions (grey):

$$M_*/\mathrm{M}_\odot > 7 \times 10^{10}$$
$$R_{\mathrm{e,major}}/\mathrm{kpc} < 2.0. \quad (15)$$

Building on Graham (2013), Graham et al. (2015) furthered the proof of concept for this study as it supplied generic selection criteria on small, but massive bulges in the local Universe from different studies (Seigar & James 1998; Graham 2001; Möllenhoff & Heidt 2001; Balcells, Graham & Peletier 2007; Laurikainen et al. 2010; van den Bosch et al. 2012; Dullo & Graham 2013; Savorgnan & Graham 2016a). They found 21 small, but massive spheroids within 90 Mpc and gave an initial (lower) estimate of the volume number density $n \sim 6.9 \times 10^{-6}\,\mathrm{Mpc}^{-3}$ (or per unit dex stellar mass, it is $3.5 \times 10^{-5}\,\mathrm{Mpc}^{-3}\,\mathrm{dex}^{-1}$) as a lower limit for such systems.

While we have focused on galaxies more massive than $10^{11}\,\mathrm{M}_\odot$, given that the presence of a disc results in a bulge-to-total ratio less than 1, we have uncovered some spheroids less massive than $10^{11}\,\mathrm{M}_\odot$. Although our spheroid sample is incomplete below this mass, we are able to obtain lower limits to the actual number density of compact spheroids defined by a range of selection criteria in the literature which have encompassed masses down to 1, 4, 5, and $7 \times 10^{10}\,\mathrm{M}_\odot$. It must, therefore, be kept in mind that the number densities, from our three bins, shown in Fig. 15 are lower limits.

The majority of the spheroids (66/103) lie within the size–mass range $0.4\,\mathrm{kpc} < R_\mathrm{e} < 6.0\,\mathrm{kpc}$ and $1.0 \times 10^{10} < M_*/\mathrm{M}_\odot$ (RC15) $< 2.5 \times 10^{11}$. The lower bound simply reflects the mass boundary of our host galaxy sample and reveals that some galaxies have B/T ratios less than 0.1. The scatter along either the size or mass axis is rather small in this region. With (geometric mean)-axis half-light radii less than $\approx$1 kpc and stellar masses $M_{*,\,\mathrm{sph}} < 2 \times 10^{10}\,\mathrm{M}_\odot$ (RC15), the scatter is much more prominent. This variation of scatter is less apparent when using the major-axis size, as shown in the lower left-hand panel of Fig. 15. We include this because van der Wel et al. (2014) used the major-axis galaxy sizes for their investigation.

Considerable effort has been made searching for the ultracompact massive galaxies (UCMGs) in the local Universe, defined by as those with $M_{*,\mathrm{gal}}/\mathrm{M}_\odot > 8 \times 10^{10}$ and $R_\mathrm{e} < 1.5$ kpc (Trujillo et al. 2009; Ferré-Mateu et al. 2017; Tortora et al. 2018, 2020; Scognamiglio et al. 2020). These objects are extremely rare compared to the regular red nuggets, with the number density of $n_{\mathrm{UCMG}} \sim 1$–9×10^{-6} Mpc^{-3} at $z < 0.5$ (Tortora et al. 2018, 2020). In our sample, there are two spheroids that satisfy the UGMG definition, giving a lower limit to the number density of ultracompact massive spheroids of $n_{\mathrm{c,Sph}} \sim 4.2 \times 10^{-6}\,\mathrm{Mpc}^{-3}$.

We provide an assortment of information in Tables D1–D3 regarding our spheroid sample. The parameters of the Sérsic functions are listed in Columns (4)–(6). Column (7) gives the spheroid apparent magnitudes as measured by `Profiler`. Column (8) lists the absolute magnitudes of the spheroids, based on the distances shown in Appendix A. The magnitudes are corrected for galactic extinction from Schlegel, Finkbeiner & Davis (1997). Columns (9)–(12) tabulate the spheroid stellar masses, obtained using each of the four MLCRs (Equation Array 3).

5 COSMIC EVOLUTION OF COMPACT MASSIVE SPHEROIDS

In this section, we compare our local spheroids with the red nuggets in low-to-intermediate-z (Section 5.3) and high-z (Section 5.2) from the literature, as well as the embedded local bulges obtained by other multidecomposition works (Section 5.1). Subsequently, we are able to plot out the potential evolution of compact massive spheroids across cosmic time. The effect of adopting a different M_*/L ratio is explored in Section 5.4.

5.1 Low redshifts ($z < 0.03$)

We have compared our local spheroids with the bulges from other studies of $z \approx 0$ galaxies. We have a preference for decompositions with a similar degree of detail. Relevant studies of the galaxy size evolution (e.g. Trujillo et al. 2006, 2007; Taylor et al. 2010; Newman et al. 2012; McLure et al. 2013; Damjanov et al. 2014; Fang et al. 2015) have measured the effective radii and stellar

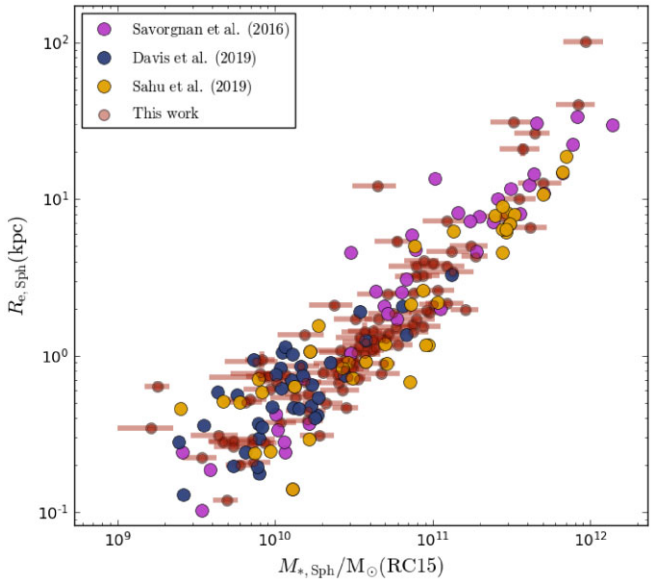

Figure 16. A comparison of our spheroids' stellar masses ($M_{*,\,Sph}/M_\odot$(RC15)) and circularized effective radius ($R_{e,\,Sph}$, transparent red points) with those from Savorgnan & Graham (2016a) (purple points), Davis et al. (2019) (blue points), and Sahu et al. (2019) (orange points). The spheroids stellar masses from Savorgnan & Graham (2016a), Davis et al. (2019), and Sahu et al. (2019) are based on 3.6 μm. Both bulges and elliptical galaxies are included.

masses of local early-type galaxies, but not their bulges nor the bulges of any massive early-type spiral galaxies. This may have prevented them from establishing the evolutionary pathway taken by the high-z compact massive galaxies. The underlying assumption of those works was the preservation of the morphological types throughout their evolutionary history. Due to our different approach, a comparison with the galaxy sizes and masses from those studies would be of limited value to test our theory. We can, however, explore if our bulge sizes and masses agree with those from multicomponent decompositions of local galaxies.

Several studies of supermassive black hole scaling relations (e.g. Savorgnan & Graham 2016a; Davis et al. 2019; Sahu et al. 2019) have performed a similar style of careful galaxy analysis using IRAC 3.6 μm images of galaxies in the local Universe. Fig. 16 shows the size–mass distribution of our spheroids (red points) and the local bulges and giant elliptical galaxies from these studies.

Savorgnan & Graham (2016a) obtained their surface brightness profiles via `IRAF` task `ellipse` from 66 early-type host galaxies and measured the sizes and masses by using a bespoke fitting code. Davis et al. (2019) and Sahu et al. (2019) extracted their surface brightness profiles with `ISOFIT` and performed decompositions via `Profiler`. The Davis et al. (2019) spheroids are from 44 spiral host galaxies, while the Sahu et al. (2019) spheroids are from 40 early-type galaxies. These studies examine each galaxy on a case-by-case basis and assign physical components (e.g. bars and ansae rather than random Sérsic components) when modelling each surface brightness profile (see the appendices of the respective papers for detailed discussions on each galaxy).

Despite the decompositions being conducted by different personnel, the resulting distribution of bulge sizes and masses appear remarkably consistent. The high-mass end of the near-linear distribution in Fig. 16 resembles the bright arm of the spheroid distribution seen in Graham (2013, see fig. 1). Here, we mainly want to illustrate the consistency across the different studies; that is, there is no unusual offset in our sample, nor sign of dichotomy. The implications of this bulge/spheroid size–mass diagram shall be explored in future work.

In passing, we briefly note that we may be seeing evidence for a steepening of the relation at high masses. This is expected for merger-built elliptical galaxies for which the mass scales with $\sigma^2 R_{eq}/G$ yet σ barely increases over the value in the progenitor galaxies (e.g. Volonteri & Ciotti 2013). Also at play is the influence of the intracluster light (ICL) surrounding BCGs, and we may have overestimated the galaxy sizes at the top-end. Driver et al. (2007b) produced a B-band bulge luminosity function from two-component Sérsic+exponential fits (Allen et al. 2006) at $0.013 < z < 0.18$. While that work contained no dust corrections, fig. 2 from that work reveals, for their brightest bulges, a declining number density at $\mathfrak{M}_B = -20$ to -20.75 mag (AB magnitude system) – where S0 galaxies likely dominate and there is no substantial dust – of around 3×10^{-4} to 0.5×10^{-4} Mpc^{-3} dex^{-1}. For $\mathfrak{M}_{B,\odot} = +5.44$ mag, and $M_*/L = 8$, this roughly corresponds to 1.2–2.4×10^{11} M$_\odot$. Their number density, therefore, overlaps well with our result at a similar mass in Fig. 14. We do, however, find the same number density at 5×10^{11} M$_\odot$ in our data, while Driver et al. (2007b) has no bulges at these higher masses.

Our number density drops to $\sim 0.2 \times 10^{-4}$ Mpc^{-3} dex^{-1} at $M_{*,Sph} \sim 10^{12}$ M$_\odot$. The absence of the highest mass bulges in Driver et al. (2007b) may be due to the 'logic filter' employed by Allen et al. (2006) for identifying the more secure bulge + disc decompositions. It meant that the ES galaxies, and importantly perhaps some misfit S0 galaxies, remained in the single-component E galaxy bin at these highest masses. Resolving this is, however, beyond the scope of the current investigation. However, it is important to note that in this mass range, there are only two spheroids in our sample. It reflects the reality that spheroids with mass $M_{*,gal}/M_\odot \sim 10^{12}$ are rare indeed.

5.2 High redshifts ($1 < z < 3$)

The different selection criteria for compact massive systems have been used to illustrate the migration pattern of galaxy distributions, over cosmic time, in the size–mass diagram. As shown by Barro et al. (2013), van der Wel et al. (2014), and van Dokkum et al. (2015), with decreasing redshift, less and less galaxies occupy the 'compactness' selection boundaries. Damjanov et al. (2015a) demonstrated that while the actual number densities are different – depending on the selection criteria for compact massive systems – the overall trend/reduction with time remains.

We have compared the number density of our local, compact massive spheroids with that of compact massive galaxies in the intermediate and high redshift Universe. Fig. 17 shows the evolutionary trend of number density for compact systems across time, based on four different compactness criteria, from top to bottom: equations (11) (top), (12) (upper middle), (14) (lower middle), and (13) (bottom). To represent the high-z ($1.0 < z < 3.3$) red nuggets, we have included the number density trends from three works: Barro et al. (2013) (green diamonds ✦ in the top panel), van der Wel et al. (2014) (blue diamonds ✦ in the upper middle panel), and van Dokkum et al. (2015) (orange diamonds ✦ in the lower middle panel).

For intermediate redshifts ($0.2 < z < 1.0$), we included the data from Damjanov et al. (2015a). They applied several different size–mass sample selection criteria to their data. Their evolutionary trend based on the Barro et al. (2013) size–mass selection criteria is plotted in the top panel (see fig. 9 in Damjanov et al. 2015a), and that based on the van der Wel et al. (2014) selection criteria is shown in the upper middle panel (see fig. 12 in Damjanov et al. 2015a), while that based on the Damjanov et al. (2014) selection criteria is shown in the bottom panel (from fig. 11 in Damjanov et al. 2015a). These trends are marked with red diamonds (✦) in Fig. 17. In addition,

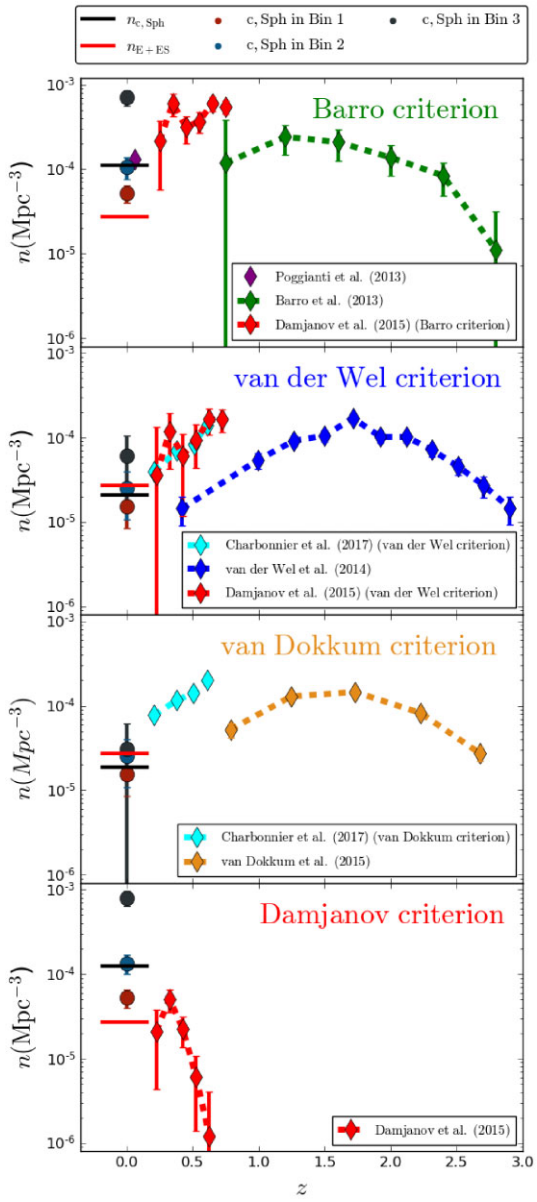

Figure 17. The number density of compact massive systems across cosmic time, based on four different size–mass selection criteria or defining boundaries. It shows the evolution of compact objects from the literature, marked in diamonds (✦) under the Barro et al. (2013) boundary (top panel, in green, from their fig. 5), the van der Wel et al. (2014) boundary (upper middle panel, in blue, from their fig. 13), the van Dokkum et al. (2015) boundary (lower middle panel, in orange, from their fig. 19), and the Damjanov et al. (2014) boundary (bottom panel, in red, from Damjanov et al. 2015a, fig. 11). The red, blue, and black circles (●), at $z \sim 0$, represent the number densities from Bins 1, 2, and 3, correspondingly. The error bars of our compact massive spheroids are assumed to be Poissonian. The horizontal black line, labelled '$n_{c,\,Sph}$', is the lower limit of the number densities across the three bins, and the red line, labelled 'n_{E+ES}', is the lower limit for the true elliptical galaxies and ellicular galaxies in the three bins (given by equation 16). In addition, the Damjanov et al. (2015a) compact sample (lower panel) is additionally shown by the red diamonds (✦) in the top and upper middle panels, while the Poggianti et al. (2013b) compact sample is marked with a purple diamond (✦) in the top panel. The number density of the compact massive galaxies from Charbonnier et al. (2017), defined using the van der Wel et al. (2014) and van Dokkum et al. (2015) criteria are depicted by the cyan diamonds (✦) in the upper middle and lower middle panels, respectively.

the number density provided by Poggianti et al. (2013b) is included, marked by the purple diamond (✦) in the top panel. The sample selection criteria from Barro et al. (2013) was used by Poggianti et al. (2013b). Because the other three criteria were not implemented by Poggianti et al. (2013b), we do not include their data in the other panels. Charbonnier et al. (2017) selects for compact massive galaxies in the SDSS Stripe 82 (CS82, Moraes et al. 2014) survey at $0.2 < z < 0.6$. Their number density trends, based on van der Wel et al. (2014) and van Dokkum et al. (2015) criteria, are presented as cyan diamonds (✦) in the upper middle and lower middle panels of Fig. 17, respectively.

In Fig. 17, the three colour-coded circles (●) at $z = 0$ are our lower limits on the number density of compact massive spheroids, as obtained using the different selection criteria applied to our three bins. In all the panels, Bin 3 tends to have the highest number density, and Bin 1 the lowest. This is a result of the bin design. As Bin 3 is complete down to the lowest host galaxy stellar mass ($M_*/\mathrm{M}_\odot$ (IP13) $\sim 1 \times 10^{11}$) compared to Bin 2 ($M_*/\mathrm{M}_\odot$ (IP13) $\sim 2 \times 10^{11}$) and Bin 1 ($M_*/\mathrm{M}_\odot$ (IP13) $\sim 5 \times 10^{11}$), we are able to capture more compact massive spheroids in Bin 3. Note that in the lower middle panel (van Dokkum et al. (2015) criterion) of Fig. 17, the number densities of all three bins are closer than the other panels. This is because van Dokkum et al. (2015)'s criterion selects only for high-mass spheroids and red nuggets with $M_*/\mathrm{M}_\odot$ (RC15) $\gtrsim 4 \times 10^{10}$. If relatively low-mass ($1 \times 10^{10} \lesssim M_*/\mathrm{M}_\odot$ (RC15) $\lesssim 4 \times 10^{10}$) systems are also included, such as when using the selection criteria from Barro et al. (2013) and Damjanov et al. (2015a), an abundance of low-mass compact massive spheroids can be found in Bin 3. These 'red pebbles' are more likely to live inside of galaxies within the mass range of $6.7 \times 10^{10} < M_{*,\mathrm{gal}}/\mathrm{M}_\odot$ (RC15) $< 1.3 \times 10^{11}$. As a result, there is roughly a factor of 10 more compact massive spheroids in Bin 3 in the upper- and lower middle panels than the top and bottom panels in Fig. 17.

For the sake of discussion, we categorise the number density of our spheroids into $n_{c,\,Sph}$ and n_{E+ES}. In Fig. 17, across all four panels, the black horizontal line ('$n_{c,\,Sph}$') depicts the total number of compact spheroids from all three bins divided by the volume $V = 4.76 \times 10^5\,\mathrm{Mpc}^3$ (our sample volume encompassed within 110 Mpc), while the red horizontal line (labelled 'n_{E+ES}') is the total number of the 'true ellipticals' (E) and elliculars (ES) divided by this volume V:

$$n_{c,Sph} = (N_{c,Sph,Bin1} + N_{c,Sph,Bin2} + N_{c,Sph,Bin3})/V \quad (16a)$$

$$n_{E+ES} = (N_{E+ES,Bin1} + N_{E+ES,Bin2} + N_{E+ES,Bin3})/V. \quad (16b)$$

These two values depict lower limits to the number densities. For $n_{c,\,Sph}$, it is the lower limit of compact massive spheroids based on a volume-limited sample of galaxies with $M_* > 6.7 \times 10^{10}\,\mathrm{M}_\odot$ (RC15) and within a distance of 110 Mpc. The value for n_{E+ES} represents the lower limit to the true number density of elliptical (E) and ellicular (ES) galaxies that can be found above $M_*/\mathrm{M}_\odot$ (RC15) $\sim 6.7 \times 10^{10}$. Note that $n_{E+ES,\,Bin3}$ is likely to be close to the true value because true elliptical galaxies tend to be massive; that is, ETGs less massive than $6.7 \times 10^{10}\,\mathrm{M}_\odot$ tend to be S0 galaxies[21] (Emsellem et al. 2011; Krajnović et al. 2013a; Cappellari et al. 2013; Cappellari 2016). For Bins 1 and 2, we may have missed some E galaxies due to the higher stellar-mass selection criteria required to keep the number of galaxies requiring careful multicomponent decomposition at a manageable level.

[21] Our E+ES galaxy with the lowest stellar mass is roughly $\sim 0.7 \times 10^{11}\mathrm{M}_\odot$

From Fig. 17, it is apparent that the definition of 'compact and massive' makes a difference to the reported number density (see also, Charbonnier et al. 2017). For the less restrictive size–mass sample selection criteria (Barro et al. 2013; Damjanov et al. 2014), the number density of compact massive spheroids is consistently higher than the number density of elliptical galaxies ($n_{\rm c,\,Sph} > n_{\rm E+ES}$), while applying the more restrictive criteria (van der Wel et al. 2014; van Dokkum et al. 2015), the two numbers are comparable ($n_{\rm c,\,sph} \simeq n_{\rm E+ES}$). This is, in part, because $n_{\rm E+ES}$ does not depend on any size or mass selection criteria, unlike $n_{\rm c,\,sph}$ (see Fig. 15).

The discrepancy between the restrictive and the less-restrictive size–mass sample selection criteria in use in the literature is informative. It means that among the local compact systems, the elliptical galaxies and high-mass spheroids ($>$(4–7)$\times$ $10^{10}\,{\rm M}_{\odot}$), formed via an E-to-E process or disc-cloaking, respectively, may have occurred with similar frequency. The disc-cloaking process is likely the dominant mechanism in shaping galaxy evolution within the stellar mass range $1 \times 10^{10} < M_*/{\rm M}_{\odot}$ (RC15) $<4 \times 10^{10}$.

5.3 Low-to-intermediate redshifts ($0.03 < z < 1$)

As a bridge between the local spheroids and the high-z galaxies, the information from intermediate redshifts provides insight into the transitioning process. In Fig. 17, we compare our results with Damjanov et al. (2015a). They studied the number density of quiescent, compact massive galaxies at $0.2 < z < 0.8$ from the COSMOS field (Leauthaud et al. 2007). While they acknowledged that most of their sample exhibited a Bulge + Disc structure, they concluded that the single Sérsic profile captures the size of the spheroids well in this redshift range, with perhaps just a slight overestimation in size.

This sample's number density shows consistency with the Barro et al. (2013) and van der Wel et al. (2014) high-z sample's peak abundance (see the top and upper middle panels in Fig. 17). In the upper panel of Fig. 17, the data from Damjanov et al. (2015a) straddles the region between our Bin 2 and Bin 3 number densities. It is also more abundant in comparison to the red nuggets' peaks number densities at $z = 1.2$, and $z = 1.7$. The lower panel shows the trend in number density, with redshift, using the size–mass selection criteria from Damjanov et al. (2014). Unfortunately with this selection, the complete set of data is not available, and Damjanov et al. (2015a) only show a partial result that they selected from the COSMOS quiescent galaxies classified as point sources in the photometric SDSS data base. Their fig. 11 depicts only a lower limit to the number density at intermediate-redshift. Nonetheless, our number of compact spheroids is vastly more numerous than the trend shown in the bottom panel. The matching number densities with the high- z data led them to conclude that the number of compact objects does not depend strongly on redshift.

Both Valentinuzzi et al. (2010) and Poggianti et al. (2013b) have argued for a constant compact quiescent galaxy number density (see also Saracco et al. 2010). Valentinuzzi et al. (2010) found a substantial number of compact quiescent galaxies in the WIde-field Nearby Galaxy-cluster Survey (WINGS; Fasano et al. 2006) at $0.04 < z < 0.07$. They reported a minimum number density of $1.3 \times 10^{-5}\,{\rm Mpc}^{-3}$ and possibly up to $1.3 \times 10^{-2}\,{\rm Mpc}^{-3}$ in cluster environments. Crucially, the majority (67 per cent) of their compact galaxies are S0. In the Padova Millennium Galaxy and Group Catalogue (PM2GC; Calvi, Poggianti & Vulcani 2011), Poggianti et al. (2013b) found $n \sim 4.23 \times 10^{-4}\,h^3\,{\rm Mpc}^{-3}$ at $0.03 < z < 0.11$. We have plotted their number density in the top panel of Fig. 17 (marked as ✦) for comparison. Both studies acknowledge that more compact quiescent galaxies were found in dense cluster environments (see also, Tortora et al. 2020). Indeed, Damjanov et al. (2015b) highlighted the environmental dependency of compact galaxies in the COSMOS field. At intermediate-z, the compact quiescent galaxies align with the high-density regions (see their fig. 8). Although, it is important to note that this might simply be a result of more massive quiescent galaxies (of all sizes) living in cluster environments compared to the field (Tortora et al. 2020).

The depth and field-of-view in our parent sample selection (see Section 2, and equation 1) is wide enough to cover both clusters and fields. It captures the small Virgo Cluster overdensity at a distance of 17 Mpc and a slight void at 40–60 Mpc. We explore the influence of the Virgo Cluster has on our analysis, later in Section 6.4.3.

5.4 Variation arising from different MLCRs

One of the uncertainties on our, and everyone's, spheroid number density comes from the adopted MLCRs and thus the stellar mass measurement. For Figs 14 to 17, we presented the result using the RC15 MLCR. Here, we will explore the consequences of applying different MLCRs. Fig. 18 shows the number density of the local compact spheroids (marked with a •) and the ellicular and elliptical galaxies (marked with a ■) based on the four different MLCRs presented in Section 2.3 and the four different selection criteria presented in Section 4.3. We have also highlighted the maximum number density of red nuggets from various works with colour-coded dashed lines.

Using the size–mass selection criteria from Barro et al. (2013) and Damjanov et al. (2015a), the number densities of compact massive spheroids are higher than elliptical+ellicular (E+ES) galaxies, for all four MLCRs (see the upper green panel and the lower red panel in Fig. 18). Applying the more restrictive size–mass selection criteria from van der Wel et al. (2014) and van Dokkum et al. (2015) reduces the number of compact massive spheroids included in the sample selection boundaries (see the upper middle panel shaded blue and the lower middle panel shaded yellow), lowering it to roughly less than or equal to the fixed number (density) of E+ES galaxies among our sample of 103 galaxies. When using the T11 stellar masses, no compact massive spheroid was found with the restrictive size–mass selection criteria. However, when using the higher IP13 stellar masses, the observed number densities of compact spheroids increased to greater than the number of E+ES galaxies, in all criteria.

The comparison showcases how the number density varies under the different stellar mass measurement and compactness selection criteria. Importantly, the MLCRs from T11 and RC15 assume the same IMF and SPS as used by those studying the high-z red nuggets. The result from the less restrictive boundaries in the size–mass plane is consistent when using these two MLCRs. With the more restrictive boundaries in the size–mass plane, and since no compact system was found using the MLCR from T11, we can conclude that the number density of local 'compact massive' spheroids is subject to the particular M_*/L ratio employed. Resolving this, beyond having reported its impact, is clearly outside the scope of the current investigation.

Our results are, however, robust when using the more inclusive size–mass selection criteria from Barro et al. (2013) and Damjanov et al. (2014). For all stellar mass estimates, we found a consistent trend of $n_{\rm c,\,Sph} > n_{\rm E+ES}$. Considering that $n_{\rm c,\,Sph}$ is just a lower limit for the local compact massive spheroids, while $n_{\rm E+ES}$ is close to the true value, our result calls for a reevaluation of the nature of the size-evolution experienced by red nuggets. At a minimum, disc growth has to play an essential role in shaping the high-z galaxies in the lower mass range ($1 \times 10^{10} < M_*/{\rm M}_{\odot}$ (RC15) $<4 \times 10^{10}$).

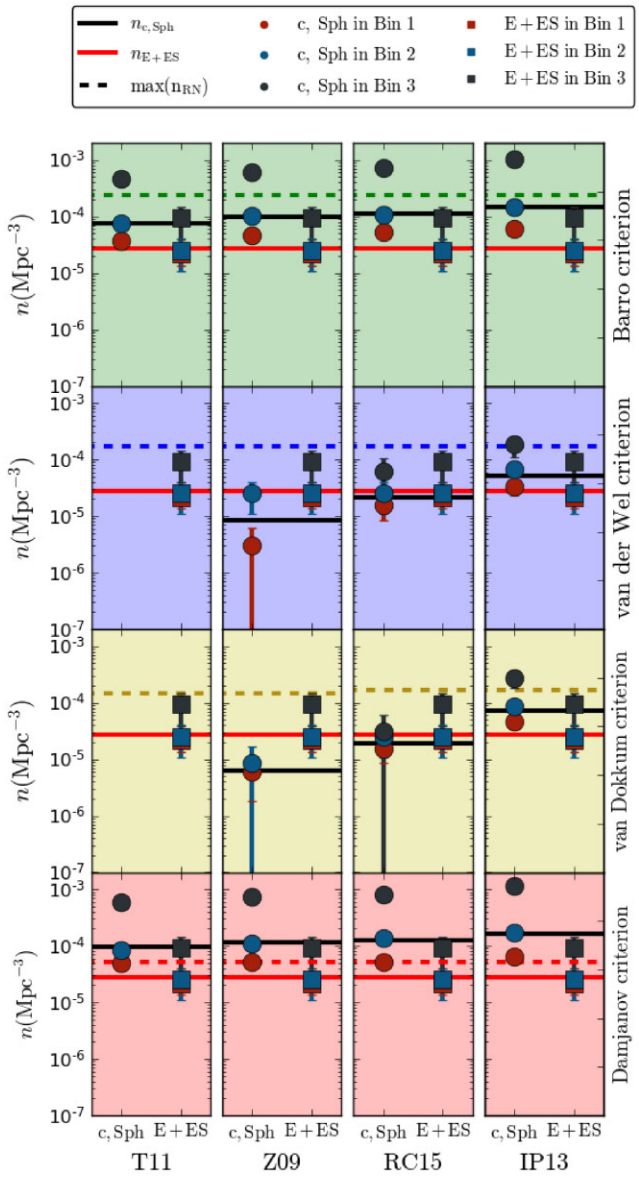

Figure 18. The number densities of local compact spheroids (•) and ellipticals + elliculars (■), using four different MLCRs, based on four size–mass selection criteria. The selection criteria applied from top to bottom are given by equations (11), (12), (14) and (13), respectively. From left to right, the MLCRs are from T11, Z09, RC15, and IP13, respectively. The red, blue, and black colours represent the samples from Bins 1, 2, and 3, respectively. The black and red horizontal lines are $n_{c,\,Sph}$ and n_{E+ES}, as depicted in Fig. 17. Here, the number density of 'E+ES' includes 11 true E galaxies and 2 ES galaxies. None of these E and ES galaxies are not 'compact massive', that is, these 13 galaxies did not satisfy any of the four 'compact massive' selection criteria. The colour-coded dashed lines are the maximum number density of the red nuggets (labelled 'max(n_{RN})') from the respective high-z publications which defined the size–mass selection criteria.

6 DISCUSSION

We have established that only ∼11 per cent of the galaxies in our sample of massive galaxies are true elliptical galaxies; the majority are multicomponent systems with bulges, discs, bars, and other lesser components. Our trend between the bulge, aka spheroid size, and mass agrees well with data from comparable, multicomponent decomposition analyses of nearby galaxies. That is, we do not detect any systematic bias in our measurements. We derive a lower limit to the number density per unit volume of (hidden) compact massive spheroids using four different size/mass selection criteria, giving $n_{c,\,Sph} \sim (0.17–1.20)\times10^{-4}$ Mpc^{-3}. We additionally examined how $n_{c,\,Sph}$ changes when adopting the four different MLCRs. We found that if only high-mass spheroids ($M_*/M_\odot$ (RC15) $>4 \times 10^{10}$) are considered, $n_{c,\,Sph}$ can be either lower, comparable or higher than n_{E+ES}. The uncertainty in stellar mass makes estimating the correct number density challenging. In the case of low-mass spheroids ($1 \times 10^{10} < M_*/M_\odot$ (RC15) $<4 \times 10^{10}$), such an issue does not exist.

In what follows, we further compare local compact massive spheroids with distant red nuggets, and we address proposed size-evolution hypotheses based on the results from our findings.

6.1 Differing evolutionary views, definitions, and assumptions

6.1.1 Alternative evolutionary processes

Here, we provide a brief overview of different conjectures regarding the size-evolution pathway taken by high-z compact massive quiescent galaxies.

(i) *Compact massive quiescent galaxies experience rapid size evolution, an E-to-E scenario*

Trujillo et al. (2007) plotted the half-light galaxy radii of local, luminous galaxies with Sérsic indices $n > 2.5$. These galaxies are a factor of four larger than the compact spheroidal-like systems at $z \sim 1.5$. From this, they concluded that the $z \sim 1.5$ compact massive galaxies evolved through dry mergers with themselves, i.e. equal-mass major mergers without star formation. van Dokkum et al. (2008) reported a typical growth in galaxy half-light radii by a factor of 5–6 since $z \sim 2.3$. They found that only 10 per cent of the massive spheroid-like galaxies at $z \sim 2.3$ had galaxy sizes equal to that of elliptical galaxies of comparable mass at $z \sim 0$. They, therefore, argued against 'monolithic collapse' as the formation channel because they found only 10 per cent are fully assembled by $z \sim 2.3$. They noted an array of processes to possibly explain the size growth, including dry mergers, satellite accretion, expansion after mass loss from stellar winds, and the arrival of new, larger galaxies since $z \sim 2.3$ on to the red sequence.

The notion of major mergers driving size evolution has been heavily challenged. The observed number of major mergers (1:1 to 1:4 mass ratios) is too low to explain the change in number density of massive ($\log_{10}(M_*/M_\odot) \geq 11.1$) galaxies (Man, Zirm & Toft 2016). Taylor et al. (2010) found no galaxies in the SDSS DR7 with comparable sizes to the van Dokkum et al. (2008) and Damjanov et al. (2009) red nuggets at higher redshifts. They also argued against *stochastic* major mergers as the critical driving force for the size evolution in early-type galaxies because it will result in some galaxies (those which experienced many mergers) having masses larger than observed in the local Universe. Carrasco, Conselice & Trujillo (2010), who studied eight massive galaxies at $1 < z < 2$ from the POWIR survey (Conselice et al. 2007), reported extreme compactness within $R < 2$ kpc (higher than the stellar densities of local galaxies). With similar reasoning as Taylor et al. (2010), they advocated that minor mergers and accretion are more likely the cause of the size growth.

While some kind of E-to-E scenario is widely accepted in the community (e.g. Buitrago et al. 2008; Bezanson et al. 2009; Hopkins et al. 2009; Szomoru et al. 2011; Newman et al. 2012), the mechanism which supports a dramatic E-to-E size growth remains a subject of debate. Fan et al. (2008) had proposed that through mass loss

(stellar winds, AGN jets), galaxies experience adiabatic expansion as the new gravitational equilibrium relaxes. However, adiabatic expansion has been called into question by numerical simulations, as Ragone-Figueroa & Granato (2011) found galaxies 'puffing-up' due to stellar winds occurs when the stellar population is younger than the formation of the red nuggets (by 0.5 Gyr). Hopkins et al. (2009) and Bezanson et al. (2009) advocated that, through minor mergers and accretion, red nuggets may build up a low-density three-dimensional envelope which hides the compact galaxies as the core of a larger *elliptical* galaxy (see also Hopkins et al. 2010; Szomoru et al. 2011; López-Sanjuan et al. 2012; Oogi & Habe 2013).

(ii) *Compact massive quiescent galaxies experience only a mild, or no, evolution and now reside in local galaxy clusters: an E-to-E/S0 scenario.*

(Galaxy cluster)-focused studies at intermediate-z have challenged the universality of the significant size-growth scenario. Valentinuzzi et al. (2010) and Saracco et al. (2010) report on the abundance of 'compact' galaxies in cluster environments and postulate that red nuggets live in dense environments nowadays. Similarly, Poggianti et al. (2013b) found that the fraction of local compact massive galaxies are three times higher in clusters than in the field, arguing for the scenario of mild evolution (by a factor of ∼1.6 in size) for high-z red nuggets. Damjanov et al. (2015b) echo the same point as they subsequently found compact massive quiescent galaxies at $0.1 < z < 0.4$ in the COSMOS field (Scoville et al. 2007) resided in denser environments than other quiescent galaxies. Carollo et al. (2013) argued that the addition of more large newly quenched early-type galaxies, as time progresses, is responsible for the apparent size evolution (a.k.a., the 'progenitor bias', van Dokkum & Franx 1996; Saglia et al. 2010). In this picture, the size growth of quiescent galaxies since $z \sim 2$ is of secondary importance.

(iii) *Compact massive quiescent galaxies experience size evolution via disc growth: a disc-cloaking (E-to-S0/S) scenario*

Graham (2013) and Graham et al. (2015) expanded the possible evolutionary channels, where instead of only considering elliptical (E) galaxies as the end product of red nugget evolution, lenticular (S0) and early-type spiral (Sa) galaxies may arise by cloaking the compact spheroid with a large-scale disc built through minor mergers and gas accretion. Upon entering a cluster of galaxies with a hot X-ray gas halo, any future disc growth via gas accretion and star formation would naturally be curtailed. The hypothesis of disc-cloaking was supported by a reported lower-limit to the number density of $n \sim 6.9 \times 10^{-6}\,\mathrm{Mpc}^{-3}$, based on 21 local compact massive spheroids within 90 Mpc (Graham et al. 2015). It was a lower-limit because the volume was not sampled completely; the 21 systems simply represented spheroids that had been reported in the literature as having small sizes and high masses and were known to the authors. Their finding was further supported by de la Rosa et al. (2016) using the automatic Bulge + Disc decompositions of local galaxies imaged by SDSS (Mendel et al. 2014). From a sample of SDSS DR7 galaxies and a survey area of $8,032\,\mathrm{deg}^2$ at $0.025 < z < 0.15$, they found a number density of local compact bulges ($n \sim 0.28$–$3.12 \times 10^{-4}\,\mathrm{Mpc}^{-3}$) comparable with the number density of the distant red nuggets across multiple size–mass sample-selection criteria (Barro et al. 2013; van der Wel et al. 2014; van Dokkum et al. 2015). Because galaxies can have (truncated) non-exponential discs and more than two components, such as bars and rings, etc., automated Bulge + Disc decompositions often fail to provide a reliable measurement of the bulge size and luminosity, which is why we undertook our careful investigation.

6.1.2 *Differing selection criteria and assumptions*

The criteria of selecting for the parent sample, measurement of the galaxies' properties, and the definition of compactness, vary from one study to another. It will be a monumental task to homogenize all the data presented in the literature. Instead, we provide a brief description of various approaches and assumptions commonly made (see Table 5), and we highlight a few potential causes of discrepancy.

Parent sample: The majority of studies select their parent galaxy set based on the galaxies' stellar masses, redshifts, and star formation (or its proxies, e.g. colour-colour selection). Sometimes the sample is further restricted by morphology or brightness concentration (Sérsic index). Column (2) in Table 5 summaries such unique conditions for several studies. Trujillo et al. (2007) divided their sample of luminous galaxies into 'spheroidal' (Sérsic index $n > 2.5$) and 'disc-like' (Sérsic index $n < 2.5$) to illustrate the stronger size evolution in spheroids, and the lack thereof in disc galaxies. The Bezanson et al. (2009) local sample is morphology-dependent, using the apparent 'E' galaxies from Tal et al. (2009). Some studies did not construct the parent sample based on star formation (Trujillo et al. 2007, 2009; Taylor et al. 2010), where both quiescent and star-forming galaxies are considered. The sample from Carollo et al. (2013) is based on the ZEST+ morphology classification (an upgraded version from Scarlata et al. 2007), from which they select both massive early-type ('E/S0') and late-type ('Sa–cd') galaxies. Studies that have a parent sample inclusive of all morphologies would not be biased by an E-to-E scenario presumption. Although, depending on the lower mass threshold in their 'compactness' criteria, individual works might be probing a different population of red nuggets. Indeed, for instance, applying a higher mass selection from Trujillo et al. (2009) ($M_*/\mathrm{M}_\odot \sim 8 \times 10^{10}$) would return a lower number density compared to that of Poggianti et al. (2013b) ($M_*/\mathrm{M}_\odot \sim 10^{10}$).

Size measurements: The method of size measurement varies slightly between studies. The most commonly used method is fitting a single Sérsic $R^{1/n}$ model to the surface brightness profile of the galaxies (e.g. Daddi et al. 2005; Trujillo et al. 2007, 2009; Bezanson et al. 2009; Valentinuzzi et al. 2010; Cassata et al. 2011; Mancini et al. 2010; Saracco et al. 2010; Poggianti et al. 2013a; Barro et al. 2013; van der Wel et al. 2014; van Dokkum et al. 2015). From this, the effective radius R_e (essentially the half-light radius $R_{1/2}$) is generally used to represent the size of a galaxy in discussions. Some studies, however, fit the de Vaucouleurs (1948) $R^{1/4}$ model instead. For example, Taylor et al. (2010) rely on the parametric measurements from Strauss et al. (2002), who used an $R^{1/4}$ model to describe the galaxy surface brightness profiles (see also section 3.2 in Taylor et al. 2010, for a relevant discussion). For red nuggets, Damjanov et al. (2009) fit the $R^{1/4}$ model to their MUNICS (Drory et al. 2001) data and both $R^{1/4}$ and $R^{1/n}$ models to their GDDS (Abraham et al. 2004) data. If one assumes an $R^{1/4}$ model, the effective radius could be overestimated if the galaxy has a Sérsic index $n < 4$. In Column (3) of Table 5, we list the measurement method.

The colour of an image also affects its size measurement (Kelvin et al. 2012; Vulcani et al. 2014; Kennedy et al. 2016). In Column (4) of Table 5, we show the band in which the study was conducted. Importantly, the size of early-type galaxies is smaller in the red band as compared to the blue band. As seen in La Barbera et al. (2010), there is a size decrease by 30 per cent from g- through K-band, and a 25 per cent decrease from the H_{160} to the r_{625} filter (Marian et al. 2018).

Stellar mass: The galaxy stellar mass can be estimated via broad-band SED fitting (e.g. Daddi et al. 2005; Longhetti et al. 2007; Kriek

Table 5. The underlying characteristics of different surveys spanning a range of redshifts.

Data source (1)	Unique selection conditions (2)	Galaxy model (3)	Photometry (4)	Adopted IMF (5)	Lower mass limit ($M_*/\mathrm{M}_\odot$) (6)
$z \sim 0$					
Bezanson et al. (2009)	'E' [a]	$R^{1/n}$ ($n \leq 4$) [a2]	V-band	Kroupa (2001)	10^{11}
Trujillo et al. (2009)	'Q' & 'SF' [b]	$R^{1/n}$	r-band	Kroupa (2001)	8×10^{10}
Taylor et al. (2010)	'Q' & 'SF' [c]	$R^{1/4}$	z'-band	Chabrier (2003)	5×10^{10}
Poggianti et al. (2013b)	'Q' & 'SF' [d]	$R^{1/n}$	H-band	Kroupa (2001)	10^{10}
$0.2 < z < 1.0$					
Valentinuzzi et al. (2010)	'Q' & 'SF' [e]	$R^{1/n}$	V-band	Salpeter (1955), Kroupa (2001)	5×10^{10}
Carollo et al. (2013)	'E/S0' & 'Sa-cd' [f]	$R_{1/2}$ [b2]	I-band	Salpeter (1955)	3.1×10^{10}
Damjanov et al. (2015a)	–	$R^{1/n}$	I-band	Kroupa (2001)	$1–5 \times 10^{10}$
$1.0 < z < 3.0$					
Daddi et al. (2005)	–	$R^{1/n}$	i-,z-band	Salpeter (1955)	10^{11}
Trujillo et al. (2007)	$n = 2.5$ divide [g]	$R^{1/n}$	I-band	Chabrier (2003)	10^{11}
van Dokkum et al. (2008)	–	$R^{1/n}$	H-band	Kroupa (2001)	10^{11}
Damjanov et al. (2009)	–	$R^{1/4}$ or $R^{1/n}$	H-band	Baldry & Glazebrook (2003) [a3]	2.5×10^{10}
	–	$R^{1/4}$	H-band	Salpeter (1955) [b3]	–
Saracco et al. (2010)	$n > 2$ [h]	$R^{1/n}$	z'-band	Chabrier (2003)	3×10^{10}
Cassata et al. (2011)	'Spheroidal' [i]	$R^{1/n}$	z-, H-band	Salpeter (1955)	10^{10}
Barro et al. (2013)	–	$R^{1/n}$	H-band	Chabrier (2003)	10^{10}
van der Wel et al. (2014)	–	$R^{1/n}$	H-, J-band	Chabrier (2003)	5×10^{10}
van Dokkum et al. (2015)	–	$R^{1/n}$	H_{160}-band	Chabrier (2003)	4×10^{10}

Notes. Columns: (1) Data source; (2) special conditions in the parent sample selection other than (i) low star-formation rate, (ii) stellar mass, and (iii) redshift; see the respective footnotes for more detailed descriptions. (3) size measurement model: $R^{1/4}$ is the de Vaucouleurs (1948) profile and $R^{1/n}$ is the Sérsic (1968) profile; (4) photometric passband in which the size measurement is taken; (5) assumed initial mass function (IMF); and (6) the lower mass limit for the compact criteria. If no clear size–mass selection criteria were used, we show the lower limit in the parent sample selection instead.
Footnotes: [a] Bezanson et al. (2009) selected the parent sample at $z \sim 0$ based on morphologically 'E' type galaxies from Tal et al. (2009) (see their section 2.1.2); [b], [c], [d], and [e]: In their parent sample selection, Trujillo et al. (2009), Taylor et al. (2010), Poggianti et al. (2013b) and Valentinuzzi et al. (2010) did not discriminate between quiescent ('Q') and star-forming ('SF') galaxies; [f]: Carollo et al. (2013) use the non-parametric ZEST + morphological classification algorithms to select for 'E/S0' and 'Sa-cd' galaxies to construct the parent sample; [g]: Trujillo et al. (2007) divided their sample into two groups: the 'spheroid-like' (Sérsic index $n > 2.5$) and 'disc-like' ($n < 2.5$); [h]: Saracco et al. (2010) selects for galaxies from Giavalisco et al. (2004) and excluded those with Sérsic index $n < 2$; [i]: Cassata et al. (2011) select only the galaxies with a spheroidal morphology under visual inspection, which are the 'galaxies with no signs of asymmetry and centrally concentrated' (see their section 2); [a2]: Bezanson et al. (2009) limited the fitting range of the Sérsic index $n \leq 4$ for their local galaxy sample (see their section 2.2); [b2]: Carollo et al. (2013) measured the half-light radius of each galaxy numerically (see their section 3.1). Here, we denote such by '$R_{1/2}$'; [a3], [b3]: The stellar mass of Damjanov et al. (2009)'s GDDS and MUNICS red nuggets are calculated assuming the Baldry & Glazebrook (2003) and Salpeter (1955) IMFs, respectively.

et al. 2008; Barro et al. 2013).[22] The underlying assumptions for such an operation differ between studies and, as we have shown, the stellar mass calculation affects the reported number density. One such factor is the assumed stellar population model. Most works in Table 5 use the Bruzual & Charlot (2003) stellar population model, except for few studies: Valentinuzzi et al. (2010) uses the Maraston (2005) model, where the influence of thermally-pulsating asymptotic giant branch (TP-AGB) stars are considered; Saracco, Longhetti & Andreon (2009) and Cassata et al. (2011) use the updated Charlot & Bruzual models from 2008 (CB08) and 2009 (CB09), respectively. According to Wuyts et al. (2007), assuming a Maraston (2005) model over the Bruzual & Charlot (2003) model will result in a factor of 1.6 decrease in stellar mass. Meanwhile, Salimbeni et al. (2009) found a 0.2 dex decrease in estimated stellar mass if one adopts CB09 rather than the Bruzual & Charlot (2003) model.

Another factor is the choice of the initial mass function (IMF). Here, we only show, in Column (5) of Table 5, the IMF used in the respective studies for reference purposes. The Chabrier (2003) IMF is the most widely-used and also the most bottom-light compared to the other contemporaries. The CANDELS-based (Grogin et al. 2011; Koekemoer et al. 2011) size evolution studies (Barro et al. 2013; van der Wel et al. 2014; van Dokkum et al. 2015) all assume the Chabrier (2003) IMF. However, some low-to-intermediate redshift studies (Bezanson et al. 2009; Valentinuzzi et al. 2010; Poggianti et al. 2013b; Carollo et al. 2013) instead assume the more bottom-heavy Salpeter (1955) IMF, or the pseudo-Kroupa IMF (Kroupa 2001) rather than the Kroupa (2002) IMF. Using a Chabrier (2003) IMF will yield 0.24 dex less mass than the Salpeter (1955) IMF (Salimbeni et al. 2009). A bottom-heavy IMF could result in higher stellar mass, and therefore, more spheroids will be included by the 'compact massive' selection criteria.

Compactness criteria: As discussed in Section 4.3, the compactness criteria are usually somewhat arbitrary or it borders the distribution of the general galaxy population's size–mass relation. The lower mass limit, in particular, can alter the number density of 'compact' systems in one's sample. We have listed the lower mass limit for each study in Column (6) of Table 5. If the study did not apply a clear size–mass selection boundary, the lowest mass limit (corresponding to the magnitude limit) of the parent sample is provided. These lower mass limits vary from $M_*/\mathrm{M}_\odot = 10^{10}$ to

[22] Among the works listed in Table 5, only Poggianti et al. (2013b) did not perform SED fitting. Their data source from the PM2GC survey (Calvi et al. 2011) estimates the galaxy stellar mass via the Bell & de Jong (2001) M/L relation.

10^{11}. If a study assumes a bottom-heavy IMF and a lower mass limit, one can expect a higher reported number density.

6.2 The possibility of E-to-E evolution

Our work is fundamentally different from the previously mentioned works. By not treating galaxies as single-component systems, our analysis provides additional information on the galaxies' structural features. Based on the RC3 morphology, the frequency of alleged 'E' galaxies in our local sample is abundant. However, after performing analysis and decomposition of the galaxy light, the number of elliptical galaxies is revised downward, already weakening the argument that the high-z red nuggets transformed into today's elliptical galaxies, simply because the actual number of elliptical galaxies is sparse. Only 13/28 originally labelled 'E' galaxies are true ellipticals (11E+2ES, see Section 3.4). This reflects revelations from a quarter of a century ago, whereby the true number of pressure-supported elliptical galaxies was found to be notably lower than previously thought (e.g. D'Onofrio et al. 1995; Graham et al. 1998).

6.2.1 The morphology of host galaxies with an embedded compact massive spheroid

The literature abounds with examples of what were formerly elliptical galaxies that are reclassified as disc galaxies. Early examples are NGC 4111 (E7 → Sa: Adams & Seahes 1937, their p.31) and NGC 3115 (E7 → S0: Burbidge, Burbidge & Fish 1961).

Our results cast doubt on the evolutionary scenario of red nuggets transforming into elliptical galaxies. In Fig. 19, we plot the geometric-mean, i.e. circularized, half-light radius and total mass of the host galaxies, shown by the green plus signs ('+'), and their respective embedded spheroids (shown by the solid red circles). The three prominent outliers are marked with red hollow circles.[23] The sample shown here are the 55 spheroids that satisfy the compact-massive selection criteria of Barro et al. (2013), the most inclusive criteria. We divided the sample into two categories, they are:

(i) spheroids embedded in lenticular galaxies[24] ('S0 hosts', see the upper panel in Fig. 19); and
(ii) spheroids embedded in spiral galaxies ('S hosts', see the lower panel in Fig. 19).

None of the compact massive spheroids, as identified using the selection criteria of Barro et al. (2013), are pure elliptical galaxies. A significant number of compact massive spheroids with stellar masses above (4–5)$\times 10^{10}$ $M_\odot$ come from S0 host galaxies, while those with stellar masses lower than (4–5)$\times 10^{10}$ $M_\odot$ are slightly more likely to come from a spiral host galaxy. Additionally, none of the 11E+2ES galaxies (when using the T11, Z09, or RC15 mass prescriptions) satisfy the 'compact-massive' selection criteria of any paper.[25] What this means is that all of our compact massive spheroids are embedded inside either S0 or early-type S galaxies; none are compact massive elliptical galaxies, although a few such galaxies do exist locally.

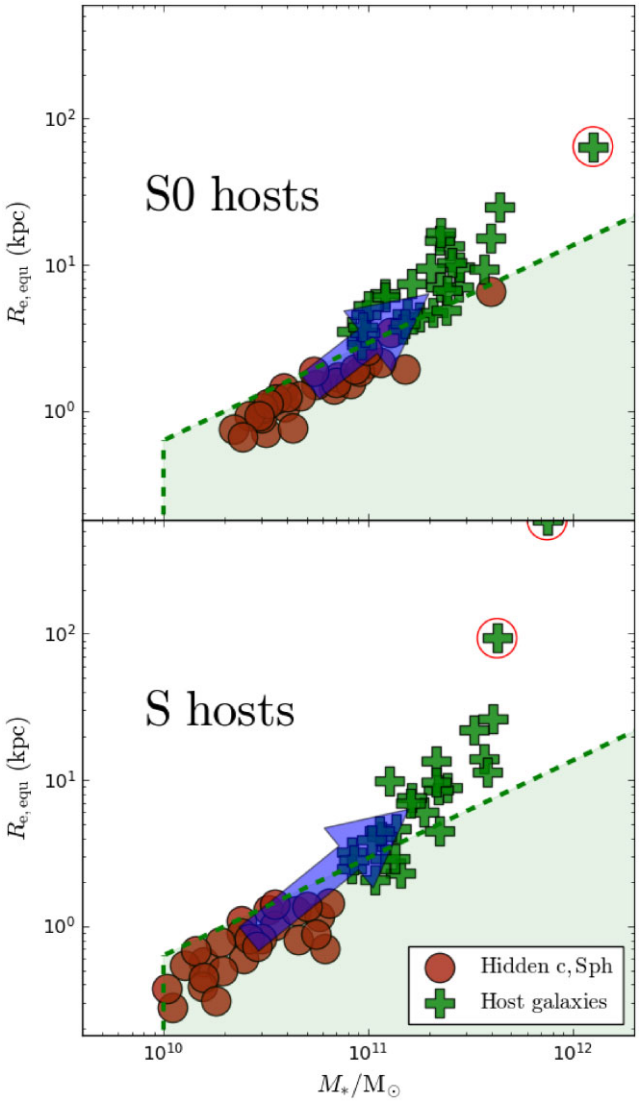

Figure 19. The size–mass (in RC15 mass) distribution of 55 compact massive spheroids according to the size and mass selection criteria shown in equation (11) (green dashed line and the shaded area). The host galaxies' morphologies are based on their reclassifications in Section 3.4. The sample is separated into 'S0 hosts' (upper panel) and 'S hosts' (lower panel). The red solid circles are the compact massive spheroids hidden within the host galaxies (labelled 'Hidden c,Sph') and the green plus signs are the host galaxies (labelled 'Host galaxies'). The size (circularized radius $R_{e,\,eq}$) of the host galaxy is obtained via a single Sérsic fit to the surface brightness profile. The blue arrows indicate the direction of growth if the high-z compact massive system were to assemble mass via the inside-out, disc cloaking process. We highlighted the three prominent outliers with red hollow circles.

[23]For the sake of mimicking how most studies measure galaxy size, we use a single Sérsic function to measure the host galaxy's effective radius, although we know it is not the best measurement for some galaxies (see also Appendix C). Case in point, the three outliers are NGC 3158 (S0), IC 983 (S), and NGC 3646 (S). All have a disc component with a rather shallow profile and large scale length $h > 20$ kpc. Combined with a prominent bulge, this creates a curvature in the surface brightness profile that requires a single Sérsic function with an exceptionally high index ($n > 5$). This highlights a problematic issue with the conventional method of measuring galaxy size and shall be pursued further in future work.

[24]The morphologies here refers to the reclassification we introduced in Section 3.4.

[25]Only when applying the highest stellar mass estimation (IP13), did we find 3, 3, and 4 'compact massive' galaxies when using the Barro et al. (2013), Damjanov et al. (2014), and van Dokkum et al. (2015) selection criteria, respectively. However, because IP13 assumes a different IMF comapred to these studies, it is not exactly a fair comparison.

6.2.2 3D envelopes

Hopkins et al. (2009) proposed an evolutionary pathway for red nuggets, where, through dry minor mergers, the high-z compact galaxies develop a pressure-supported 3D envelope to become the cores of today's elliptical galaxies. This is a different evolutionary path to acquiring a rotating 2D disc to become the bulges of today's lenticular galaxies. The answer to differentiating between these two evolutionary paths depends on understanding the surface density profiles of massive local galaxies as a function of radius. One can also resort to kinematic information to ascertain the presence of a rotating disc. Hopkins et al. (2009) investigated 180 early-type galaxies from Lauer et al. (2007) and Kormendy et al. (2009), and found similarities between the inner part, ∼(1–5) kpc, of the local early-type galaxy light profiles and the distant compact massive quiescent galaxies in the sample of van Dokkum et al. (2008). Earlier in the same year, Bezanson et al. (2009) had reached a similar conclusion, stating that the inner ($R < 1$ kpc) stellar densities of local elliptical galaxies are similar to the high-z red nuggets. Possibly due to the difficulty distinguishing E from S0 among ETGs, papers advocating for an E-to-E evolution kept emerging (e.g. Oldham et al. 2017; Tortora et al. 2020; Zhu, Ho & Gao 2021), despite the fact that the similarity of the profile's inner density did not actually prove the proposed E-to-E evolution over an E-to-S0 evolution. Arnold et al. (2011) suggested minor mergers were building a pressure-supported halo around NGC 3115. De, Chattopadhyay & Chattopadhyay (2014) reported structural similarity in the inner part at radius $R < 1$ kpc of local early-type galaxies with the red nuggets at $2 < z < 7$, and virtually no correlation at $R > 10$ kpc. However, information on the $z \sim 0$ number density of S0 galaxies with compact massive cores is needed. This required identifying which early-type galaxies are S0 or E, or ES.

While the studies mentioned above provide a legitimate argument for the inside-out growth scenario, our result provides additional insight into the nature of this evolution. Those studies generally did not attempt to separate the early-type galaxies into a disc (lenticular) and no-disc (true elliptical) systems. By and large, they assumed evolution into larger pressure-supported systems rather than entertaining the notion of substantial disc growth to create a different type of galaxy with significant ordered motion. Barbosa et al. (2021b) conducted a detailed kinematic and population analysis on a bona fide elliptical, NGC 3311, and found a compact core, a high-z 'relic' galaxy, is hidden inside $R < 2$ kpc. Similar studies would be much welcomed to confirm an E-to-E transition. Our bulge-to-disc and disc-to-total ratios reveal that the discs, and their bars and ansae, are nowadays the dominant mass component in many local massive galaxies. This has considerable implications on many fronts, such as the inferred dark matter haloes of massive early-type galaxies implied from their central velocity dispersion, σ, via the expression $M \sim \sigma^2 R_{\rm e,\,gal}$ (e.g. Poincare & Vergne 1911; Zwicky 1937; Poveda 1958, 1961). Obviously, the larger $R_{\rm e,\,gal}$ radii, which are dominated by the size of the disc, is not applicable for use in this expression for a virialized, pressure-supported galaxy.

Hopkins et al. (2009) used data from Kormendy et al. (2009), a selected set of 27 elliptical (E) galaxies from the Virgo Cluster and with very few massive galaxies ($M_* > 3 \times 10^{11}$ M$_\odot$). They modelled all the E galaxies with a single Sérsic fit. However, upon inspection, some of these galaxies exhibit features which may be a signature of a rotational component. For instance, there is a rising ellipticity ϵ profile in IC 3381, IC 3490, IC 3509, NGC 4387, NGC 4482 NGC 4486 and NGC 4636, a typical sign for an extended disc; high ellipticity section ($\epsilon > 0.4$) in the ϵ profile: NGC 4464, NGC 4467, NGC 4478, NGC 4515, and NGC 4621 which could indicate the existence of intermediate scale disc. Hopkins et al. (2009) also used data from Lauer et al. (2007) based on 219 early-type galaxies taken from different sources (Lauer et al. 1995; Faber et al. 1997; Quillen, Bower & Stritzinger 2000; Ravindranath et al. 2001; Rest et al. 2001; Laine et al. 2002; Lauer et al. 2005). In terms of morphologies, roughly half of the sample was thought to be 'E', a quarter of them 'S0', and the other quarter 'BCG' according to the RC3 classifications. Most BCGs are ellipticals, yet without a multicomponent analysis of kinematic data, the nature of the alleged 'E' galaxies is not confirmed.

The local galaxy sample used by Bezanson et al. (2009) came from Tal et al. (2009), with well-defined distances (15 Mpc < Dist. < 50 Mpc) and absolute magnitude ($\mathfrak{M}_B < -20$ mag). They pointed out half of their sample exhibits morphological disturbance features, such as shells and tidal tails, implying heavy interactions with their environments.

De et al. (2014) supports the 3D envelope scenario based on the three-Sérsic-component decompositions by Huang et al. (2013) on the Carnegie-Irvine Galaxy Survey data (Ho et al. 2011). The 94 galaxies they investigated used to model listed as 'E' in the RC3 classifications. Huang et al. (2013) used three Sérsic functions to describe the inner, middle, and outer region of the galaxy. They found a high correlation between the inner region of the local galaxies and the high-z red nuggets but not the outer region, hence concluding the red nuggets went through a multistage buildup in an inside-out manner. This, however, does not rule out disc growth. Indeed, as Huang et al. (2013) pointed out in their table 1, the following galaxies have an edge-on disc: ESO 221-G026, NGC 3585, and NGC 7029, and these: IC 4797, NGC 584, NGC 3904, NGC 4033, NGC 4697, NGC 6673, NGC 7145, NGC 7192, NGC 7507 are possibly S0 galaxies. Instead of a multi-layered elliptical galaxy, there could be many S0 galaxies in the mix, and the inner region of these galaxies is, in fact, the bulge.

As we have established in Section 3.4, without exploring the galactic substructure, the morphology of early-type galaxies is often mistaken. Instead of comparing the high-z quiescent galaxies to true elliptical galaxies, the comparisons are essentially being made using many local lenticular galaxies. It is likely that many of the alleged low-density 3D envelopes are actually 2D rotating discs seen somewhat face-on. Rather than evidence of 3D envelope growth, many of the galaxies used in the above studies instead support the 2D disc cloaking process.

6.3 Disc growth

6.3.1 Evidence of disc accretion

Lyman-α gas clouds are observed within 500 kpc of high-z galaxies of all types (Wakker & Savage 2009; Prochaska et al. 2011; Thom et al. 2011; Stocke et al. 2013; Tumlinson et al. 2013). For instance, Bouché et al. (2013) used a background quasar to trace the nearby gas (damped Lyman absorber 26 kpc away) of a star-forming galaxy at $z = 2.3$ with a typical rotational disc, according to its kinematics (Förster Schreiber et al. 2009). The kinematics of the gas shows a signature of cold accretion, where it appears to be low-metallicity, co-planar, and co-rotational compared to its disc. In the local Universe, Coccato et al. (2013) examined the two counter-rotating discs in both NGC 3593 (S0/a) and NGC 4550 (S0), where the secondary discs differ from the primary discs in metallicity and stellar populations. They favour a scenario of gas accretion forming the second disc ∼2–7 Gyr ago.

High-z red nuggets are reported to have reached their peak abundance at $z \sim 1.2$–1.6, and dropped in number ever since (Barro et al. 2013; van der Wel et al. 2014; van Dokkum et al. 2015). The disappearance of these galaxies through the growth of discs may involve the creation of star-forming galaxies (should much of the disc stars be built from accreted gas) or not (when the bulk of the disc is built from accreted galaxies with little gas).

There is an abundance of evidence from different approaches that confirm the prominence of discs in local early-type galaxies. Kaviraj et al. (2007) investigated the UV and optical photometry of ∼2100 SDSS early-type galaxies at $0 < z < 0.11$ and found at least ∼30 per cent exhibit recent (∼1 Gyr ago) star formation activity. Fabricius et al. (2014) performed a detailed analysis of NGC 7217, a spheroid-dominated galaxy (classified as an early-type spiral in Buta et al. 1995) with two distinct rotational components. The active star formation of the rotational structures suggested an ongoing (re)growth of the stellar disc. While this process is truncated in cluster environments, it can still occur in the field (e.g. Graham et al. 2017).

While 'cosmic noon' has passed, and there are less substantial cold gas clouds nearby for galaxies to accrete, it is an ongoing, downsizing phenomenon. The kinematics of the gas shows a signature of cold accretion, where it appears to be low-metallicity, coplanar, and corotational compared to its disc (see also, Kacprzak et al. 2010, 2015; Stewart et al. 2013; Nielsen et al. 2017; Martin et al. 2019; Zabl et al. 2019). Davis et al. (2011) examined the gaseous content of local early-type galaxies with CO and H I interferometric observations. The kinematic misalignment between the gas and stellar components implied that 42 per cent of the gas in field galaxies (fast rotators) is ex situ in origin, namely from cold accretion and minor mergers.[26] Alatalo et al. (2013) investigated the morphology of molecular gas through CO imaging by the CARMA ATLAS^{3D} survey, finding half of the 40 CO-rich early-type galaxies exhibit a CO disc. They estimated (with a correction factor from Kaviraj et al. 2012) the lower mass limit to the total accreted gas to be $2.48 \times 10^{10}\,\mathrm{M}_{\odot}$ across 15 galaxies, a value consistent with the mass brought in by minor mergers (Lotz et al. 2008) and thus the accretion of not just gas but also stars from smaller galaxies.

As mentioned before, the extensive kinematic observations from the ATLAS^{3D} survey revealed that the majority of the local early-type galaxies are 'fast rotators' (Emsellem et al. 2011). Krajnović et al. (2011) shows that most early-type galaxies (∼82 per cent) are 'regular rotators' (defined in *Kinemetry*, Krajnović et al. 2006, 2008), in the sense that the velocity maps are dominated by ordered rotation. Krajnović et al. (2013b) performed Bulge + Disc decompositions on a set of 180 of the non-barred galaxies. They found that galaxies with high angular momentum (λ_e) also have a large disc-to-total flux ratio. The combination of kinematics and photometric results revealed that 83 per cent of their early-type galaxies have a rotational disc that accounts for around ∼40 per cent the stellar mass of a galaxy.

Our result highlighted the abundance of discs in massive local galaxies, providing strong support for the disc growth (cloaking) scenario. The cyclical nature of galaxy metamorphosis has been recognized widely in simulations (White & Rees 1978; Navarro & Benz 1991; White & Frenk 1991; Bournaud & Combes 2002; Steinmetz & Navarro 2002). If disc cloaking were to occur to our spheroids, and, subsequently, build up an extended disc and other substructures in an inside-out manner, the systems will experience growth in both size and mass. They would migrate outward (see the blue arrows, in Fig. 19) from the compact massive region (the green shaded area) in the size–mass diagram and become the massive ($M_*/\mathrm{M}_{\odot} > 10^{11}$) local S0 and S galaxies. Depending on the nature of the minor mergers (wet or dry) and the amount of cold stream gas accretion, the galaxies may also migrate outside of the 'quiescent' region in the colour–colour diagram to enter the 'star-forming' blue region because of the newly built rotational discs. With time, star formation in these discs turns off, and a quenched, lenticular galaxy now moves back into the 'quiescent' region with a larger overall size.

6.4 Important caveats

6.4.1 The role of IMF in stellar mass estimation

It is questionable whether there is a universal IMF among galaxies (Cenarro et al. 2003; Bastian, Covey & Meyer 2010; van Dokkum & Conroy 2010; Cappellari et al. 2012; Ferreras et al. 2013; La Barbera et al. 2013; Smith 2014; Spiniello et al. 2014). The slope of the low-mass end of the IMF is thought to be directly correlated with the velocity dispersion of galaxies (Ferreras et al. 2013; Domínguez Sánchez et al. 2019) and, consequently, the colour of galaxies (Dutton, Mendel & Simard 2012; Pforr, Maraston & Tonini 2012; Ricciardelli et al. 2012; Vazdekis et al. 2012). For example, Martín-Navarro et al. (2015) analysed the 'relic' galaxy NGC 1277 (Graham et al. 2016a) that is compact (1–2 kpc) and has an exceptionally high velocity dispersion ($\sigma > 400\,\mathrm{km\,s^{-1}}$, see also Ferré-Mateu et al. (2017) for its detailed features). However, the IMF correlation with velocity dispersion has been called into doubt. Importantly, from one BCG, NGC 3311, Barbosa et al. (2021a) presented an important case showing the IMF-σ correlation to be invalid, a mere coincidence that old stars are found in the area of a galaxy with high dispersion. They found the tightest relations to be between stellar age-to-IMF and radius-to-IMF. They found the IMF to be bottom-heavy and requiring a high Υ_*. Ferré-Mateu, Vazdekis & de la Rosa (2013) has shown the non-universality, whereby adjusting the slope of the IMFs according to the central velocity dispersion yields a more comparable star formation history among the early-type galaxies. While Smith (2014) pointed out the discrepancy between methods for probing the IMF of galaxies, based on the data from ATLAS^{3D} and Conroy & van Dokkum (2012b), there was a broad agreement that elliptical galaxies have a more bottom-heavy IMF.

If a bottom-heavy IMF is indeed better suited for high dispersion galaxies, then among the MLCRs in Section 2.3, IP13 perhaps portrays a more accurate stellar mass since it assumes the Kroupa (1998) IMF – yielding $\log(M_*/L)$ ratios 0.225 dex lower than those obtained with the Salpeter (1955) IMF, see Flynn et al. (2006, their fig. 12) – instead of the more bottom-light Kroupa (2002) IMF or the Chabrier (2003) IMF (see also Ferreras et al. 2013; Kroupa et al. 2013). Although, there is plenty of evidence (Cenarro et al. 2003; Falcón-Barroso et al. 2003; Vazdekis et al. 2003; van Dokkum & Conroy 2010; Spiniello et al. 2012; Conroy & van Dokkum 2012a, b; van Dokkum & Conroy 2012) indicating there are more low-mass stars in elliptical galaxies than even the most bottom-heavy IMF (Salpeter 1955) predicts. This implies that even our highest mass estimation (the IP13 masses) is an underestimation of the real stellar mass. Throughout this work, however, the relative stellar mass compared to the high-z measurements is more important to us. Because the studies of high-z red nuggets assume a bottom-light Chabrier (2003) IMF, for comparison purposes, we need to apply the same assumption as we estimate the spheroids' stellar mass (T11 and

[26]Note that only 22 per cent of early-type galaxies in their survey has detectable molecular gas (Young et al. 2011). The gas content in local early-type galaxies is evident but not at all prominent.

RC15 MLCRs), even if the real stellar mass is larger than what was presented in Fig. 15.

6.4.2 *The similarity between local spheroids and distant red nuggets*

In order to fully prove that high-z red nuggets and local spheroids are drawn from the same population, we need matching sizes, stellar masses (and thus stellar densities), internal dynamic features and stellar populations. Such a full comparison for our sample is beyond the scope of this paper but is perhaps not required given the extensive evidence in the literature.

The bulges of lenticular galaxies and high-z quiescent galaxies both have high velocity dispersions. For example, Martinez-Manso et al. (2011) reported on a range of dispersions, $\sigma \sim 156$–$236\,\mathrm{km\,s^{-1}}$, for four red nuggets at $z \sim 1$ taken from Trujillo et al. (2007). van de Sande et al. (2013) measured five galaxies at $z \sim 2$ to have $\sigma \sim 290$–$450\,\mathrm{km\,s^{-1}}$. These highest values appear as outliers after Belli, Newman & Ellis (2014) analysed 56 quiescent galaxies at $0.9 < z < 1.6$ and obtained each galaxy's mean velocity dispersion within $R_{\mathrm{e,\,gal}}$. They found an average $\langle\sigma_{\mathrm{e}}\rangle$ value of $219\,\mathrm{km\,s^{-1}}$. For comparison, in the local Universe, the MASSIVE survey (Ma et al. 2014) reports on the central velocity dispersions σ_{c} for 90 early-type galaxies within 104 Mpc. They are in the range of $\sigma_{\mathrm{c}} \sim 200$–$350\,\mathrm{km\,s^{-1}}$ (Veale et al. 2017). In the redshift range $0.15 \lesssim z \lesssim 0.5$, Scognamiglio et al. (2020) detected 19 UCMGs ($M_*/\mathrm{M}_\odot > 8 \times 10^{10}$ and $R_{\mathrm{e}} < 1.5$kpc) spanning a range of $200 \lesssim \sigma/\mathrm{km\,s^{-1}} \lesssim 400$ (see also, Tortora et al. 2016, 2018, 2020; Barbosa et al. 2021b).

Local spheroids are also known to contain old stellar populations that existed at high-z. Saracco et al. (2009) showed 32 early-type galaxies at $1 < z < 2$ which exhibit two distinct stellar populations: the old (∼3.5 Gyr) and young (∼1 Gyr) stars, implying the early-type galaxies exist at least since $z > 3$–3.5. Peletier et al. (2007) also reached the same conclusion from the perspective of stellar velocity dispersion dips. MacArthur et al. (2009, see their table 4) found that in local spiral galaxy bulges, old stellar populations (>10 Gyr) make up the majority of the mass budget. Regardless of whether the bulges of local galaxies formed via outside-in (i.e. secular evolution) or inside-out (i.e. mergers and/or accretion) scenarios, the structural similarity to high-z red nuggets is now well established. Although, evidence from stellar population studies (Proctor & Sansom 2002; Moorthy & Holtzman 2006; Thomas & Davies 2006; Jablonka, Gorgas & Goudfrooij 2007; MacArthur et al. 2008; Saracco et al. 2009) favour the inside-out process in early-type galaxies.

The stellar densities are also comparable between local bulges and high-z red nuggets (Graham 2013, his fig. 1), which have half-light densities higher than local early-type galaxies of the same mass. This is because the discs of local lenticular galaxies – which tend to dominate these galaxies' stellar mass budget – increase the galaxies' half-light radii but not in an economical space-filling fashion. The Bulge + Disc decompositions from de la Rosa et al. (2016) also show the size–mass relation overlaps (see their fig. 3); the red nuggets at $0.18 < z < 1$ share almost the same relation and galaxies at $1 < z < 1.8$ have a similar slope, but are slightly more compact. Graham (2013) further showed that local dwarf 'compact elliptical' (cE) galaxies have similar sizes, stellar masses, and densities as local low-mass bulges, suggesting that they are the (largely) disc-free counterparts of lower mass bulges, just as red nuggets are the (largely) disc-free counterparts of high-mass bulges.

Graham et al. (2015) also illustrated that the overlap in the (Sérsic index, n)–(effective radius, R_{e}) diagram (their fig. 3, primarily from Bulge + Disc decompositions of local galaxies) between bulges and high-z red nuggets from Damjanov et al. (2011). Given the structural similarity, they, therefore, concluded that not all compact massive *spheroids* have gone through significant size evolution since $z < 2.5$.

6.4.3 *Contributions from the Virgo Cluster*

Bin 3 is of particular interest. Bin 3 captured galaxies within Dist. < 45 Mpc, a space containing the Virgo Cluster. Not only is it complete down to the lowest galaxy stellar mass (M_* (IP13) $= 10^{11}\,\mathrm{M}_\odot$), it also yields the highest number density for compact massive spheroids.

In Fig. 20, we show the location of our host galaxies in the sky. Small black dots are all the galaxies in the SDSS field bounded by our angular selection (equation 1). One can clearly see the large-scale filament structures in the local Universe manifesting. The blue points are the 103 host galaxies in our sample. Since we only select for massive galaxies, it is natural that most of them live in dense environments. One can see the blue points largely coincide with the overdensity regions. The red points are the Virgo Cluster host galaxies. There are 22 out of 52 galaxies in Bin 3 that are in the Extended Virgo Cluster Catalogue (EVCC; Kim et al. 2014a).

Using the less restrictive Barro et al. (2013) and Damjanov et al. (2014) sample selection criteria, Bin 3 is more abundant with compact massive spheroids than the peak of the red nugget population ($n_{\mathrm{c,Sph,Bin3}} > \max(\mathrm{n_{RN}})$) across all stellar masses. Note that the $n_{\mathrm{c,\,Sph,\,Bin3}}$ here corresponds to the respective 'compact massive' selection criteria as the high-z nuggets' peak abundance ($\max(\mathrm{n_{RN}})$). When using the more restrictive selection criteria from van der Wel et al. (2014) and van Dokkum et al. (2015), our result varies depending on the stellar mass estimates (Fig. 18). With T11 and Z09 stellar mass, no compact massive spheroid was found in Bin 3 with the restrictive van der Wel et al. (2014) and van Dokkum et al. (2015) criteria. With RC15 stellar mass, Bin 3 has a lower number of compact massive spheroids to the red nuggets, $n_{\mathrm{c,Sph,Bin3}} < \max(\mathrm{n_{RN}})$ (around 0.66–0.78 difference). Finally, in IP13 stellar mass, $n_{\mathrm{c,\,Sph,\,Bin3}}$ is slightly higher than $\max(\mathrm{n_{RN}})$, by 38 per cent in van der Wel et al. (2014) criteria and 52 per cent in van Dokkum et al. (2015) criteria.

The high number density in Bin 3 reinforces the idea that the cloaking process is more prevalent among the low-mass spheroids ($1 \times 10^{10} < M_{*,\,\mathrm{Sph}}$ (RC15)/$\mathrm{M}_\odot < 4 \times 10^{10}$). Because Bin 3 has a lower stellar mass selection limit as compared to Bins 1 and 2, it samples some extra low-mass galaxies ($6.7 \times 10^{10} < M_{*,\mathrm{gal}}/\mathrm{M}_\odot$ (RC15) $< 1.3 \times 10^{11}$). The low-mass spheroids are likely to experience drastic disc growth since $z \sim 1.5$, creating galaxies with stellar mass range $6.7 \times 10^{10} < M_{*,\mathrm{gal}}/\mathrm{M}_\odot$ (RC15) $< 1.3 \times 10^{11}$, thereby increasing the number density in Bin 3.

Having roughly half of the galaxies in Bin 3 being Virgo Cluster members, we examine if the cluster affects the estimation of the number density of the compact massive spheroids. We do so by removing the Virgo Cluster galaxies from our sample and recalculating the number density of compact massive spheroids in Bin 3. Table 6 shows the resulting number densities using the four criteria for defining compact massive spheroids (Barro et al. 2013; van der Wel et al. 2014; Damjanov et al. 2014; van Dokkum et al. 2015) and using the four stellar mass estimates (T11, Z09, IP13, RC15).

With the restrictive selection criteria (van der Wel et al. 2014; van Dokkum et al. 2015), we found a similar number of compact massive

Table 6. The number densities of Bin 3 after removing Virgo Cluster galaxies.

MLCR Criteria	T11 $n_{c,Sph,Bin3}/Mpc^{-3}$ (#)	Z09 $n_{c,Sph,Bin3}/Mpc^{-3}$ (#)	RC15 $n_{c,Sph,Bin3}/Mpc^{-3}$ (#)	IP13 $n_{c,Sph,Bin3}/Mpc^{-3}$ (#)
Barro et al. (2013)	3.1×10^{-4} (10)	3.1×10^{-4} (12)	4.3×10^{-4} (14)	6.4×10^{-4} (21)
van der Wel et al. (2014)	0	0	0	9.2×10^{-5} (3)
van Dokkum et al. (2015)	0	0	3.1×10^{-5} (1)	1.2×10^{-4} (4)
Damjanov et al. (2014)	3.7×10^{-4} (12)	4.3×10^{-4} (14)	5.0×10^{-4} (16)	7.1×10^{-4} (23)

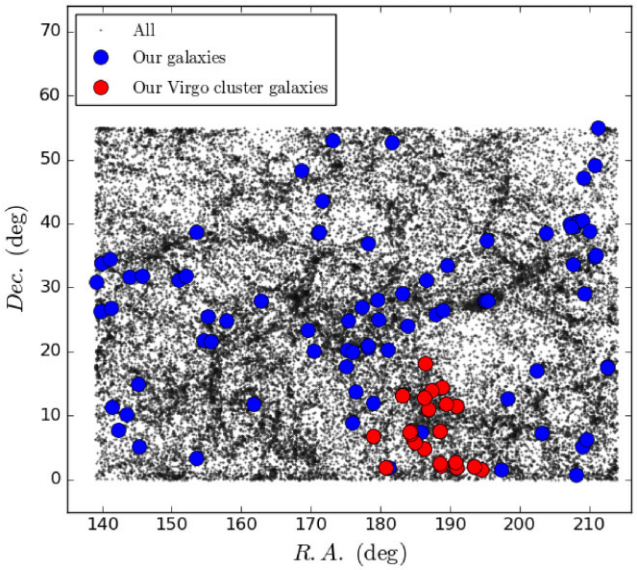

Figure 20. The spatial distribution of the galaxies. The parent sample selected by the angular boundaries from equation (1) is marked in black dots. The 103 galaxies selected by the three bins (equation 5) are marked as the blue circles. Among these 103 galaxies, the ones that are the members of the Virgo Cluster are marked as red circles.

spheroids as before. With the less restrictive selection criteria (Barro et al. 2013; Damjanov et al. 2014), the numbers of compact massive spheroids are roughly halved. Because the reduction (∼58 per cent–61 per cent) is comparable to the number of removed Virgo members (∼42 per cent), we, therefore, conclude the Virgo Cluster overdensity does not increase Bin 3's number density in any significant way. Our wide-sky coverage prevented a potential bias as the Virgo Cluster takes up less than one-eighth of the area in the R.A. and Dec selection window (see Fig. 20). Moreover, with the reduced number densities ($n_{c,\,Sph,\,Bin3} \approx (0.3–5.0) \times 10^{-4}\,Mpc^{-3}$), Bin 3 still contains a comparable number of compact massive spheroids to the peak red nugget density ($max(n_{RN}) \approx (1.8–2.4) \times 10^{-4}\,Mpc^{-3}$). Thus, even without the influence of the Virgo Cluster, there remains a sizable amount of compact massive spheroids in Bin 3, sufficient to account for the missing red nuggets.

6.4.4 Some distant red nuggets may also have discs

It is unclear whether the original red nuggets (from Daddi et al. 2005; van Dokkum et al. 2008; Damjanov et al. 2009) are devoid of any disc growth. From visual inspection, some galaxies exhibit discy, high-ellipticity isophotes. For example, galaxy numbers: '4950' ($z = 1.55$) from Daddi et al. (2005); '1030-1813' ($z = 2.56$), '1030-2559' ($z = 2.39$), '1256-142' ($z = 2.37$), and 'HDFS1-1849' ($z = 2.31$) from van Dokkum et al. (2008); and '22-0189' ($z = 1.49$), '15-4367' ($z = 1.725$), 'S7F5_254' ($z = 1.22$), and 'S7F5_045' ($z = 1.45$) from Damjanov et al. (2009).

The existence of (nascent) discs in some high-z galaxies is supported by van der Wel et al. (2011). They found a significant portion of the compact massive quiescent galaxies ($M_*/M_\odot > 10^{10.8}$, and $R_e < 2$ kpc) are flattened in projection, thus concluding that 40 per cent–65 per cent of red nuggets at $z \sim 2$ are disc-dominated. Ferré-Mateu et al. (2012) also found elongated morphologies in red nuggets at $z > 1$ and classified them as fast rotators. One may therefore question whether those red nuggets are genuinely single-component systems. While spheroids can rotate, it is certainly the case that the low-resolution of images at high-z will blend the bulges and discs together to create the appearance of a single-component system. Indeed, even at low z, astronomers have struggled for a century to separate S0 galaxies from E galaxies. As such, the disc inclination angle and dust content will further complicate the situation. The shrouding dust heated by star formation will redden the galaxies' light (Pérez-González et al. 2008). Interestingly, a few notable local 'relic' galaxies (NGC 1277, PCG 032873, and Mrk 1216), that are believed to be untouched by ex-situ processes, have strong stellar rotation. NGC 1277 has a rotational velocity $v_r \sim 300$ km s^{-1} in the outer region and a central velocity dispersion $\sigma_0 > 300$ km s^{-1} (Trujillo et al. 2014). In (Ferré-Mateu et al. 2017, see their fig. 2), both PCG 032873 and Mrk 1216 exhibit a rotational velocity of $v_r \sim 200$ km s^{-1} and central dispersion of $\sigma_0 \sim 320$ km s^{-1}, implying, indeed, they are not single-component systems. These systems may have accreted and grown their discs. Until they transition through the ES to S0 phase, they may remain compact massive galaxies. This may even conceivably explain some of the youthfulness seen in some ultracompact massive galaxies (Spiniello et al. 2021), although we note this is just speculation on our part.

It will be interesting to perform structural decompositions on intermediate- and high-z galaxies when high-quality images become available from facilities such as the European Southern Observatory's Very Large Telescope interferometer, equipped with PIONIER (1.6 μm; Le Bouquin et al. 2011), GRAVITY (2.0–2.4 μm imager; 4 mas seeing using the four 8-m Unit Telescopes; Gillessen et al. 2010; Eisenhauer et al. 2011), and MAVIS (optical, under development; McDermid et al. 2020; Rigaut et al. 2020). Subsequently, cosmological simulations involving disc cloaking can be tested if the observed high-mass end of the spheroid mass function, and the spheroid size–mass relation can be reproduced, reported here for the local Universe. Careful analysis will enable one to measure the growth of discs in early-type galaxies, shifting the focus away from spheroids – which appear to be relatively inert.

6.5 Summary and conclusions

We defined volume- and mass-limited samples of local galaxies from the SDSS that are nondiscriminatory against galaxy morphology (Section 2). The galaxies have masses greater than $10^{11}\,M_\odot$ and

reside within 110 Mpc. We have discussed how the different mass-to-light ratios (Section 2.3) and distance measurements (Section 2.4) would affect the estimation of the stellar masses and sizes of the galaxies and their spheroids. A detailed, case-by-case study of 103 galaxies was undertaken. We performed multicomponent decompositions (Section 3.3) on the surface brightness profiles of each galaxy. Rather than using automated routines which blindly fit several Sérsic components, we carefully examined each image and identified the morphological features that are present. This was further supported by recourse to the literature, in particular, studies including kinematic data or high-resolution *HST* data. This enabled a considerable improvement upon the conventional Bulge + Disc decomposition. Our analysis encompasses the less prominent yet important substructures (i.e. bars, *ansae*, spiral arms, nuclear discs, intermediate-scale discs, etc.), which can skew the bulge parameters if not taken into account. From our investigation, we have made the following observations.

(i) New morphological classifications were required, and made, for the galaxies. Previously overlooked substructures, such as large- and intermediate-scale discs, are now incorporated into the description of the morphology (Section 3.4). This is important because the morphology reflects the physical processes which shaped the galaxies' evolution.

(ii) Implications from the low number of 'true elliptical' galaxies in the local Universe rule out the dominance of the popular E-to-E evolutionary path whereby quasi-spherical 3D envelopes accumulate around red nuggets for relatively low-mass red nuggets ($M_*/\mathrm{M}_\odot < 4 \times 10^{10}$). The possibility of such an E-to-E scenario is discussed in Section 6.2.

(iii) Morphology-dependent B/T flux ratios are presented for the massive galaxies in Fig. 12 (Section 4.1).

(iv) We provided the mass function of the local spheroids down to stellar mass $M_*/\mathrm{M}_\odot \sim (0.24\text{–}1.8) \times 10^{10}$ (Section 4.2). Most massive spheroids ($M_*/\mathrm{M}_\odot$ (RC15) $>3 \times 10^{11}$) are not simultaneously small ($R_\mathrm{e} < 2$ kpc).

(v) The size–mass distribution of the local spheroids is presented (Section 4.3). The number density of 'compact' and 'massive' spheroids is obtained based on five different selection criteria.

(vi) We compared the number density of local compact massive spheroids with intermediate- and high-redshift galaxies. The evolutionary trend for the number density of compact massive quiescent systems is presented in Fig. 17, based on four different sample selection criteria (Sections 5.2 and 5.3).

Two important insights can be drawn from our results:

(i) The local elliptical galaxies are not as abundant as previously believed. Among the 28 supposed elliptical galaxies (E), 20 are actually lenticular galaxies (S0). There are only ∼11 per cent (11/103) true elliptical galaxies, plus 2 ES galaxies, in our sample.

(ii) We found compact massive spheroids hidden in the local lenticular and early-type spiral galaxies. Working with our host galaxies' selection limit ($M_{*,\mathrm{gal}}/\mathrm{M}_\odot$ (RC15) $>6.7 \times 10^{10}$), we present a range of lower limits of the number density to the compact massive spheroid of $n_{\mathrm{c,\,Sph}} \sim (0.17\text{–}1.20) \times 10^{-4}\,\mathrm{Mpc}^{-3}$, as defined by different definitions of 'compact massive' systems. If relatively low-mass ($M_*/\mathrm{M}_\odot \sim (1\text{–}4) \times 10^{10}$) spheroids are included, then there are sufficient numbers of compact massive spheroids ($n_{\mathrm{c,Sph}} \sim 1.20 \times 10^{-4}\,\mathrm{Mpc}^{-3}$) to match the peak in the number density of red nuggets when defined using the same mass and size criteria.
If we select for only high-mass spheroids ($M_*/\mathrm{M}_\odot > 4 \times 10^{10}$), the number densities for compact massive spheroids and true ellipticals are comparable ($n_{\mathrm{c,\,Sph}} \simeq n_{\mathrm{E+ES}}$). However, in the high-mass range, the uncertainty in stellar mass estimation makes it difficult to conclude which evolution dominates by number density alone (Section 5.4). Interestingly, for $M_{*,\mathrm{gal}}/\mathrm{M}_\odot$ (RC15) $>6.7 \times 10^{10}$ and Dist. < 45 Mpc (Bin 3), we found more compact massive spheroids than the red nuggets' peak abundance: $n_{\mathrm{c,Sph,Bin3}} > \max(\mathrm{n_{RN}})$, inspite of the influence from Virgo Cluster galaxies.

Collectively, this calls the frequency of the E-to-E scenario into doubt, while the disc-cloaking scenario is now more salient than ever. An E-to-E evolution and disc-cloaking create distinctly different end products. If we are to truly understand galaxies, and the cosmological evolution of galaxies, this distinction is of key importance.

ACKNOWLEDGEMENTS

This research was supported under the Australian Research Council's funding scheme DP17012923 and by Tamkeen under the New York University Abu Dhabi Research Institute grant CAP^3. This research has made use of the NASA/IPAC Extragalactic Database (NED), which is funded by the National Aeronautics and Space Administration and operated by the California Institute of Technology.

The project is made possible by using the following software packages: `AstroPy` (Astropy Collaboration 2013, 2018), `CMasher` (van der Velden 2020), `IRAF` (Tody 1986, 1993), `ISOFIT` (Ciambur 2015), `Matplotlib` (Hunter 2007), `NumPy` (Harris et al. 2020), `Profiler` (Ciambur 2016), `SAOImageDS9` (Joye & Mandel 2003), `SciPy` (Virtanen et al. 2020), `SExtractor` (Bertin & Arnouts 1996), and `TOPCAT` (Taylor 2005).

All the scripts used in the analysis are available on GitHub (https://github.com/dex-hon-sci/GalSpheroids).

DATA AVAILABILITY

The data underlying this article will be shared upon request to the corresponding author.

REFERENCES

Abraham R. G. et al., 2004, AJ, 127, 2455
Adams W. S., Seahes F. H., 1937, Mount Wilson Obs. Annu. Rep., 9, 1
Aguerri J. A. L., Beckman J. E., Prieto M., 1998, AJ, 116, 2136
Aihara H. et al., 2011, ApJS, 193, 29
Ajhar E. A., Tonry J. L., Blakeslee J. P., Riess A. G., Schmidt B. P., 2001, ApJ, 559, 584
Alatalo K. et al., 2013, MNRAS, 432, 1796
Allen P. D., Driver S. P., Graham A. W., Cameron E., Liske J., de Propris R., 2006, MNRAS, 371, 2
Almoznino E., Loinger F., Brosch N., 1993, MNRAS, 265, 641
Andredakis Y. C., Peletier R. F., Balcells M., 1995, MNRAS, 275, 874
Arnold J. A., Romanowsky A. J., Brodie J. P., Chomiuk L., Spitler L. R., Strader J., Benson A. J., Forbes D. A., 2011, ApJ, 736, L26
Astropy Collaboration, 2013, A&A, 558, A33
Astropy Collaboration, 2018, AJ, 156, 123
Athanassoula E., 2005, MNRAS, 358, 1477
Balcells M., Graham A. W., Peletier R. F., 2007, ApJ, 665, 1084
Baldry I. K., Glazebrook K., 2003, ApJ, 593, 258
Baldry I. K., Glazebrook K., Brinkmann J., Ivezić, Ž., Lupton R. H., Nichol R. C., Szalay A. S., 2004, ApJ, 600, 681
Balogh M. L., Baldry I. K., Nichol R., Miller C., Bower R., Glazebrook K., 2004, ApJ, 615, L101
Barbosa C. E., Spiniello C., Arnaboldi M., Coccato L., Hilker M., Richtler T., 2021a, A&A, 645, L1
Barbosa C. E., Spiniello C., Arnaboldi M., Coccato L., Hilker M., Richtler T., 2021b, A&A, 649, A93

Bardeen J. M., 1975, in Hayli A., ed., Proc. IAU Symp. 69, Dynamics of the Solar Systems. D. Reidel Pub. Co., Dordrecht; Boston, p. 297
Barro G. et al., 2013, ApJ, 765, 104
Bastian N., Covey K. R., Meyer M. R., 2010, ARA&A, 48, 339
Bell E. F., de Jong R. S., 2001, ApJ, 550, 212
Bell E. F., McIntosh D. H., Katz N., Weinberg M. D., 2003, ApJS, 149, 289
Belli S., Newman A. B., Ellis R. S., 2014, ApJ, 783, 117
Bellstedt S., Graham A. W., Forbes D. A., Romanowsky A. J., Brodie J. P., Strader J., 2017, MNRAS, 470, 1321
Bender R., 1988a, A&A, 193, L7
Bender R., 1988b, A&A, 202, L5
Bender R., 1990, A&A, 229, 441
Bender R., Saglia R. P., Gerhard O. E., 1994, MNRAS, 269, 785
Bernardi M., Hyde J. B., Sheth R. K., Miller C. J., Nichol R. C., 2007, AJ, 133, 1741
Bertin E., Arnouts S., 1996, A&AS, 117, 393
Bezanson R., van Dokkum P. G., Tal T., Marchesini D., Kriek M., Franx M., Coppi P., 2009, ApJ, 697, 1290
Binggeli B., Tammann G. A., Sandage A., 1987, AJ, 94, 251
Binney J., 1978, MNRAS, 183, 501
Blakeslee J. P. et al., 2009, ApJ, 694, 556
Blanton M. R. et al., 2003, ApJ, 594, 186
Blanton M. R., Eisenstein D., Hogg D. W., Schlegel D. J., Brinkmann J., 2005, ApJ, 629, 143
Blanton M. R., Kazin E., Muna D., Weaver B. A., Price-Whelan A., 2011, AJ, 142, 31
Bothun G. D., Gregg M. D., 1990, ApJ, 350, 73
Bouché N., Murphy M. T., Kacprzak G. G., Péroux C., Contini T., Martin C. L., Dessauges-Zavadsky M., 2013, Science, 341, 50
Bournaud F., Combes F., 2002, A&A, 392, 83
Bournaud F., Elmegreen B. G., Elmegreen D. M., 2007, ApJ, 670, 237
Brinchmann J., Charlot S., White S. D. M., Tremonti C., Kauffmann G., Heckman T., Brinkmann J., 2004, MNRAS, 351, 1151
Bruzual A. G., 2007a, in Vazdekis A., Peletier R., eds, Stellar Populations as Building Blocks of Galaxies, Vol. 241. Cambridge Univ. Press, Cambridge, p. 125
Bruzual G., 2007b, in Vallenari A., Tantalo R., Portinari L., Moretti A., eds, ASP Conf. Ser. Vol. 374, From Stars to Galaxies: Building the Pieces to Build Up the Universe. Astron. Soc. Pac., San Francisco, p. 303
Bruzual G., Charlot S., 2003, MNRAS, 344, 1000
Buitrago F., Trujillo I., Conselice C. J., Bouwens R. J., Dickinson M., Yan H., 2008, ApJ, 687, L61
Burbidge E. M., Burbidge G. R., Fish R. A., 1961, ApJ, 133, 393
Buta R., van Driel W., Braine J., Combes F., Wakamatsu K., Sofue Y., Tomita A., 1995, ApJ, 450, 593
Buta R., Laurikainen E., Salo H., Knapen J. H., 2010, ApJ, 721, 259
Calvi R., Poggianti B. M., Vulcani B., 2011, MNRAS, 416, 727
Calzetti D., Armus L., Bohlin R. C., Kinney A. L., Koornneef J., Storchi-Bergmann T., 2000, ApJ, 533, 682
Capaccioli M., Caon N., 1992, in Longo G., Capaccioli M., Busarello G., eds, Astrophysics and Space Science Library, Vol. 178, Morphological and Physical Classification of Galaxies. Springer, Dordrecht, p. 99
Capaccioli M., Held E. V., Nieto J.-L., 1987, AJ, 94, 1519
Capaccioli M., Held E. V., Lorenz H., Vietri M., 1990a, AJ, 99, 1813
Capaccioli M., Caon N., Rampazzo R., 1990b, MNRAS, 242, 24P
Cappellari M., 2016, ARA&A, 54, 597
Cappellari M. et al., 2011a, MNRAS, 413, 813
Cappellari M. et al., 2011b, MNRAS, 416, 1680
Cappellari M. et al., 2012, Nature, 484, 485
Cappellari M. et al., 2013, MNRAS, 432, 1862
Carollo C. M. et al., 2013, ApJ, 773, 112
Carrasco E. R., Conselice C. J., Trujillo I., 2010, MNRAS, 405, 2253
Carter D., 1978, MNRAS, 182, 797
Carter D., 1987, ApJ, 312, 514
Cassata P. et al., 2011, ApJ, 743, 96
Cenarro A. J., Gorgas J., Vazdekis A., Cardiel N., Peletier R. F., 2003, MNRAS, 339, L12
Chabrier G., 2003, PASP, 115, 763
Charbonnier A. et al., 2017, MNRAS, 469, 4523
Charlot S., Fall S. M., 2000, ApJ, 539, 718
Ciambur B. C., 2015, ApJ, 810, 120
Ciambur B. C., 2016, Publ. Astron. Soc. Austr., 33, e062
Ciambur B. C., Graham A. W., 2016, MNRAS, 459, 1276
Ciambur B. C., Graham A. W., Bland-Hawthorn J., 2017, MNRAS, 471, 3988
Coccato L., Morelli L., Pizzella A., Corsini E. M., Buson L. M., Dalla Bontà E., 2013, A&A, 549, A3
Colless M., 1999, Phil. Trans. R. Soc. A, 357, 105
Combes F., Sanders R. H., 1981, A&A, 96, 164
Combes F., Debbasch F., Friedli D., Pfenniger D., 1990, A&A, 233, 82
Comerón S. et al., 2014, A&A, 562, A121
Conroy C., van Dokkum P., 2012a, ApJ, 747, 69
Conroy C., van Dokkum P. G., 2012b, ApJ, 760, 71
Conselice C. J. et al., 2007, MNRAS, 381, 962
Costantin L. et al., 2020, ApJ, 889, L3
D'Onofrio M., 2001, MNRAS, 326, 1517
D'Onofrio M., Zaggia S. R., Longo G., Caon N., Capaccioli M., 1995, A&A, 296, 319
da Cunha E., Charlot S., Elbaz D., 2008, MNRAS, 388, 1595
da Cunha E., Charlot S., Dunne L., Smith D., Rowlands K., 2012, in Tuffs R. J., Popescu C. C., eds, The Spectral Energy Distribution of Galaxies - SED 2011, Vol. 284. Cambridge Univ. Press, Cambridge, p. 292
Daddi E. et al., 2005, ApJ, 626, 680
Damjanov I. et al., 2009, ApJ, 695, 101
Damjanov I. et al., 2011, ApJ, 739, L44
Damjanov I., Chilingarian I., Hwang H. S., Geller M. J., 2013, ApJ, 775, L48
Damjanov I., Hwang H. S., Geller M. J., Chilingarian I., 2014, ApJ, 793, 39
Damjanov I., Geller M. J., Zahid H. J., Hwang H. S., 2015a, ApJ, 806, 158
Damjanov I., Zahid H. J., Geller M. J., Hwang H. S., 2015b, ApJ, 815, 104
Davies R. L., Birkinshaw M., 1986, ApJ, 303, L45
Davies R. L., Birkinshaw M., 1988, ApJS, 68, 409
Davies R. L., Efstathiou G., Fall S. M., Illingworth G., Schechter P. L., 1983, ApJ, 266, 41
Davis T. A. et al., 2011, MNRAS, 417, 882
Davis B. L., Graham A. W., Cameron E., 2019, ApJ, 873, 85
de Grijs R., Kregel M., Wesson K. H., 2001, MNRAS, 324, 1074
de la Rosa I. G., La Barbera F., Ferreras I., Sánchez Almeida J., Dalla Vecchia C., Martínez-Valpuesta I., Stringer M., 2016, MNRAS, 457, 1916
de Souza R. E., Gadotti D. A., dos Anjos S., 2004, ApJS, 153, 411
de Vaucouleurs G., 1948, Ann. Astrophys., 11, 247
de Vaucouleurs G., 1959, ApJ, 130, 728
de Vaucouleurs G., de Vaucouleurs A., Corwin, Herold G. J., Buta R. J., Paturel G., Fouque P., 1991, Third Reference Catalogue of Bright Galaxies. Springer, New York, NY, USA
De T., Chattopadhyay T., Chattopadhyay A. K., 2014, Publ. Astron. Soc. Austr., 31, e047
Díaz-García S., Salo H., Laurikainen E., Herrera-Endoqui M., 2016, A&A, 587, A160
Djorgovski S., Davis M., 1987, ApJ, 313, 59
Domínguez Sánchez H., Bernardi M., Brownstein J. R., Drory N., Sheth R. K., 2019, MNRAS, 489, 5612
Dressler A., 1980, ApJS, 42, 565
Driver S. P., Popescu C. C., Tuffs R. J., Liske J., Graham A. W., Allen P. D., de Propris R., 2007a, MNRAS, 379, 1022
Driver S. P., Allen P. D., Liske J., Graham A. W., 2007b, ApJ, 657, L85
Driver S. P., Popescu C. C., Tuffs R. J., Graham A. W., Liske J., Baldry I., 2008, ApJ, 678, L101
Driver S. P., Robotham A. S. G., Bland-Hawthorn J., Brown M., Hopkins A., Liske J., Phillipps S., Wilkins S., 2013, MNRAS, 430, 2622
Drory N., Feulner G., Bender R., Botzler C. S., Hopp U., Maraston C., Mendes de Oliveira C., Snigula J., 2001, MNRAS, 325, 550
Dullo B. T., 2019, ApJ, 886, 80
Dullo B. T., Graham A. W., 2013, ApJ, 768, 36
Dutton A. A., Mendel J. T., Simard L., 2012, MNRAS, 422, L33

Dutton A. A., Macciò A. V., Mendel J. T., Simard L., 2013, MNRAS, 432, 2496
Efstathiou G., Ellis R. S., Carter D., 1980, MNRAS, 193, 931
Eisenhauer F. et al., 2011, The Messenger, 143, 16
Elmegreen B. G., Bournaud F., Elmegreen D. M., 2008, ApJ, 688, 67
Emsellem E. et al., 2007, MNRAS, 379, 401
Emsellem E. et al., 2011, MNRAS, 414, 888
Erwin P., 2005, MNRAS, 364, 283
Erwin P., 2015, ApJ, 799, 226
Erwin P., Debattista V. P., 2013, MNRAS, 431, 3060
Erwin P., Sparke L. S., 2002, AJ, 124, 65
Erwin P., Beltrán J. C. V., Graham A. W., Beckman J. E., 2003, ApJ, 597, 929
Erwin P., Beckman J. E., Pohlen M., 2005, ApJ, 626, L81
Erwin P., Pohlen M., Beckman J. E., 2008, AJ, 135, 20
Faber S. M., Wegner G., Burstein D., Davies R. L., Dressler A., Lynden-Bell D., Terlevich R. J., 1989, ApJS, 69, 763
Faber S. M. et al., 1997, AJ, 114, 1771
Fabricius M. H. et al., 2014, MNRAS, 441, 2212
Falcón-Barroso J., Peletier R. F., Vazdekis A., Balcells M., 2003, ApJ, 588, L17
Fan L., Lapi A., De Zotti G., Danese L., 2008, ApJ, 689, L101
Fang G.-W., Ma Z.-Y., Chen Y., Kong X., 2015, Res. Astron. Astrophys., 15, 819
Fasano G. et al., 2006, A&A, 445, 805
Ferré-Mateu A., Vazdekis A., Trujillo I., Sánchez-Blázquez P., Ricciardelli E., de la Rosa I. G., 2012, MNRAS, 423, 632
Ferré-Mateu A., Vazdekis A., de la Rosa I. G., 2013, MNRAS, 431, 440
Ferré-Mateu A., Trujillo I., Martín-Navarro I., Vazdekis A., Mezcua M., Balcells M., Domínguez L., 2017, MNRAS, 467, 1929
Ferreras I., La Barbera F., de La Rosa I. G., Vazdekis A., de Carvalho R. R., Falcon-Barroso J., Ricciardelli E., 2013, MNRAS, 429, L15
Ferrers N., 1877, Quart. J Pure Appl. Math, 14, 1
Fisher K. B., Huchra J. P., Strauss M. A., Davis M., Yahil A., Schlegel D., 1995, ApJS, 100, 69
Flynn C., Holmberg J., Portinari L., Fuchs B., Jahreiß H., 2006, MNRAS, 372, 1149
Font J. et al., 2017, ApJ, 835, 279
Font J., Beckman J. E., James P. A., Patsis P. A., 2019, MNRAS, 482, 5362
Förster Schreiber N. M. et al., 2009, ApJ, 706, 1364
Franx M., Illingworth G., Heckman T., 1989a, AJ, 98, 538
Franx M., Illingworth G., Heckman T., 1989b, ApJ, 344, 613
Fukugita M., Ichikawa T., Gunn J. E., Doi M., Shimasaku K., Schneider D. P., 1996, AJ, 111, 1748
Gadotti D. A., 2009, MNRAS, 393, 1531
Gallazzi A., Bell E. F., 2009, ApJS, 185, 253
Gargiulo A., Saracco P., Longhetti M., La Barbera F., Tamburri S., 2012, MNRAS, 425, 2698
Giavalisco M. et al., 2004, ApJ, 600, L93
Gillessen S. et al., 2010, in Danchi W. C., Delplancke F., Rajagopal J. K., eds, Proc. SPIE Conf. Ser. Vol. 7734, Optical and Infrared Interferometry II. SPIE, Bellingham, p. 77340Y
Giovanelli R. et al., 2005, AJ, 130, 2598
Gorbachev V. I., 1970, Sov. Astron., 14, 182
Graham A. W., 2001, AJ, 121, 820
Graham A. W., 2013, in Oswalt T. D., Keel W. C., eds, Elliptical and Disc Galaxy Structure and Modern Scaling Laws, Vol. 6. Springer Science + Business Media, Dordrecht, p. 91
Graham A., 2015, Highlights Astron., 16, 360
Graham A. W., 2019, MNRAS, 487, 4995
Graham A. W., Driver S. P., 2005, Publ. Astron. Soc. Aust., 22, 118
Graham A. W., Worley C. C., 2008, MNRAS, 388, 1708
Graham A. W., Colless M. M., Busarello G., Zaggia S., Longo G., 1998, A&AS, 133, 325
Graham A. W., Erwin P., Trujillo I., Asensio Ramos A., 2003a, AJ, 125, 2951
Graham A. W., Jerjen H., Guzmán R., 2003b, AJ, 126, 1787
Graham A. W., Onken C. A., Athanassoula E., Combes F., 2011, MNRAS, 412, 2211
Graham A. W., Dullo B. T., Savorgnan G. A. D., 2015, ApJ, 804, 32
Graham A. W., Durré M., Savorgnan G. A. D., Medling A. M., Batcheldor D., Scott N., Watson B., Marconi A., 2016a, ApJ, 819, 43
Graham A. W., Ciambur B. C., Savorgnan G. A. D., 2016b, ApJ, 831, 132
Graham A. W., Janz J., Penny S. J., Chilingarian I. V., Ciambur B. C., Forbes D. A., Davies R. L., 2017, ApJ, 840, 68
Graziani R., Courtois H. M., Lavaux G., Hoffman Y., Tully R. B., Copin Y., Pomarède D., 2019, MNRAS, 488, 5438
Grogin N. A. et al., 2011, ApJS, 197, 35
Gutiérrez L., Erwin P., Aladro R., Beckman J. E., 2011, AJ, 142, 145
Harris C. R. et al., 2020, Nature, 585, 357
Helou G., Madore B. F., Schmitz M., Bicay M. D., Wu X., Bennett J., 1991, in Albrecht M. A., Egret D., eds, The NASA/IPAC Extragalactic Database. Springer, Dordrecht, p. 89
Ho L. C., Li Z.-Y., Barth A. J., Seigar M. S., Peng C. Y., 2011, ApJS, 197, 21
Hohl F., 1975, in Hayli A., ed., Proc. IAU Symp. 69, Dynamics of the Solar Systems. D. Reidel Pub. Co., Dordrecht, Boston, p. 349
Hopkins P. F., Bundy K., Murray N., Quataert E., Lauer T. R., Ma C.-P., 2009, MNRAS, 398, 898
Hopkins P. F., Bundy K., Hernquist L., Wuyts S., Cox T. J., 2010, MNRAS, 401, 1099
Huang S., Ho L. C., Peng C. Y., Li Z.-Y., Barth A. J., 2013, ApJ, 766, 47
Huang X. et al., 2017, ApJ, 836, 157
Hubble E. P., 1926a, ApJ, 64, 321
Hubble E., 1926b, Contrib. Mount Wilson Obs. / Carnegie Instit. Washington, 324, 1
Hubble E. P., 1927, The Observatory, 50, 276
Hubble E. P., 1936, Realm of the Nebulae, Mrs. Hepsa Ely Silliman memorial lectures. Yale Univ. Press, London
Huchra J., Davis M., Latham D., Tonry J., 1983, ApJS, 52, 89
Hunter J. D., 2007, Comput. Sci. Eng., 9, 90
Hyde J. B., Bernardi M., 2009, MNRAS, 396, 1171
Into T., Portinari L., 2013, MNRAS, 430, 2715
Iodice E., D'Onofrio M., Capaccioli M., 1999, in Giuricin G., Mezzetti M., Salucci P., eds, ASP Conf. Ser. Vol. 176, Observational Cosmology: The Development of Galaxy Systems. Astron. Soc. Pac., San Francisco, p. 402
Jablonka P., Gorgas J., Goudfrooij P., 2007, A&A, 474, 763
Jeans J. H., 1919, Problems of Cosmogony and Stellar Dynamics. Cambridge Univ. Press, Cambridge
Jedrzejewski R. I., 1987, MNRAS, 226, 747
Jedrzejewski R., Schechter P. L., 1989, AJ, 98, 147
Jones D. H. et al., 2004, MNRAS, 355, 747
Joye W. A., Mandel E., 2003, in Payne H. E., Jedrzejewski R. I., Hook R. N., eds, ASP Conf. Ser. Vol. 295, Astronomical Data Analysis Software and Systems XII. Astron. Soc. Pac., San Francisco, p. 489
Kacprzak G. G., Churchill C. W., Ceverino D., Steidel C. C., Klypin A., Murphy M. T., 2010, ApJ, 711, 533
Kacprzak G. G., Muzahid S., Churchill C. W., Nielsen N. M., Charlton J. C., 2015, ApJ, 815, 22
Kanbur S. M., Ngeow C., Nikolaev S., Tanvir N. R., Hendry M. A., 2003, A&A, 411, 361
Kauffmann G. et al., 2003, MNRAS, 341, 33
Kaviraj S. et al., 2007, ApJS, 173, 619
Kaviraj S. et al., 2012, MNRAS, 423, 49
Kelvin L. S. et al., 2012, MNRAS, 421, 1007
Kennedy R. et al., 2016, MNRAS, 460, 3458
Khosroshahi H. G., Wadadekar Y., Kembhavi A., 2000, ApJ, 533, 162
Kim S. et al., 2014a, ApJS, 215, 22
Kim T. et al., 2014b, ApJ, 782, 64
King I. R., 1978, ApJ, 222, 1
Koekemoer A. M. et al., 2011, ApJS, 197, 36
Kormendy J., Fisher D. B., Cornell M. E., Bender R., 2009, ApJS, 182, 216
Kourkchi E., Courtois H. M., Graziani R., Hoffman Y., Pomarède D., Shaya E. J., Tully R. B., 2020, AJ, 159, 67
Krajnović D., Cappellari M., de Zeeuw P. T., Copin Y., 2006, MNRAS, 366, 787
Krajnović D. et al., 2008, MNRAS, 390, 93

Krajnović D. et al., 2011, MNRAS, 414, 2923
Krajnović D. et al., 2013a, MNRAS, 432, 1768
Krajnović D. et al., 2013b, MNRAS, 433, 2812
Kriek M., van der Wel A., van Dokkum P. G., Franx M., Illingworth G. D., 2008, ApJ, 682, 896
Kriek M., van Dokkum P. G., Labbé I., Franx M., Illingworth G. D., Marchesini D., Quadri R. F., 2009, ApJ, 700, 221
Kroupa P., 1998, in Rebolo R., Martin E. L., Zapatero Osorio M. R., eds, ASP Conf. Ser. Vol. 134, Brown Dwarfs and Extrasolar Planets. Astron. Soc. Pac., San Francisco, p. 483
Kroupa P., 2001, MNRAS, 322, 231
Kroupa P., 2002, Science, 295, 82
Kroupa P., Weidner C., Pflamm-Altenburg J., Thies I., Dabr inghausen J., Marks M., Maschberger T., 2013, in Oswalt T. D., Gilmore G., eds, Planets, Stars and Stellar Systems, Vol. 5: Galactic Structure and Stellar Populations. Springer, Berlin, p. 115
La Barbera F., de Carvalho R. R., de La Rosa I. G., Lopes P. A. A., Kohl-Moreira J. L., Capelato H. V., 2010, MNRAS, 408, 1313
La Barbera F., Ferreras I., Vazdekis A., de la Rosa I. G., de Carvalho R. R., Trevisan M., Falcón-Barroso J., Ricciardelli E., 2013, MNRAS, 433, 3017
Laine S., Shlosman I., Knapen J. H., Peletier R. F., 2002, ApJ, 567, 97
Läsker R., Ferrarese L., van de Ven G., 2014, ApJ, 780, 69
Lauer T. R. et al., 1995, AJ, 110, 2622
Lauer T. R. et al., 2005, AJ, 129, 2138
Lauer T. R. et al., 2007, ApJ, 664, 226
Laurikainen E., Salo H., Buta R., 2005, MNRAS, 362, 1319
Laurikainen E., Salo H., Buta R., Knapen J. H., Comerón S., 2010, MNRAS, 405, 1089
Le Bouquin J. B. et al., 2011, A&A, 535, A67
Leauthaud A. et al., 2007, ApJS, 172, 219
Liller M. H., 1966, ApJ, 146, 28
Liu M. C., Graham J. R., 2001, ApJ, 557, L31
Longhetti M. et al., 2007, MNRAS, 374, 614
López-Sanjuan C. et al., 2012, A&A, 548, A7
Lotz J. M., Jonsson P., Cox T. J., Primack J. R., 2008, MNRAS, 391, 1137
Lundmark K., 1925, MNRAS, 85, 865
Lupton R., Gunn J. E., Ivezić Z., Knapp G. R., Kent S., 2001, in Harnden F. R. J., Primini F. A., Payne H. E., eds, ASP Conf. Ser. Vol. 238, Astronomical Data Analysis Software and Systems X. Astron. Soc. Pac., San Francisco, p. 269
MacArthur L. A., Ellis R. S., Treu T. U V., Bundy K., Moran S., 2008, ApJ, 680, 70
MacArthur L. A., González J. J., Courteau S., 2009, MNRAS, 395, 28
Ma C.-P., Greene J. E., McConnell N., Janish R., Blakeslee J. P., Thomas J., Murphy J. D., 2014, ApJ, 795, 158
Man A. W. S., Zirm A. W., Toft S., 2016, ApJ, 830, 89
Mancini C. et al., 2010, MNRAS, 401, 933
Mandel K. S., Narayan G., Kirshner R. P., 2011, ApJ, 731, 120
Maraston C., 1998, MNRAS, 300, 872
Maraston C., 2005, MNRAS, 362, 799
Marian V., Ziegler B., Kuchner U., Verdugo M., 2018, A&A, 617, A34
Marigo P., Girardi L., Bressan A., Groenewegen M. A. T., Silva L., Granato G. L., 2008, A&A, 482, 883
Martin P., 1995, AJ, 109, 2428
Martin D. C. et al., 2019, Nat. Astron., 3, 822
Martín-Navarro I., La Barbera F., Vazdekis A., Ferré-Mateu A., Trujillo I., Beasley M. A., 2015, MNRAS, 451, 1081
Martinez-Manso J. et al., 2011, ApJ, 738, L22
Martinez-Valpuesta I., Knapen J. H., Buta R., 2007, AJ, 134, 1863
McDermid R. et al., 2020, Phase A Science Case for MAVIS – The Multi-conjugate Adaptive-optics Visible Imager-Spectrograph for the VLT Adaptive Optics Facility. Macquarie University, Sydney
McDonald M., Courteau S., Tully R. B., Roediger J., 2011, MNRAS, 414, 2055
McLure R. J. et al., 2013, MNRAS, 428, 1088
Mei S. et al., 2007, ApJ, 655, 144
Mendel J. T., Simard L., Palmer M., Ellison S. L., Patton D. R., 2014, ApJS, 210, 3
Méndez-Abreu J. et al., 2017, A&A, 598, A32
Michard R., 1984, A&A, 140, L39
Miller R. H., 1978, ApJ, 223, 122
Möllenhoff C., Heidt J., 2001, A&A, 368, 16
Moorthy B. K., Holtzman J. A., 2006, MNRAS, 371, 583
Moraes B. et al., 2014, Rev. Mex. Astron. Astrofis. Ser. Conf., 44, 202
Mould J. R. et al., 2000, ApJ, 529, 786
Naab T., Johansson P. H., Ostriker J. P., 2009, ApJ, 699, L178
Navarro J. F., Benz W., 1991, ApJ, 380, 320
Nelson E. J. et al., 2012, ApJ, 747, L28
Newman A. B., Ellis R. S., Bundy K., Treu T., 2012, ApJ, 746, 162
Nielsen N. M., Kacprzak G. G., Muzahid S., Churchill C. W., Murphy M. T., Charlton J. C., 2017, ApJ, 834, 148
Nieto J. L., Roques S., Llebaria A., Vand erriest C., Lelievre G., di Serego Alighieri S., Macchetto F. D., Perryman M. A. C., 1988, ApJ, 325, 644
Norman C. A., Sellwood J. A., Hasan H., 1996, ApJ, 462, 114
Oke J. B., 1974, ApJS, 27, 21
Oldham L. et al., 2017, MNRAS, 465, 3185
Oogi T., Habe A., 2013, MNRAS, 428, 641
Patterson F. S., 1940, Harvard Coll. Obs. Bullet., 914, 9
Peebles P. J. E., 1989, ApJ, 344, L53
Peebles P. J. E., 2001, ApJ, 557, 495
Peletier R. F., Balcells M., 1996, AJ, 111, 2238
Peletier R. F., Davies R. L., Illingworth G. D., Davis L. E., Cawson M., 1990, AJ, 100, 1091
Peletier R. F., Balcells M., Davies R. L., Andredakis Y., Vazdekis A., Burkert A., Prada F., 1999, MNRAS, 310, 703
Peletier R. F. et al., 2007, MNRAS, 379, 445
Peletier R. F. et al., 2012, MNRAS, 419, 2031
Peng C. Y., Ho L. C., Impey C. D., Rix H.-W., 2002, AJ, 124, 266
Peng C. Y., Ho L. C., Impey C. D., Rix H.-W., 2010, AJ, 139, 2097
Pérez-González P. G., Trujillo I., Barro G., Gallego J., Zamorano J., Conselice C. J., 2008, ApJ, 687, 50
Peterson C. J., 1978, ApJ, 222, 84
Pforr J., Maraston C., Tonini C., 2012, MNRAS, 422, 3285
Phelps S. D., Desjacques V., Nusser A., Shaya E. J., 2006, MNRAS, 370, 1361
Poggianti B. M. et al., 2013a, ApJ, 762, 77
Poggianti B. M., Moretti A., Calvi R., D'Onofrio M., Valentinuzzi T., Fritz J., Renzini A., 2013b, ApJ, 777, 125
Poggianti B. M. et al., 2016, in Napolitano N. R., Longo G., Marconi M., Paolillo M., Iodice E., eds, The Universe of Digital Sky Surveys, Vol. 42. Springer, Berlin, p. 177
Pohlen M., Dettmar R. J., Lütticke R., Aronica G., 2002, A&A, 392, 807
Pohlen M., Beckman J. E., Hüttemeister S., Knapen J. H., Erwin P., Dettmar R. J., 2004, in Block D. L., Puerari I., Freeman K. C., Groess R., Block E. K., eds, Astrophysics and Space Science Library, Vol. 319, Penetrating Bars Through Masks of Cosmic Dust. Kluwer Academic Publishers, Dordrecht, p. 713
Poincare H., Vergne H., 1911, Lecons sur les hypotheses cosmogoniques professees a la Sorbonne, Landmarks of Science. A. Hermann et fils, Paris
Poveda A., 1958, Bol. Obs. Tonantzintla Tacubaya, 2, 3
Poveda A., 1961, ApJ, 134, 910
Prieto M., Gottesman S. T., Aguerri J.-A. L., Varela A.-M., 1997, AJ, 114, 1413
Prochaska J. X., Weiner B., Chen H. W., Mulchaey J., Cooksey K., 2011, ApJ, 740, 91
Proctor R. N., Sansom A. E., 2002, MNRAS, 333, 517
Quillen A. C., Bower G. A., Stritzinger M., 2000, ApJS, 128, 85
Ragone-Figueroa C., Granato G. L., 2011, MNRAS, 414, 3690
Ravindranath S., Ho L. C., Peng C. Y., Filippenko A. V., Sargent W. L. W., 2001, AJ, 122, 653
Rest A., van den Bosch F. C., Jaffe W., Tran H., Tsvetanov Z., Ford H. C., Davies J., Schafer J., 2001, AJ, 121, 2431

Ricciardelli E., Vazdekis A., Cenarro A. J., Falcón-Barroso J., 2012, MNRAS, 424, 172
Rigaut F. et al., 2020, in Evans C. J., Bryant J. J., Motohara K., eds, Proc. SPIE Conf. Ser. Vol. 11447, Ground-based and Airborne Instrumentation for Astronomy VIII. SPIE, Bellingham, p. 114471R
Roediger J. C., Courteau S., 2015, MNRAS, 452, 3209
Ruiz-Lapuente P., 1996, ApJ, 465, L83
Saglia R. P. et al., 2010, A&A, 524, A6
Saha A., Thim F., Tammann G. A., Reindl B., Sand age A., 2006, ApJS, 165, 108
Saha K., Graham A. W., Rodríguez-Herranz I., 2018, ApJ, 852, 133
Sahu N., Graham A. W., Davis B. L., 2019, ApJ, 876, 155
Salimbeni S., Fontana A., Giallongo E., Grazian A., Menci N., Pentericci L., Santini P., 2009, in Giobbi G., Tornambe A., Raimondo G., Limongi M., Antonelli L. A., Menci N., Brocato E., eds, AIP Conf. Proc. Vol. 1111, Probing Stellar Populations Out to the Distant Universe: Cefalu 2008, Proceedings of the International Conference. Am. Inst. Phys., New York, p. 207
Salo H. et al., 2015, ApJS, 219, 4
Salpeter E. E., 1955, ApJ, 121, 161
Sánchez S. F. et al., 2016, A&A, 594, A36
Sandage A., Binggeli B., Tammann G. A., 1985, AJ, 90, 395
Saracco P., Longhetti M., Andreon S., 2009, MNRAS, 392, 718
Saracco P., Longhetti M., Gargiulo A., 2010, MNRAS, 408, L21
Saulder C., van den Bosch R. C. E., Mieske S., 2015, A&A, 578, A134
Savorgnan G. A. D., Graham A. W., 2016a, ApJS, 222, 10
Savorgnan G. A. D., Graham A. W., 2016b, MNRAS, 457, 320
Scarlata C. et al., 2007, ApJS, 172, 406
Schechter P. L., Gunn J. E., 1979, ApJ, 229, 472
Schlegel D. J., Finkbeiner D. P., Davis M., 1997, American Astronomical Society Meeting Abstracts, 87.04
Schombert J., McGaugh S., Lelli F., 2019, MNRAS, 483, 1496
Schombert J., McGaugh S., Lelli F., 2022, AJ, 163, 154
Scognamiglio D. et al., 2020, ApJ, 893, 4
Scott N. et al., 2015, MNRAS, 451, 2723
Scoville N. et al., 2007, ApJS, 172, 1
Seigar M. S., James P. A., 1998, MNRAS, 299, 672
Sellwood J. A., Wilkinson A., 1993, Rep. Prog. Phys., 56, 173
Sérsic J. L., 1968, Atlas de Galaxias Australes. Cordoba Observatorio Astronomico, Cordoba, Argentina
Shaya E. J., Tully R. B., 2013, MNRAS, 436, 2096
Shaya E. J., Tully R. B., Hoffman Y., Pomarède D., 2017, ApJ, 850, 207
Silverman J. M. et al., 2012, MNRAS, 425, 1789
Simard L., 1998, in Albrecht R., Hook R. N., Bushouse H. A., eds, ASP Conf. Ser. Vol. 145, Astronomical Data Analysis Software and Systems VII. Astron. Soc. Pac., San Francisco, p. 108
Simard L. et al., 2002, ApJS, 142, 1
Simard L., Mendel J. T., Patton D. R., Ellison S. L., McConnachie A. W., 2011, ApJS, 196, 11
Simien F., Prugniel P., 2002, A&A, 384, 371
Smith R. J., 2014, MNRAS, 443, L69
Spiniello C., Trager S. C., Koopmans L. V. E., Chen Y. P., 2012, ApJ, 753, L32
Spiniello C., Trager S., Koopmans L. V. E., Conroy C., 2014, MNRAS, 438, 1483
Spiniello C. et al., 2021, A&A, 654, A136
Steinmetz M., Navarro J. F., 2002, New Astron., 7, 155
Stewart K. R., Brooks A. M., Bullock J. S., Maller A. H., Diemand J., Wadsley J., Moustakas L. A., 2013, ApJ, 769, 74
Stocke J. T., Keeney B. A., Danforth C. W., Shull J. M., Froning C. S., Green J. C., Penton S. V., Savage B. D., 2013, ApJ, 763, 148
Stone C. J., Arora N., Courteau S., Cuillandre J.-C., 2021, MNRAS, 508, 1870
Stoughton C. et al., 2002, AJ, 123, 485
Strateva I. V. et al., 2003, AJ, 126, 1720
Strauss M. A. et al., 2002, AJ, 124, 1810
Szomoru D., Franx M., Bouwens R. J., van Dokkum P. G., Labbé I., Illingworth G. D., Trenti M., 2011, ApJ, 735, L22
Tal T., van Dokkum P. G., Nelan J., Bezanson R., 2009, AJ, 138, 1417
Taylor M. B., 2005, in Shopbell P., Britton M., Ebert R., eds, ASP Conf. Ser. Vol. 347, Astronomical Data Analysis Software and Systems XIV. Astron. Soc. Pac., San Francisco, p. 29
Taylor E. N., Franx M., Glazebrook K., Brinchmann J., van der Wel A., van Dokkum P. G., 2010, ApJ, 720, 723
Taylor E. N. et al., 2011, MNRAS, 418, 1587
Thom C., Werk J. K., Tumlinson J., Prochaska J. X., Meiring J. D., Tripp T. M., Sembach K. R., 2011, ApJ, 736, 1
Thomas D., Davies R. L., 2006, MNRAS, 366, 510
Tody D., 1986, in Crawford D. L., ed., Proc. SPIE Conf. Ser. Vol. 627, Instrumentation in Astronomy VI. SPIE, Bellingham, p. 733
Tody D., 1993, in Hanisch R. J., Brissenden R. J. V., Barnes J., eds, ASP Conf. Ser. Vol. 52, Astronomical Data Analysis Software and Systems II. Astron. Soc. Pac., San Francisco, p. 173
Tonry J. L., Dressler A., Blakeslee J. P., Ajhar E. A., Fletcher A. B., Luppino G. A., Metzger M. R., Moore C. B., 2001, ApJ, 546, 681
Tortora C. et al., 2016, in Napolitano N. R., Longo G., Marconi M., Paolillo M., Iodice E., eds, The Universe of Digital Sky Surveys, Vol. 42. Springer, Berlin, p. 123
Tortora C. et al., 2018, MNRAS, 481, 4728
Tortora C. et al., 2020, A&A, 638, L11
Tran H. D., Tsvetanov Z., Ford H. C., Davies J., Jaffe W., van den Bosch F. C., Rest A., 2001, AJ, 121, 2928
Trujillo I., Erwin P., Asensio Ramos A., Graham A. W., 2004, AJ, 127, 1917
Trujillo I. et al., 2006, MNRAS, 373, L36
Trujillo I., Conselice C. J., Bundy K., Cooper M. C., Eisenhardt P., Ellis R. S., 2007, MNRAS, 382, 109
Trujillo I., Cenarro A. J., de Lorenzo-Cáceres A., Vazdekis A., de la Rosa I. G., Cava A., 2009, ApJ, 692, L118
Trujillo I., Ferreras I., de La Rosa I. G., 2011, MNRAS, 415, 3903
Trujillo I., Ferré-Mateu A., Balcells M., Vazdekis A., Sánchez-Blázquez P., 2014, ApJ, 780, L20
Tukey J., 1977, Exploratory Data Analysis, Addison-Wesley series in behavioral science No. v. 2. Addison-Wesley Publishing Company, Boston
Tully R. B., Fisher J. R., 1977, A&A, 500, 105
Tully R. B., Verheijen M. A. W., 1997, ApJ, 484, 145
Tully R. B., Shaya E. J., Karachentsev I. D., Courtois H. M., Kocevski D. D., Rizzi L., Peel A., 2008, ApJ, 676, 184
Tully R. B. et al., 2013, AJ, 146, 86
Tully R. B., Courtois H., Hoffman Y., Pomarède D., 2014, Nature, 513, 71
Tumlinson J. et al., 2013, ApJ, 777, 59
Valentinuzzi T. et al., 2010, ApJ, 712, 226
van de Sande J. et al., 2013, ApJ, 771, 85
van den Bergh S., 1990, ApJ, 348, 57
van den Bosch R. C. E., Gebhardt K., Gültekin K., van de Ven G., van der Wel A., Walsh J. L., 2012, Nature, 491, 729
van der Kruit P. C., 1987, A&A, 173, 59
van der Kruit P. C., Searle L., 1981, A&A, 95, 116
van der Marel R. P., Binney J., Davies R. L., 1990, MNRAS, 245, 582
van der Velden E., 2020, J. Open Source Softw., 5, 2004
van der Wel A. et al., 2011, ApJ, 730, 38
van der Wel A. et al., 2014, ApJ, 788, 28
van Dokkum P. G., Conroy C., 2010, Nature, 468, 940
van Dokkum P. G., Conroy C., 2012, ApJ, 760, 70
van Dokkum P. G., Franx M., 1996, MNRAS, 281, 985
van Dokkum P. G. et al., 2008, ApJ, 677, L5
van Dokkum P. G. et al., 2015, ApJ, 813, 23
Vazdekis A., Cenarro A. J., Gorgas J., Cardiel N., Peletier R. F., 2003, MNRAS, 340, 1317
Vazdekis A., Ricciardelli E., Cenarro A. J., Rivero-González J. G., Díaz-García L. A., Falcón-Barroso J., 2012, MNRAS, 424, 157
Veale M., Ma C.-P., Greene J. E., Thomas J., Blakeslee J. P., McConnell N., Walsh J. L., Ito J., 2017, MNRAS, 471, 1428
Vika M., Driver S. P., Cameron E., Kelvin L., Robotham A., 2012, MNRAS, 419, 2264
Vika M., Bamford S. P., Häußler B., Rojas A. L., 2014, MNRAS, 444, 3603
Virtanen P. et al., 2020, Nat. Methods, 17, 261

Volonteri M., Ciotti L., 2013, ApJ, 768, 29
Vulcani B. et al., 2014, MNRAS, 441, 1340
Wakker B. P., Savage B. D., 2009, ApJS, 182, 378
Werner N., Lakhchaura K., Canning R. E. A., Gaspari M., Simionescu A., 2018, MNRAS, 477, 3886
West A. A. et al., 2010, AJ, 139, 315
West A. A., 2005, PhD thesis, University of Washington, Washington, USA
White S. D. M., Frenk C. S., 1991, ApJ, 379, 52
White S. D. M., Rees M. J., 1978, MNRAS, 183, 341
Willick J. A., Courteau S., Faber S. M., Burstein D., Dekel A., Strauss M. A., 1997, ApJS, 109, 333
Wuyts S. et al., 2007, ApJ, 655, 51
York D. G. et al., 2000, AJ, 120, 1579
Young L. M. et al., 2011, MNRAS, 414, 940
Zabl J. et al., 2019, MNRAS, 485, 1961
Zhu P., Ho L. C., Gao H., 2021, ApJ, 907, 6
Zibetti S., Charlot S., Rix H.-W., 2009, MNRAS, 400, 1181
Zwicky F., 1937, ApJ, 86, 217
Zwicky F., Kowal C. T., 1968, Catalogue of Galaxies and of Clusters of Galaxies, Volume VI. California Institute of Technology, Pasadena
Zwicky F., Zwicky M. A., 1971, Catalogue of Selected Compact Galaxies and of Post-Eruptive Galaxies. Guemligen, Switzerland

APPENDIX A: DISTANCE CORRECTION

The variation among the four different distance measurements that we explored turns out not to be significant in regard to the number density of compact massive spheroids. We show these distance measurements in the forest plot of Fig. A1. The W1997, M2000, *Cosmicflow-3* (Kourkchi et al. 2020), and z-independent distances are labelled in green, blue, purple, and orange points, respectively. The mean differences between each set of distances span 3.16 to 7.54 Mpc, while the standard deviations vary from 2.38 to 4.95 Mpc. The values and sources of the various z-independent distances are listed in Table A1.

Cosmicflow-3 has the most sophisticated model to date, and it was built from the largest observational data set among the three model-based choices. The main issue of *Cosmicflow-3* is the triple-value region, where the gravity of the Virgo Cluster is significant enough to bend the velocity–distance relation into a cubic equation. Galaxies residing within 7–21 Mpc, therefore, have two or three solutions (possible distances) for the same recessional velocity. In Fig. A1, we highlighted such objects with extended error bars (NGC 4374, NGC 4429, NGC 4459, NGC 4636, NGC 4643, NGC 4845, NGC 4649, and NGC 4772), in which the upper and lower limits represent the high and low estimation of the distance, respectively.

We used the redshift-independent distance as the primary distance to calculate the luminosity of the spheroids and galaxies in our sample. The only exceptions are NGC 4874 (an SBF distance), NGC 5440 (an SNIa distance), and NGC 4233 (an SBF distance), where all of them exhibit a large error (>10 Mpc). In these cases, we use the *Cosmicflow-3* value instead. In total, 19 galaxies' total and spheroidal stellar mass are obtained via z-independent distances. Other than these 19 galaxies, we primarily used the *Cosmicflow-3* distance, in total, for 81 galaxies. There are an additional three galaxies that are within the triple-value region but which do not have z-independent measurements: NGC 4845, NGC 4643, and NGC 4429. In all three cases, the W1997 distances lie within the triple-value region, with a reasonable agreement with the median value of the *Cosmicflow-3* distance. For these galaxies, we elect to use the W1997 distances, derived from empirical TF-relation, instead. The adopted distances for all 103 galaxies are provided in Table C1.

Table A1. Redshift-independent measurements.

Name	Distance (Mpc)	Method	Sources
		Bin 1	
NGC 4874	100.0 ± 10.0	SBF	Liu & Graham (2001)
		Bin 2	
NGC 5440	54.425 ± 12.718	SNIa	Silverman et al. (2012)
		Bin 3	
NGC 4649	16.827 ± 1.200	SBF	Tonry et al. (2001)
NGC 4636	14.655 ± 0.904	SBF	Tonry et al. (2001)
NGC 4374	18.510 ± 0.606	SBF	Blakeslee et al. (2009)
NGC 4261	31.623 ± 2.892	SBF	Tonry et al. (2001)
NGC 4772	16.6 ± 1.1	SNIa	Huang et al. (2017)
NGC 4579	21.0 ± 2.0	SNIa	Ruiz-Lapuente (1996)
NGC 4548	15.424 ± 0.564	Cepheids	Kanbur et al. (2003)
NGC 4536	15.567 ± 0.749	Cepheids	Kanbur et al. (2003)
NGC 4527	14.158 ± 0.867	Cepheids	Kanbur et al. (2003)
NGC 4526	16.904 ± 1.631	SBF	Tonry et al. (2001)
NGC 4494	17.061 ± 0.887	SBF	Tonry et al. (2001)
NGC 4459	16.069 ± 0.450	SBF	Mei et al. (2007)
NGC 4414	17.693 ± 0.362	Cepheids	Kanbur et al. (2003)
NGC 4382	17.881 ± 0.560	SBF	Blakeslee et al. (2009)
NGC 4233	33.884 ± 18.355	SBF	Tonry et al. (2001)
NGC 4168	30.903 ± 6.594	SBF	Tonry et al. (2001)
NGC 3414	25.235 ± 4.142	SBF	Tonry et al. (2001)
NGC 3368	11.695 ± 0.609	Cepheids	Saha et al. (2006)
NGC 3169	16.444 ± 0.617	SNIa	Mandel, Narayan & Kirshner (2011)
NGC 2962	34.041 ± 2.435	SBF	Ajhar et al. (2001)

Note. SNIa = Supernovae Type Ia
SBF = Surface Brightness Fluctuations

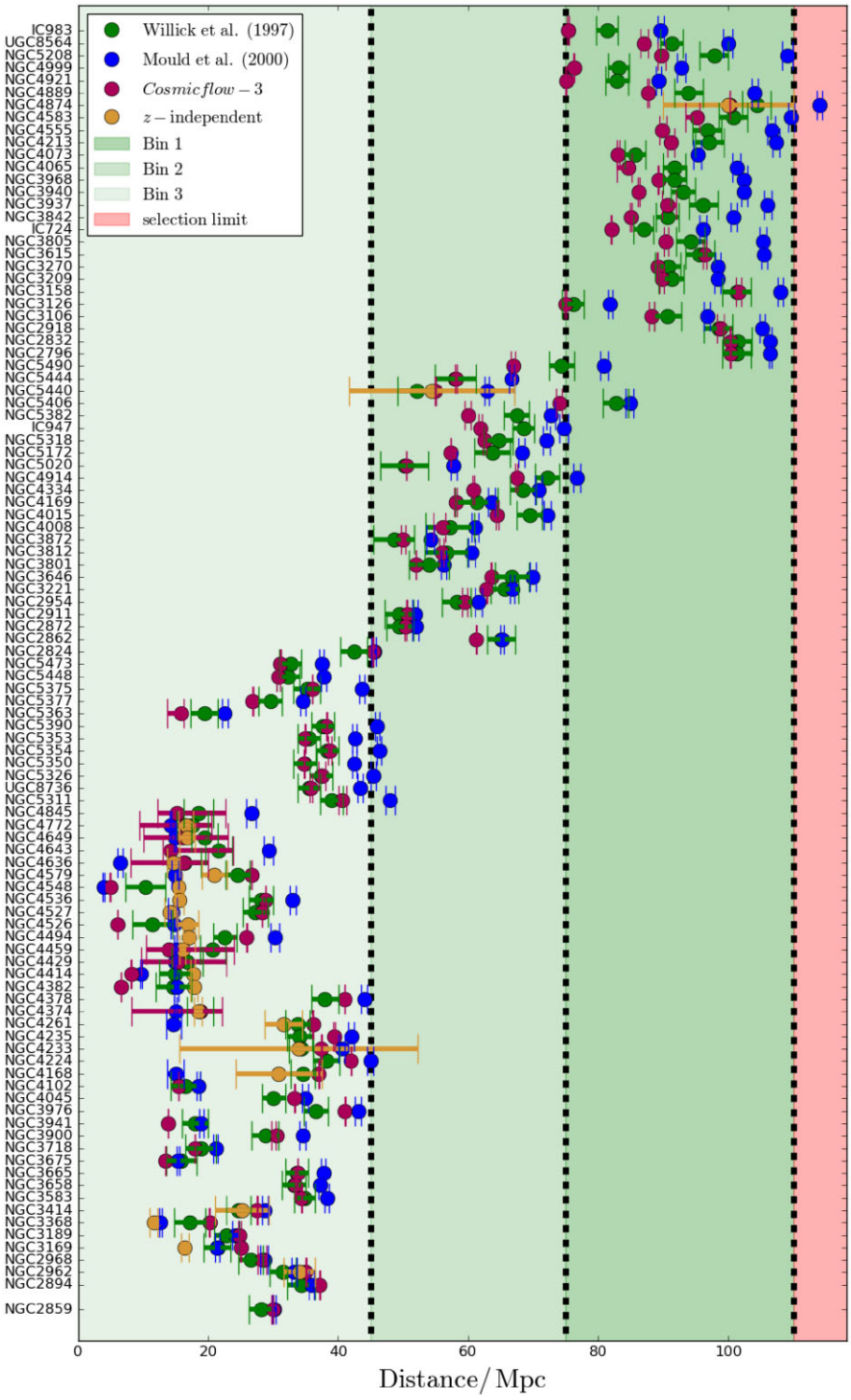

Figure A1. Distances using different models. The pink zone is the area outside of the selection volume. The purple points are the *Cosmicflow-3* (Kourkchi et al. 2020) distances, the blue points are the M2000 distances, and the green points are the W1997 distances. The orange points are a blanket label for the redshift-independent measurements from various sources; see Table A1. Galaxies are listed in descending (westward) order, according to right ascension. Note that several galaxies (NGC 5490, NGC 5406, NGC 4914, NGC 2824, NGC 5390, NGC 5354, NGC 5326, and NGC 5311) have their distances lie in different Bins. For those cases, we present the result in the Bins according to their *Cosmicflow-3* distance as in both Tables C1–C3 and D1–D3.

APPENDIX B: THE MASS-TO-LIGHT COLOUR RELATIONS

Here, we provide a supplementary description of possible error sources and the underlying assumptions that went into building the mass-to-light colour relations (MLCRs) presented in this work. This speaks directly to the stellar masses that we have derived.

Several key factors contribute to the error budget of the estimated stellar mass.

(i) The innate stellar population model degeneracy, between age and metallicity, is reported to constitute a small error of 0.1–0.2 dex from idealized mock galaxy studies (Gallazzi & Bell 2009).

(ii) A more prominent error comes from the systematic treatments of the 'priors'. The IMF provides the normalization factor for the MLCRs, and its uncertainty affects the M_*/L ratio. For example, there can be a change of up to 0.3 dex in mass if one assumes a Chabrier (2003) over a Salpeter (1955) IMF (RC15).

(iii) Another obvious factor is the stellar population model. The most widely used prescription is the BC03 Stellar Population Synthesis (SPS) model. It provides a comprehensive library of the stellar population that was validated by agreement with early data from the SDSS. Over the years, the community has been continuously updating the model by including previously unconsidered stellar isochrones. The most notable issue plaguing stellar population models is the influence of the thermally pulsating asymptotic giant branch (TP-AGB) stars. Multiple studies (e.g. Maraston 1998, 2005) have pointed out that the excess light from the young ($\sim$1 Gyr) TP-AGB star's emission can lead us to an underestimation of the M_*/L ratio. This effect is particularly relevant for near-infrared (NIR) studies, as the inclusion of TP-AGB stars (Bruzual 2007a, b) in the renewed version of the BC03 SPS model in 2007 (commonly known as the CB07 SPS in the literature, see the *MAGPHYS* da Cunha, Charlot & Elbaz 2008 library) results in M_*/L ratio changes of 0.1 and 0.4 dex in the optical and NIR, respectively (Z09).

(iv) Treatment of the interstellar medium (ISM) and dust attenuation also changes the perceived light. IP13 show the effect of omitting dust attenuation in their fig. 13. In a dusty scenario, the mass-to-light relation can change by up to 0.5 dex in the case of an inclined disc (see also Driver et al. 2007a, 2008).

Given the need to appreciate how the stellar masses of the high-z galaxies were obtained by different authors, we identify and briefly describe each MLCR they used.

(i) Z09 assumes the Chabrier (2003) IMF, the CB07 SPS, and the dust attenuation from Charlot & Fall (2000). The M_*/L ratio is produced using the fiducial mass reconstruction method by Monte Carlo sampling from the CB07 library, with parameters advised by Kauffmann et al. (2003). The M_*/L ratio is then mapped on to the colour space of $(g - i)$ and $(i - H)$ to build their MLCR shown in equation (3a). They verified this by comparing it to nine local galaxies within 30 Mpc.

(ii) Both T11 and RC15 used the Chabrier (2003) IMF and the BC03 SPS, which, as we have seen, has been the most commonly used assumption in the literature when calculating the stellar masses of high-z galaxies. Given the assumed dust attenuation law from Calzetti et al. (2000), T11 calculated the stellar mass by fitting the SED from early Galaxy And Mass Assembly (GAMA DR1) broad-band photometry data via Bayesian probability minimization. Among the above-mentioned MLCRs, T11 is the only one that is built empirically from the ground up. The GAMA data covers the intermediate-redshift range ($z < 0.65$; median $z = 0.2$) and magnitudes $r_{\rm petro} < 19.4$–19.8 mag. However, claim has been made that T11's MLCR underestimated the M/L ratio for early-type spirals and ellipticals (Schombert, McGaugh & Lelli 2022).

(iii) RC15 constructed their MLCR via mock galaxies using the *MAGPHYS* library (da Cunha et al. 2008). The mock galaxy SEDs undergo Bayesian fitting on *girzH* bands to recover the stellar masses. The MLCR yields excellent agreement with the observational SHIVir survey ('Spectroscopy and *H*-band imaging of Virgo Cluster galaxies'; McDonald et al. 2011) data, having mean residuals of -0.01 dex and 0.05 dex (see their fig. 6).
With the same IMF and SPS as T11, RC15 is different in several ways. First, RC15 assume a different dust treatment (Charlot & Fall 2000) with two-component models accounting for the dust in molecular clouds and the ambient ISM. Secondly, RC15 suggests that T11 did not include bursts in their model SFHs, while *MAGPHYS* contains random burst models superimposed in the SFH. Both works are validated by their respective observational data: one of which focuses on the nearby Virgo Cluster galaxies and the other on galaxies at intermediate redshifts. The considerable discrepancy between them (Fig. 2) might arise from the use of different data sets.

(iv) Finally, IP13 constructed their MLCR uniquely by choosing a Kroupa (1998) IMF and the Marigo et al. (2008) isochrone model (the same used in CB07). Once again, the choice of Marigo et al. (2008) isochrones stems from the concern over the TP-AGB influence. Their equation is constructed assuming a dust-free scenario. While the effect of dust is significant in some colour, they concluded that $(g - i)$ remains a good tracer for the galaxies' stellar masses. The consequence of using such a combination is the slower decline of stellar mass as a function of age (see their fig. 1) in comparison to the more popular BC03 SPS.

APPENDIX C: GALAXY DATA

Here, we present the basic information for the galaxy sample identified in Section 2.4. Tables C1–C3 also provide the new morphological classifications (Column 9) based on our multicomponent decomposition, as described in Section 3.3.

In Tables C1–C3, Column (8) lists the past morphology assignment while Column (9) provides our new classifications. The labels for the new classes are inspired by the 'morphology grid' from Graham (2019) for high surface brightness galaxies. It represents the progression from the traditional Hubble-Jeans sequence (Jeans 1919; Lundmark 1925; Hubble 1926a, b, 1927, 1936), with an emphasis on the commonly overlooked features in early-type galaxies, such as bars and the continua of disc sizes (nuclear, intermediate, and large-scale). The grid includes the ellicular (ES) class of galaxies (Liller 1966), denoting the spheroids with an embedded intermediate-scale disc, and it removes the redundant E4–E7 classes because they are essentially all lenticular galaxies (Liller 1966; Gorbachev 1970; Michard 1984; Capaccioli, Caon & Rampazzo 1990b; van den Bergh 1990). For simplicity's sake, we omit the subdivision of spiral arm shapes (a, b, c, d, and m) which are not as relevant to our investigation. We label the galaxies as ellipticals without a disc (E0–E3), elliculars (EAS or EBS), lenticulars (SA0, SAB0, or SB0), and spirals (SA, SAB, or SB), in which A and B are the distinctions between barless and barred galaxies, and AB is designated for weak bars, defined here as those with lower central surface brightness (μ_0) than the disc.

In accordance with the common practice in the literature, we performed a single Sérsic function fit to determine the effective radius ($R_{\rm e}$) for each galaxy. In Fig. C1, we show the distribution of $R_{\rm e}/R_{\rm max}$ for our galaxies, separated by their morphology. We choose the cutoff radius, $R_{\rm max}$, to fitting the light profile at the radius where the S/N ratio is low and no longer useful for decomposition. The majority

Table C1. Galaxy sample and basic data.

Name	RA	Dec	Dist.	$\mathfrak{m}_g$	$\mathfrak{m}_i$	Seeing	Morph.	Morph.	$\mathfrak{M}_i$	$M_{*,\mathrm{gal}}$	R_{max}
	deg	deg	Mpc	mag	mag	arcsec	(old)	(new)	mag	$10^{10}\,\mathrm{M}_\odot$	arcsec
(1)	(2)	(3)	(4)	(5)	(6)	(7)	(8)	(9)	(10)	(11)	(12)
Bin 1											
IC 983	212.5	17.7	89.6	12.3	11.1	0.8	SBbc	SB	−23.7	62.7	72.0
UGC 8564	203.7	38.5	100.0	13.4	11.9	0.8	S0	SA0	−23.1	59.9	50.0
NGC 5208	203.1	7.3	109.2	13.1	11.9	0.9	S0	SA0	−23.3	48.6	36.0
NGC 4999	197.4	1.7	92.8	11.9	10.8	0.9	Sb	SB	−24.1	81.3	50.0
NGC 4921	195.4	27.9	89.3	12.1	10.9	0.8	Sab	SAB	−23.9	81.4	68.0
NGC 4889	195.0	28.0	104.1	12.1	10.9	1.0	E	E3	−24.2	109.8	47.0
NGC 4874	194.9	28.0	99.5	12.7	11.5	1.1	E	SA0	−23.5	52.3	90.0
NGC 4583	189.5	33.5	109.7	13.6	12.2	1.4	S0	SA0	−23.0	60.1	34.0
NGC 4555	188.9	26.5	106.6	12.2	11.0	1.3	E	E2	−24.1	89.1	57.0
NGC 4213	183.9	24.0	107.3	12.6	11.4	0.9	E	SA0	−23.8	64.3	42.0
NGC 4073	181.1	1.9	95.3	12.5	11.3	1.0	E	E3	−23.6	60.7	68.0
NGC 4065	181.0	20.2	101.3	12.6	11.4	0.8	E	SA0	−23.6	54.3	27.0
NGC 3968	178.9	12.0	102.4	12.1	10.9	1.1	Sbc	SAB	−24.1	84.8	57.0
NGC 3940	178.2	21.0	102.5	12.9	11.6	1.5	E	SA0	−23.4	54.8	50.0
NGC 3937	178.2	20.6	106.1	12.2	11.0	1.0	S0	SA0	−24.1	80.1	69.0
NGC 3842	176.0	19.9	100.8	12.5	11.3	0.9	E	SA0	−23.7	63.1	62.0
IC 724	175.9	8.9	96.1	12.6	11.4	1.2	Sa	SA	−23.5	58.1	43.0
NGC 3805	175.2	20.3	105.3	12.9	11.6	0.9	S0	EAS	−23.5	63.3	64.0
NGC 3615	169.5	23.4	105.6	12.8	11.6	1.0	E	E3	−23.5	57.7	60.0
NGC 3270	157.9	24.9	98.4	12.8	11.5	1.3	SABb	SAB	−23.4	58.5	33.0
NGC 3209	155.2	25.5	98.4	12.4	11.2	1.0	E	SA0	−23.7	66.2	52.0
NGC 3158	153.5	38.8	108.0	12.7	11.5	1.3	E	SA0	−23.7	68.8	105.0
NGC 3126	152.1	31.9	81.9	12.7	11.4	1.1	SABb	SB0	−23.2	58.9	23.0
NGC 3106	151.0	31.2	96.7	12.4	11.2	1.4	S0	SA0	−23.7	60.9	36.0
NGC 2918	143.9	31.7	105.3	12.8	11.5	1.1	E	SB0	−23.6	65.3	33.0
NGC 2832	139.9	33.7	106.4	12.6	11.4	1.3	E	E3	−23.7	59.9	95.0
NGC 2796	139.2	30.9	106.5	13.2	11.8	1.0	Sa	SA0	−23.3	71.1	38.0

Note. In descending (westward) order, according to right ascension. Columns: (1) the galaxy name; (2) the right ascension angle in J2000 coordinates (in degrees); (3) the declination angle in J2000 coordinates (in degrees); (4) the adopted (luminosity) distance described in part (iii) of Section 2.4; (5) the *g*-band apparent magnitude and (6) the *i*-band apparent magnitude from the NASA-Sloan ATLAS catalogue (http://www.nsatlas.org/) after correcting both for Galactic dust extinction and the K(z)-correction; (7) the seeing (in arcsec) measured by `imexam`; (8) the RC3 Hubble morphology classification; (9) our new classification described in Section 3.4; (10) the absolute *i*-band magnitude calculated using columns (4) and (6), with Galactic dust and *K*-correction from the NASA-Sloan ATLAS catalogue applied; and (11) the total galaxy stellar mass using the IP13 $(g-i)$-dependent M_*/L ratio applied to the SDSS-derived *i*-band magnitude. (12) the cutoff radius (in arcsec) in circularized equivalent-axis.

(83/103) of our galaxies have $R_{\mathrm{e}}/R_{\mathrm{max}} < 1$. There are 20 galaxies which have effective radii exceeding their cutoff radii ($R_{\mathrm{e}}/R_{\mathrm{max}} > 1$). They are exclusively S0 and S galaxies. The outliers illustrate the problem of using a single Sérsic fit to measure the size of a galaxy. A shallow disc profile combined with a prominent bulge can result in a long-tailed surface brightness profile. The parametrized effective size of such a galaxy, from a single Sérsic fit, will be an overestimate of the actual half-light radius. The effect of inflated galaxy radii in S0 and S galaxies is not widely appreciated and shall be addressed in a separate work.

Table C2. Galaxy sample (*continued*).

Name	RA	Dec	Dist.	$\mathfrak{m}_g$	$\mathfrak{m}_i$	Seeing	Morph.	Morph.	$\mathfrak{M}_i$	$M_{*,\mathrm{gal}}$	R_{max}
	deg	deg	Mpc	mag	mag	arcsec	(old)	(new)	mag	$10^{10}\,\mathrm{M}_\odot$	arcsec
(1)	(2)	(3)	(4)	(5)	(6)	(7)	(8)	(9)	(10)	(11)	(12)
Bin 2											
NGC 5490	212.5	17.5	80.9	12.4	11.2	0.9	E	SA0	−23.4	50.9	63.0
NGC 5444	210.9	35.1	66.7	12.2	11.0	1.0	E	E2	−23.2	38.9	85.0
NGC 5440	210.8	34.8	54.4	12.3	11.1	0.9	Sa	SA	−22.6	28.1	83.0
NGC 5406	210.1	38.9	84.8	12.3	11.1	0.8	Sbc	SAB	−23.5	54.1	53.0
NGC 5382	209.6	6.3	72.7	13.1	11.9	0.8	S0	EAS	−22.4	19.4	42.0
IC 947	208.1	0.8	74.7	12.5	11.3	1.3	S0	SA0	−23.1	36.5	12.7
NGC 5318	207.7	33.7	72.0	13.0	11.7	1.3	S0	SB0	−22.6	33.4	50.0
NGC 5172	202.3	17.1	68.3	12.3	11.2	0.7	SABc	SB	−22.9	24.4	29.0
NGC 5020	198.2	12.6	57.8	11.5	10.6	1.2	Sbc	SB	−23.2	20.7	90.0

Table C2 – *continued*

Name	RA	Dec	Dist.	$\mathfrak{m}_g$	$\mathfrak{m}_i$	Seeing	Morph.	Morph.	$\mathfrak{M}_i$	$M_{*,\mathrm{gal}}$	R_{max}
	deg	deg	Mpc	mag	mag	arcsec	(old)	(new)	mag	$10^{10}\,\mathrm{M}_\odot$	arcsec
(1)	(2)	(3)	(4)	(5)	(6)	(7)	(8)	(9)	(10)	(11)	(12)
NGC 4914	195.2	37.3	76.7	11.7	10.7	1.0	E	SAB0	−23.8	51.6	78.0
NGC 4334	185.8	7.5	70.9	12.6	11.5	1.0	Sab	SB	−22.8	26.2	45.7
NGC 4169	183.1	29.2	63.6	12.7	11.4	0.8	S0	SB0	−22.6	25.0	47.0
NGC 4015	179.7	25.0	72.2	13.1	11.8	0.9	E	SA0	−22.5	26.5	37.0
NGC 4008	179.6	28.2	61.0	12.4	11.2	0.9	E	SA0	−22.7	23.7	64.0
NGC 3872	176.5	13.8	54.2	11.8	10.6	0.8	E	SA0	−23.0	34.4	75.0
NGC 3812	175.3	24.8	60.6	12.3	11.1	0.8	E	E0	−22.8	28.5	40.0
NGC 3801	175.1	17.7	56.2	12.4	10.9	1.1	S0	SA0	−22.8	56.1	46.0
NGC 3646	170.4	20.2	70.0	12.0	10.8	1.1	Sc	SA	−23.4	50.5	29.0
NGC 3221	155.6	21.6	66.8	12.8	11.5	0.7	Sc	SB	−22.6	28.4	54.0
NGC 2954	145.1	14.9	61.6	12.6	11.4	1.1	E	SA0	−22.5	20.2	47.0
NGC 2911	143.4	10.2	51.8	11.5	10.0	1.1	S0	SA0	−23.6	108.0	128.0
NGC 2872	141.4	11.4	51.9	12.2	11.0	1.0	E	E2	−22.6	26.0	38.0
NGC 2862	141.2	26.8	65.2	12.9	11.6	0.9	SBbc	SB	−22.4	22.3	34.0
NGC 2824	139.8	26.3	45.5	11.1	9.9	0.9	S0	SA0	−23.4	44.8	23.3

Note. Columns: See Table C1.

Table C3. Galaxy sample (*continued*).

Name	RA	Dec	Dist.	$\mathfrak{m}_g$	$\mathfrak{m}_i$	Seeing	Morph.	Morph.	$\mathfrak{M}i$	$M_{*,\mathrm{gal}}$	R_{max}
	deg	deg	Mpc	mag	mag	arcsec	(old)	(new)	mag	$10^{10}\,\mathrm{M}_\odot$	arcsec
(1)	(2)	(3)	(4)	(5)	(6)	(7)	(8)	(9)	(10)	(11)	(12)
Bin 3											
NGC 5473	211.2	54.9	37.5	12.1	10.9	0.9	S0	SB0	−22.0	15.0	77.0
NGC 5448	210.7	49.2	37.8	12.0	10.8	0.8	Sa	SB	−22.1	15.8	52.0
NGC 5375	209.2	29.2	43.6	12.0	10.9	0.9	SBab	SB	−22.3	15.6	85.0
NGC 5377	209.1	47.2	34.6	11.4	10.3	1.0	Sa	SB	−22.4	17.6	113.0
NGC 5363	209.0	5.3	22.6	10.4	9.2	1.2	S0-a	SA0	−22.5	22.4	100.0
NGC 5390	208.9	40.5	46.0	11.2	10.0	0.8	Sbc	SB	−23.3	48.3	82.0
NGC 5353	208.4	40.3	42.6	11.2	10.0	1.1	S0	SB0	−23.1	38.8	28.0
NGC 5354	208.4	40.3	46.3	11.0	9.8	1.0	S0	SA0	−23.5	49.3	69.0
NGC 5350	208.3	40.4	42.5	10.9	9.8	1.0	Sbc	SB	−23.3	32.4	53.0
NGC 5326	207.7	39.6	45.4	12.2	11.0	1.0	Sa	SA	−22.3	20.1	37.0
UGC 8736	207.3	39.5	43.4	12.2	10.4	0.9	Sc	SA	−22.8	54.3	17.0
NGC 5311	207.2	40.0	48.0	12.3	10.9	0.9	S0-a	SA0	−22.5	29.4	78.0
NGC 4845	194.5	1.6	26.7	12.3	10.9	1.1	SABa	SA	−21.3	13.2	70.0
NGC 4772	193.4	2.2	26.0	11.7	10.5	1.0	SABa	SA	−21.6	10.1	112.0
NGC 4649	190.9	11.6	16.8	9.7	8.4	1.1	E	SA0	−22.7	28.1	155.0
NGC 4643	190.8	2.0	29.3	10.8	9.6	0.9	S0-a	SB0	−22.7	25.7	124.0
NGC 4636	190.7	2.7	14.7	9.3	8.2	1.1	E	SA0	−22.7	23.8	210.0
NGC 4579	189.4	11.8	21.0	10.4	9.2	1.0	Sb	SB	−22.4	19.0	75.0
NGC 4548	188.9	14.5	15.4	10.2	9.0	0.8	Sb	SB	−22.0	13.6	156.0
NGC 4536	188.6	2.2	15.6	11.2	9.7	1.1	SABb	SB	−21.3	13.2	89.0
NGC 4527	188.5	2.7	14.2	11.2	9.5	1.2	SABb	SB	−21.2	13.0	125.0
NGC 4526	188.5	7.7	16.9	10.3	9.1	1.0	S0	SB0	−22.0	13.7	72.0
NGC 4494	187.9	25.8	17.1	10.4	9.3	0.8	E	E2	−21.9	10.2	146.0
NGC 4459	187.3	14.0	16.1	10.6	9.4	0.9	S0	E2	−21.6	10.7	68.0
NGC 4429	186.9	11.1	14.9	10.4	9.1	1.1	S0-a	SA0	−21.7	12.0	108.0
NGC 4414	186.6	31.2	17.7	10.3	9.2	1.2	Sc	SA	−22.0	10.3	140.0
NGC 4382	186.4	18.2	17.9	10.0	8.9	1.4	S0-a	SA0	−22.3	12.1	120.0
NGC 4378	186.3	4.9	44.0	11.9	10.7	1.1	Sa	SA	−22.5	23.7	96.0
NGC 4374	186.3	12.9	18.5	10.0	8.8	1.1	E	SA0	−22.6	23.7	228.0
NGC 4261	184.8	5.8	31.6	11.0	9.8	1.1	E	E2	−22.7	27.2	120.0
NGC 4235	184.3	7.2	42.0	12.0	10.7	0.8	Sa	SA	−22.4	23.7	53.0
NGC 4233	184.3	7.6	33.9	12.5	11.2	0.8	S0	SA0	−21.4	10.2	66.0
NGC 4224	184.1	7.5	45.0	12.4	11.0	1.0	SABa	SA0	−22.2	23.4	71.0
NGC 4168	183.1	13.2	30.9	11.4	10.3	1.1	E	SA0	−22.1	12.0	100.0
NGC 4102	181.6	52.7	18.6	11.8	10.3	1.0	SABb	SB	−21.0	10.8	87.0

Table C3 – *continued*

Name	RA	Dec	Dist.	$\mathfrak{m}_g$	$\mathfrak{m}_i$	Seeing	Morph.	Morph.	$\mathfrak{M}i$	$M_{*,\mathrm{gal}}$	R_{max}
	deg	deg	Mpc	mag	mag	arcsec	(old)	(new)	mag	$10^{10}\,\mathrm{M}_\odot$	arcsec
(1)	(2)	(3)	(4)	(5)	(6)	(7)	(8)	(9)	(10)	(11)	(12)
NGC 4045	180.7	2.0	34.9	12.1	10.8	1.0	Sa	SB	−21.9	15.0	63.0
NGC 3976	179.0	6.7	43.1	12.2	10.9	0.8	Sb	SB	−22.2	17.6	26.0
NGC 3941	178.2	37.0	19.0	10.6	9.5	1.4	S0	SB0	−21.9	10.0	96.0
NGC 3900	177.3	27.0	34.5	11.7	10.6	1.1	S0-a	SA0	−22.1	11.3	81.0
NGC 3718	173.1	53.1	21.2	11.6	10.0	1.2	Sa	SA	−21.6	19.0	105.0
NGC 3675	171.5	43.6	15.4	10.6	9.3	1.1	Sb	SA	−21.6	11.9	135.0
NGC 3665	171.2	38.8	37.7	11.0	9.8	1.0	S0	SA0	−23.1	38.0	120.0
NGC 3658	171.0	38.6	37.3	12.0	10.7	0.9	S0	SB0	−22.1	16.2	62.0
NGC 3583	168.5	48.3	38.3	11.9	10.7	1.0	Sb	SB	−22.2	13.8	86.0
NGC 3414	162.8	28.0	25.2	11.3	10.1	0.9	S0	SA0	−21.9	12.4	107.0
NGC 3368	161.7	11.8	11.7	9.8	8.5	1.1	Sab	SB	−21.8	13.2	188.0
NGC 3189	154.5	21.8	24.2	11.1	9.8	0.9	Sa	SB	−22.2	19.0	76.0
NGC 3169	153.6	3.5	16.4	11.4	9.9	1.2	Sa	SA	−21.2	12.5	158.0
NGC 2968	145.8	31.9	28.6	12.6	10.9	1.1	Sa	SB	−21.4	15.4	77.0
NGC 2962	145.2	5.2	34.0	12.0	10.7	1.3	S0-a	SB0	−22.0	17.4	71.0
NGC 2894	142.4	7.7	35.9	13.3	11.7	0.9	Sa	SB	−21.1	11.4	48.0
NGC 2859	141.1	34.5	30.1	11.6	10.4	0.9	S0-a	SB0	−22.0	11.6	70.0

Note. Columns: See Tables C1 and C2.

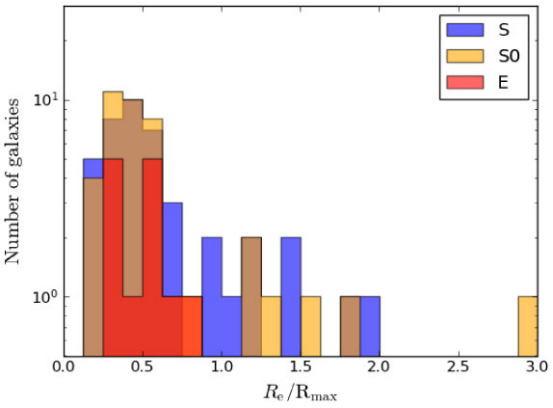

Figure C1. The distribution of galaxy circularized effective radius (R_e)–maximum radius (R_{max}) ratio. We obtained R_e via a single Sérsic fit and the R_{max} is our cutoff radius for the fit. The sample is separated by their morphological type and colour coded with red, orange, and blue for E, S0, and S galaxies, respectively. Here, we only show the distribution between $0 < R_e/R_{max} < 3.0$, where 96 galaxies are present.

APPENDIX D: LOCAL SPHEROIDS' PARAMETERS

We present the structural parameters and the masses of the bulges/spheroids in our host galaxies in Tables D1–D3. Column (2) is the distance we used to calculate the absolute magnitude and stellar masses (see Appendix A and (iv) in Section 2.4). Column (3) showcases the function we used to model the spheroids, either a Sérsic (S) or a core-Sérsic (cS) function (see Graham et al. (2003a). Columns (4)–(6) provide the parameters of the Sérsic and core-Sérsic functions. In column (4), it represents the surface brightness (i.e. μ_e) at effective radius R_e (column 5) in equivalent axis. Column (6) shows the Sérsic index n of the spheroids. Columns (7) and (8) give their apparent and absolute magnitudes, respectively. Columns (9)–(12) are the spheroids' stellar masses based on the four M_*/L ratios discussed in Section 2.3.

Table D1. Spheroid sample.

Name	Dist.	Type	μ_e	R_e	n	$\mathfrak{m}_{Sph}$	$\mathfrak{M}_{Sph}$	$\log_{10}\left(\frac{M_*}{M_\odot}\right)_{T11}$	$\log_{10}\left(\frac{M_*}{M_\odot}\right)_{Z09}$	$\log_{10}\left(\frac{M_*}{M_\odot}\right)_{RC15}$	$\log_{10}\left(\frac{M_*}{M_\odot}\right)_{IP13}$
	Mpc			kpc		mag	mag				
(1)	(2)	(3)	(4)	(5)	(6)	(7)	(8)	(9)	(10)	(11)	(12)
Bin 1											
IC 983	75.38	S	19.20	1.31	1.70	13.42	−20.97	10.33 ± 0.15	10.43 ± 0.13	10.50 ± 0.12	10.67 ± 0.09
UGC8564	87.05	S	19.86	2.13	2.70	13.12	−21.58	10.76 ± 0.11	10.94 ± 0.08	11.00 ± 0.08	11.17 ± 0.06
NGC 5208	89.72	S	18.67	1.42	1.61	13.08	−21.69	10.64 ± 0.15	10.75 ± 0.13	10.81 ± 0.11	10.98 ± 0.09
NGC 4999	76.28	S	19.15	1.08	2.16	13.65	−20.76	10.20 ± 0.17	10.28 ± 0.15	10.36 ± 0.13	10.52 ± 0.10
NGC 4921	75.09	S	20.03	1.70	2.19	13.56	−20.82	10.31 ± 0.14	10.43 ± 0.12	10.50 ± 0.11	10.67 ± 0.08
NGC 4889	87.72	cS	25.40	101.89	10.13	10.23	−24.48	11.77 ± 0.14	11.89 ± 0.12	11.96 ± 0.11	12.13 ± 0.08
NGC 4874	100.26	cS	20.05	3.71	1.78	12.65	−22.36	10.90 ± 0.15	11.01 ± 0.13	11.08 ± 0.11	11.24 ± 0.09
NGC 4583	95.22	S	19.06	1.08	1.23	14.36	−20.53	10.34 ± 0.11	10.53 ± 0.08	10.59 ± 0.08	10.76 ± 0.06
NGC 4555	89.89	S	21.07	7.74	3.41	11.46	−23.31	11.26 ± 0.15	11.35 ± 0.14	11.42 ± 0.12	11.59 ± 0.09
NGC 4213	91.24	cS	21.02	4.62	5.05	12.35	−22.45	10.90 ± 0.16	10.99 ± 0.14	11.06 ± 0.13	11.23 ± 0.10
NGC 4073	83.08	cS	23.72	40.11	6.34	10.25	−24.35	11.70 ± 0.15	11.81 ± 0.13	11.88 ± 0.11	12.05 ± 0.09
NGC 4065	84.68	S	19.12	1.43	1.62	13.39	−21.25	10.41 ± 0.16	10.49 ± 0.15	10.56 ± 0.13	10.73 ± 0.10
NGC 3968	89.26	S	18.50	0.89	1.36	14.02	−20.73	10.21 ± 0.16	10.30 ± 0.14	10.37 ± 0.13	10.54 ± 0.10
NGC 3940	86.28	S	20.78	3.23	4.05	12.82	−21.86	10.68 ± 0.15	10.78 ± 0.13	10.86 ± 0.12	11.02 ± 0.09
NGC 3937	90.69	S	19.01	1.71	2.53	12.81	−21.98	10.68 ± 0.17	10.75 ± 0.15	10.82 ± 0.14	10.99 ± 0.10
NGC 3842	85.05	S	18.89	1.51	1.49	13.12	−21.52	10.56 ± 0.15	10.66 ± 0.13	10.73 ± 0.12	10.90 ± 0.09
IC 724	82.06	S	17.63	0.60	0.95	13.97	−20.60	10.20 ± 0.15	10.31 ± 0.13	10.38 ± 0.11	10.55 ± 0.09
NGC 3805	90.42	S	23.68	26.4	4.65	11.24	−23.54	11.41 ± 0.14	11.54 ± 0.12	11.61 ± 0.10	11.78 ± 0.08
NGC 3615	96.41	cS	21.83	9.98	7.99	11.49	−23.43	11.34 ± 0.15	11.45 ± 0.13	11.52 ± 0.11	11.69 ± 0.09
NGC 3270	89.11	S	18.50	1.02	1.01	13.88	−20.86	10.35 ± 0.14	10.47 ± 0.11	10.54 ± 0.10	10.71 ± 0.08
NGC 3209	89.78	S	18.67	1.53	2.15	12.80	−21.97	10.73 ± 0.15	10.83 ± 0.13	10.90 ± 0.12	11.07 ± 0.09
NGC 3158	101.55	cS	20.49	6.62	3.65	11.48	−23.56	11.41 ± 0.14	11.53 ± 0.12	11.60 ± 0.11	11.77 ± 0.08
NGC 3126	75.01	S	18.33	0.71	1.72	13.85	−20.52	10.27 ± 0.12	10.43 ± 0.10	10.49 ± 0.09	10.66 ± 0.07
NGC 3106	88.19	cS	18.82	1.28	2.12	13.35	−21.38	10.47 ± 0.16	10.56 ± 0.14	10.64 ± 0.13	10.80 ± 0.10
NGC 2918	98.82	S	19.04	1.88	1.67	13.06	−21.91	10.76 ± 0.14	10.88 ± 0.12	10.95 ± 0.10	11.12 ± 0.08
NGC 2832	100.35	cS	21.72	12.69	5.18	11.15	−23.9	11.50 ± 0.15	11.60 ± 0.14	11.67 ± 0.12	11.84 ± 0.09
NGC 2796	100.39	cS	19.13	1.95	2.78	12.88	−22.13	10.94 ± 0.12	11.12 ± 0.09	11.18 ± 0.08	11.85 ± 0.07

Note. Columns: (1) the name of the galaxy in descending (westward) order, according to Right Ascension; (2) The selected distance as described in Section 2.4 updated with the newly available *Cosmicflow-3* distances (Kourkchi et al. (2020), see also Appendix A and (iv) in Section 2.4); (3) Using an SDSS *i*-band image, the spheroid's geometric mean axis, equivalent to a circularized radius, was fit with either a Sérsic (1968) (S) or a core-Sérsic (cS) model (see Graham et al. 2003a); (4) the surface brightness μ_e at R_e (in mag arcsec^{-2}); (5) the effective radius (in kpc); (6) the Sérsic index; (7) the apparent magnitude of the spheroid in the *i*-band (AB mag) with the Galactic extinction and *K*-correction applied; (8) the absolute magnitude of the spheroid in the *i*-band (AB mag); the stellar mass of the spheroid using the *g*-*i* colour-dependent M_*/L_i ratios from (9) T11, (10) Z09, (11) RC15, and (12) IP13 (see equation 3).

Table D2. Spheroid sample (*continued*).

Name	Dist.	Type	μ_e	R_e	n	$\mathfrak{m}_{Sph}$	$\mathfrak{M}_{Sph}$	$\log_{10}\left(\frac{M_*}{M_\odot}\right)_{T11}$	$\log_{10}\left(\frac{M_*}{M_\odot}\right)_{Z09}$	$\log_{10}\left(\frac{M_*}{M_\odot}\right)_{RC15}$	$\log_{10}\left(\frac{M_*}{M_\odot}\right)_{IP13}$
	Mpc			kpc		mag	mag				
(1)	(2)	(3)	(4)	(5)	(6)	(7)	(8)	(9)	(10)	(11)	(12)
Bin 2											
NGC 5490	66.93	S	19.25	2.17	2.62	11.88	−22.24	10.86 ± 0.15	10.98 ± 0.12	11.05 ± 0.11	11.22 ± 0.09
NGC 5444	58.11	cS	24.26	31.04	9.52	10.44	−23.38	11.32 ± 0.15	11.43 ± 0.13	11.50 ± 0.11	11.67 ± 0.09
NGC 5440	54.94	S	18.64	1.18	1.98	12.34	−21.36	10.55 ± 0.14	10.69 ± 0.11	10.75 ± 0.10	10.92 ± 0.08
NGC 5406	74.03	S	18.02	0.57	1.20	14.19	−20.15	10.02 ± 0.15	10.12 ± 0.13	10.19 ± 0.11	10.36 ± 0.09
NGC 5382	60.04	cS	22.28	7.22	9.83	11.57	−22.33	10.87 ± 0.15	10.97 ± 0.13	11.04 ± 0.12	11.21 ± 0.09
IC 947	61.88	S	17.69	0.50	1.63	13.57	−20.39	10.09 ± 0.15	10.19 ± 0.13	10.26 ± 0.12	10.43 ± 0.09
NGC 5318	62.57	S	19.30	1.57	2.26	12.57	−21.41	10.61 ± 0.13	10.77 ± 0.10	10.83 ± 0.09	11.00 ± 0.07
NGC 5172	57.35	S	19.82	0.92	1.80	14.20	−19.60	9.71 ± 0.17	9.77 ± 0.16	9.85 ± 0.14	10.02 ± 0.11
NGC 5020	50.51	S	18.29	0.73	0.64	13.37	−20.15	9.79 ± 0.22	9.79 ± 0.23	9.88 ± 0.20	10.05 ± 0.15
NGC 4914	67.45	S	19.86	3.45	3.26	11.42	−22.72	10.96 ± 0.17	11.03 ± 0.16	11.10 ± 0.14	11.27 ± 0.11
NGC 4334	60.86	S	17.72	0.54	0.51	13.94	−19.98	9.92 ± 0.16	10.02 ± 0.14	10.09 ± 0.12	10.26 ± 0.09
NGC 4169	58.12	S	19.24	1.94	2.17	11.92	−21.90	10.74 ± 0.14	10.86 ± 0.12	10.92 ± 0.11	11.09 ± 0.08
NGC 4015	64.45	S	18.81	0.89	2.00	13.43	−20.61	10.26 ± 0.13	10.40 ± 0.11	10.46 ± 0.10	10.63 ± 0.08
NGC 4008	56.19	S	19.14	1.57	2.34	12.21	−21.54	10.58 ± 0.16	10.70 ± 0.14	10.77 ± 0.12	10.94 ± 0.09
NGC 3872	50.00	S	17.80	0.77	1.86	12.18	−21.32	10.43 ± 0.16	10.52 ± 0.15	10.59 ± 0.13	10.76 ± 0.10
NGC 3812	55.94	cS	21.10	3.88	6.60	11.65	−22.09	10.78 ± 0.15	10.89 ± 0.13	10.96 ± 0.12	11.13 ± 0.09

Table D2 – *continued*

Name	Dist.	Type	μ_e	R_e	n	$\mathfrak{m}_{Sph}$	$\mathfrak{M}_{Sph}$	$\log_{10}\left(\frac{M_*}{M_\odot}\right)_{T11}$	$\log_{10}\left(\frac{M_*}{M_\odot}\right)_{Z09}$	$\log_{10}\left(\frac{M_*}{M_\odot}\right)_{RC15}$	$\log_{10}\left(\frac{M_*}{M_\odot}\right)_{IP13}$
	Mpc			kpc		mag	mag				
(1)	(2)	(3)	(4)	(5)	(6)	(7)	(8)	(9)	(10)	(11)	(12)
NGC 3801	52.01	S	20.44	1.71	2.41	13.07	−20.51	10.34 ± 0.11	10.54 ± 0.08	10.60 ± 0.08	10.77 ± 0.06
NGC 3646	63.60	S	18.59	0.78	1.41	13.66	−20.36	10.09 ± 0.15	10.19 ± 0.13	10.26 ± 0.12	10.43 ± 0.09
NGC 3221	62.85	S	19.09	0.68	1.02	14.57	−19.42	9.77 ± 0.14	9.91 ± 0.11	9.97 ± 0.10	10.14 ± 0.08
NGC 2954	59.51	cS	18.69	1.27	1.75	12.44	−21.44	10.48 ± 0.16	10.57 ± 0.14	10.64 ± 0.13	10.81 ± 0.10
NGC 2911	50.62	cS	21.16	4.33	4.43	11.41	−22.11	10.97 ± 0.11	11.16 ± 0.08	11.22 ± 0.08	11.39 ± 0.06
NGC 2872	50.40	S	20.88	5.01	3.65	10.90	−22.61	11.01 ± 0.15	11.12 ± 0.13	11.19 ± 0.11	11.35 ± 0.09
NGC 2862	61.24	S	18.62	0.68	1.15	13.98	−19.96	9.96 ± 0.14	10.07 ± 0.12	10.14 ± 0.11	10.31 ± 0.08
NGC 2824	45.38	S	17.70	0.29	1.30	14.24	−19.04	9.52 ± 0.16	9.61 ± 0.15	9.68 ± 0.13	9.85 ± 0.10

Note. Columns: See Table D1.

Table D3. Spheroid sample (*continued*).

Name	Dist.	Type	μ_e	R_e	n	$\mathfrak{m}_{Sph}$	$\mathfrak{M}_{Sph}$	$\log_{10}\left(\frac{M_*}{M_\odot}\right)_{T11}$	$\log_{10}\left(\frac{M_*}{M_\odot}\right)_{Z09}$	$\log_{10}\left(\frac{M_*}{M_\odot}\right)_{RC15}$	$\log_{10}\left(\frac{M_*}{M_\odot}\right)_{IP13}$
	Mpc			kpc		mag	mag				
(1)	(2)	(3)	(4)	(5)	(6)	(7)	(8)	(9)	(10)	(11)	(12)
Bin 3											
NGC 5473	31.17	S	17.39	0.39	1.35	12.49	−19.98	9.99 ± 0.14	10.12 ± 0.11	10.18 ± 0.10	10.35 ± 0.08
NGC 5448	30.82	S	19.12	0.53	1.97	13.33	−19.11	9.63 ± 0.14	9.75 ± 0.12	9.81 ± 0.11	9.98 ± 0.08
NGC 5375	36.06	S	20.07	1.36	1.82	12.57	−20.22	9.99 ± 0.16	10.08 ± 0.15	10.15 ± 0.13	10.32 ± 0.10
NGC 5377	26.89	S	19.01	0.61	2.47	12.47	−19.67	9.78 ± 0.16	9.87 ± 0.14	9.94 ± 0.13	10.11 ± 0.10
NGC 5363	15.80	S	19.12	1.21	2.24	9.97	−21.02	10.36 ± 0.15	10.46 ± 0.13	10.53 ± 0.12	10.70 ± 0.09
NGC 5390	38.20	S	19.46	0.75	2.58	13.22	−19.69	9.86 ± 0.14	9.98 ± 0.12	10.05 ± 0.11	10.21 ± 0.08
NGC 5353	34.85	S	17.36	0.44	0.84	12.61	−20.10	10.01 ± 0.15	10.12 ± 0.12	10.19 ± 0.11	10.36 ± 0.09
NGC 5354	38.76	S	19.57	1.87	2.55	11.39	−21.55	10.56 ± 0.15	10.66 ± 0.13	10.73 ± 0.12	10.90 ± 0.09
NGC 5350	34.77	S	18.99	0.35	0.98	14.71	−17.99	9.06 ± 0.18	9.12 ± 0.17	9.19 ± 0.15	9.36 ± 0.11
NGC 5326	37.55	S	18.59	0.82	2.47	12.14	−20.73	10.28 ± 0.14	10.40 ± 0.12	10.47 ± 0.11	10.64 ± 0.08
UGC 8736	35.81	S	21.58	0.63	1.82	15.75	−17.02	8.99 ± 0.10	9.20 ± 0.07	9.26 ± 0.07	9.43 ± 0.06
NGC 5311	40.64	S	19.49	1.26	2.59	12.26	−20.79	10.38 ± 0.12	10.53 ± 0.10	10.60 ± 0.09	10.77 ± 0.07
NGC 4845	18.51	S	20.83	0.95	1.98	12.64	−18.70	9.63 ± 0.11	9.83 ± 0.09	9.88 ± 0.09	10.05 ± 0.07
NGC 4772	16.60	S	19.51	0.74	1.72	11.67	−19.43	9.73 ± 0.15	9.85 ± 0.13	9.91 ± 0.11	10.08 ± 0.09
NGC 4649	16.83	cS	24.85	5.37	0.87	9.71	−21.42	10.54 ± 0.15	10.66 ± 0.12	10.73 ± 0.11	10.90 ± 0.09
NGC 4643	21.64	S	18.43	0.82	1.71	10.95	−20.73	10.23 ± 0.16	10.32 ± 0.14	10.39 ± 0.12	10.56 ± 0.10
NGC 4636	13.11	cS	20.82	2.09	2.15	10.00	−20.59	10.16 ± 0.16	10.25 ± 0.14	10.33 ± 0.12	10.49 ± 0.10
NGC 4579	21.00	S	18.92	1.13	2.82	10.40	−21.21	10.40 ± 0.16	10.49 ± 0.14	10.57 ± 0.13	10.74 ± 0.10
NGC 4548	15.42	S	19.01	0.50	1.68	11.85	−19.09	9.58 ± 0.15	9.68 ± 0.13	9.75 ± 0.12	9.92 ± 0.09
NGC 4536	15.57	S	17.65	0.20	1.48	12.60	−18.36	9.49 ± 0.11	9.69 ± 0.08	9.75 ± 0.08	9.92 ± 0.06
NGC 4527	14.16	S	18.03	0.28	1.52	12.04	−18.71	9.67 ± 0.10	9.88 ± 0.08	9.94 ± 0.07	10.11 ± 0.06
NGC 4526	16.90	S	18.59	0.85	0.43	11.11	−20.03	9.95 ± 0.15	10.06 ± 0.14	10.13 ± 0.12	10.30 ± 0.10
NGC 4494	17.06	S	20.67	3.70	2.93	9.14	−22.02	10.71 ± 0.17	10.79 ± 0.15	10.86 ± 0.13	11.03 ± 0.10
NGC 4459	16.07	S	20.87	3.21	4.00	9.30	−21.73	10.64 ± 0.15	10.75 ± 0.13	10.82 ± 0.12	10.99 ± 0.09
NGC 4429	16.76	S	19.37	1.42	1.38	10.23	−20.89	10.33 ± 0.15	10.45 ± 0.13	10.51 ± 0.12	10.68 ± 0.10
NGC 4414	17.69	S	17.16	0.29	1.26	11.65	−19.58	9.69 ± 0.18	9.75 ± 0.17	9.83 ± 0.15	10.00 ± 0.11
NGC 4382	17.88	cS	18.57	1.04	2.61	9.94	−21.32	10.34 ± 0.19	10.38 ± 0.19	10.46 ± 0.16	10.63 ± 0.12
NGC 4378	41.00	S	19.10	1.37	2.30	11.76	−21.31	10.50 ± 0.14	10.62 ± 0.12	10.69 ± 0.11	10.86 ± 0.08
NGC 4374	18.51	S	19.57	2.61	1.75	9.20	−22.14	10.79 ± 0.15	10.89 ± 0.14	10.96 ± 0.12	11.13 ± 0.09
NGC 4261	31.62	cS	23.29	20.79	8.88	9.03	−23.47	11.36 ± 0.15	11.47 ± 0.13	11.54 ± 0.11	11.71 ± 0.09
NGC 4235	39.40	S	19.37	0.84	2.36	13.04	−22.10	10.01 ± 0.13	10.16 ± 0.11	10.22 ± 0.10	10.39 ± 0.08
NGC 4233	37.45	S	18.59	0.94	0.69	12.44	−20.43	10.20 ± 0.13	10.34 ± 0.11	10.40 ± 0.10	10.57 ± 0.08
NGC 4224	42.00	S	19.56	1.13	2.87	12.56	−20.56	10.28 ± 0.12	10.43 ± 0.10	10.50 ± 0.09	10.67 ± 0.07
NGC 4168	37.02	S	19.98	2.46	1.99	11.18	−21.66	10.52 ± 0.18	10.58 ± 0.17	10.65 ± 0.15	10.82 ± 0.11
NGC 4102	15.46	S	16.35	0.12	0.60	12.84	−18.11	9.41 ± 0.10	9.61 ± 0.08	9.67 ± 0.07	9.84 ± 0.06
NGC 4045	33.27	S	17.58	0.26	0.89	13.85	−18.76	9.50 ± 0.14	9.63 ± 0.11	9.70 ± 0.10	9.87 ± 0.08
NGC 3976	41.06	S	17.47	0.37	1.51	13.25	−22.06	9.92 ± 0.14	10.04 ± 0.12	10.11 ± 0.11	10.28 ± 0.08
NGC 3941	13.85	S	17.20	0.27	1.52	11.21	−19.49	9.68 ± 0.17	9.75 ± 0.16	9.83 ± 0.14	9.99 ± 0.10
NGC 3900	30.53	S	19.28	0.77	1.34	12.79	−19.63	9.71 ± 0.18	9.78 ± 0.16	9.85 ± 0.14	10.02 ± 0.11

Table D3 – *continued*

Name	Dist.	Type	μ_e	R_e	n	$\mathfrak{m}_{Sph}$	$\mathfrak{M}_{Sph}$	$\log_{10}\left(\frac{M_*}{M_\odot}\right)_{T11}$	$\log_{10}\left(\frac{M_*}{M_\odot}\right)_{Z09}$	$\log_{10}\left(\frac{M_*}{M_\odot}\right)_{RC15}$	$\log_{10}\left(\frac{M_*}{M_\odot}\right)_{IP13}$
	Mpc			kpc		mag	mag				
(1)	(2)	(3)	(4)	(5)	(6)	(7)	(8)	(9)	(10)	(11)	(12)
NGC 3718	17.97	S	18.86	0.28	2.10	13.22	−18.05	9.40 ± 0.10	9.62 ± 0.07	9.67 ± 0.07	9.84 ± 0.06
NGC 3675	13.44	S	18.22	0.22	2.15	12.45	−18.19	9.30 ± 0.13	9.44 ± 0.11	9.50 ± 0.10	9.67 ± 0.08
NGC 3665	33.84	S	19.68	2.51	1.31	10.90	−21.75	10.67 ± 0.15	10.78 ± 0.13	10.85 ± 0.11	11.02 ± 0.09
NGC 3658	33.44	S	16.79	0.21	1.15	13.45	−19.18	9.64 ± 0.14	9.76 ± 0.12	9.83 ± 0.11	10.00 ± 0.08
NGC 3583	34.37	S	17.93	0.31	1.12	13.81	−18.87	9.46 ± 0.16	9.54 ± 0.14	9.62 ± 0.13	9.78 ± 0.10
NGC 3414	27.53	S	18.76	0.93	2.49	11.35	−20.85	10.28 ± 0.15	10.38 ± 0.13	10.45 ± 0.12	10.62 ± 0.09
NGC 3368	11.70	S	17.83	0.37	1.45	10.80	−19.54	9.80 ± 0.14	9.93 ± 0.12	9.99 ± 0.11	10.16 ± 0.08
NGC 3189	24.88	S	16.83	0.31	1.32	11.91	−20.07	10.04 ± 0.14	10.17 ± 0.11	10.24 ± 0.10	10.41 ± 0.08
NGC 3169	16.44	S	17.87	0.46	1.58	11.06	−20.02	10.15 ± 0.11	10.35 ± 0.08	10.40 ± 0.08	10.57 ± 0.06
NGC 2968	28.33	S	19.24	0.81	2.15	12.28	−19.98	10.17 ± 0.10	10.39 ± 0.08	10.44 ± 0.07	10.61 ± 0.06
NGC 2962	34.04	S	18.84	0.75	2.01	12.38	−20.28	10.11 ± 0.14	10.23 ± 0.12	10.30 ± 0.11	10.47 ± 0.08
NGC 2894	37.18	S	18.95	0.89	2.26	12.25	−20.60	10.42 ± 0.10	10.64 ± 0.07	10.69 ± 0.07	10.86 ± 0.06
NGC 2859	30.00	S	17.88	0.67	1.50	11.63	−20.75	10.21 ± 0.16	10.30 ± 0.15	10.37 ± 0.13	10.54 ± 0.10

Note. Columns: See Tables D1 and D2.

This paper has been typeset from a TEX/LATEX file prepared by the author.